


2013

## SYNTHESIS OF GRAPHENE AND ITS APPLICATIONS FOR DYE-SENSITIZED SOLAR CELLS

Hui Wang  
*Michigan Technological University*

Follow this and additional works at: <https://digitalcommons.mtu.edu/etds>


 Part of the [Materials Science and Engineering Commons](#), and the [Power and Energy Commons](#)  
Copyright 2013 Hui Wang

---

### Recommended Citation

Wang, Hui, "SYNTHESIS OF GRAPHENE AND ITS APPLICATIONS FOR DYE-SENSITIZED SOLAR CELLS",  
Dissertation, Michigan Technological University, 2013.  
<https://digitalcommons.mtu.edu/etds/681>

Follow this and additional works at: <https://digitalcommons.mtu.edu/etds>

 Part of the [Materials Science and Engineering Commons](#), and the [Power and Energy Commons](#)

SYNTHESIS OF GRAPHENE AND ITS APPLICATIONS FOR DYE SENSITIZED  
SOLAR CELLS

By

Hui Wang

A DISSERTATION

Submitted in partial fulfillment of the requirements for the degree of

DOCTOR OF PHILOSOPHY

In Materials Science and Engineering

MICHIGAN TECHNOLOGICAL UNIVERSITY

2013

© 2013 Hui Wang

This dissertation has been approved in partial fulfillment of the requirements for the Degree of DOCTOR OF PHILOSOPHY in MATERIALS SCIENCE AND ENGINEERING.

Department of Materials Science and Engineering

Dissertation Advisor: *Prof. Yun Hang Hu*

Committee Member: *Prof. Calvin L White*

Committee Member: *Prof. Stephen A Hackney*

Committee Member: *Prof. Feng Zhao*

Department Chair: *Prof. Stephen L Kampe*

# Table of Contents

<b>Table of Contents .....</b>	<b>iii</b>
<b>List of Figures.....</b>	<b>vii</b>
<b>List of Tables .....</b>	<b>xi</b>
<b>Preface.....</b>	<b>xii</b>
<b>Acknowledgement.....</b>	<b>xiii</b>
<b>List of Abbreviations .....</b>	<b>xv</b>
<b>Abstract.....</b>	<b>xviii</b>
<b>Chapter 1 Background .....</b>	<b>1</b>
<b>1.1 Photovoltaic Cells.....</b>	<b>1</b>
1.1.1 Crystalline Si solar cells .....	2
1.1.2 Thin film solar cells.....	3
1.1.3 Dye-sensitized solar cells .....	4
<b>1.2 Graphene.....</b>	<b>6</b>
1.2.1 Preparation.....	7
1.2.2 Physical properties.....	9
1.2.3 Chemical properties.....	11
<b>1.3 Graphene for Photovoltaic Solar Cells .....</b>	<b>12</b>
1.3.1 Transparent electrode .....	12
1.3.2 Functionalized graphene as hole collecting materials .....	23
1.3.3 Functionalized graphene as electron-accepting material.....	23
1.3.4 Photocatalysts of graphene–semiconductor.....	26
<b>1.4 Graphene for Dye-sensitized Solar Cells.....</b>	<b>28</b>

1.4.1 Transparent electrode .....	28
1.4.2 Promoter in photoelectrode for DSSCs .....	30
1.4.3 Counter electrode for DSSCs .....	34
<b>Chapter 2 Goals and Hypotheses.....</b>	<b>36</b>
<b>Chapter 3 Effect of Oxygen Content on Structures of Graphite Oxides.....</b>	<b>39</b>
<b>3.1 Introduction .....</b>	<b>39</b>
<b>3.2 Experimental.....</b>	<b>41</b>
3.2.1 Sample preparation .....	41
3.2.2 Characterization.....	42
<b>3.3 Results and Discussion .....</b>	<b>48</b>
<b>3.4 Conclusion.....</b>	<b>57</b>
<b>Chapter 4 Electrolyte-induced Precipitation of Graphene Oxide in Its Aqueous Solution .....</b>	<b>58</b>
<b>4.1 Introduction .....</b>	<b>58</b>
<b>4.2 Experimental.....</b>	<b>59</b>
4.2.1 Sample preparation .....	59
4.2.2 Fabrication of DSSCs .....	60
4.2.3 Characterization.....	61
<b>4.3 Results and Discussion .....</b>	<b>63</b>
4.3.1. Electrolyte-induced GO precipitation.....	63
4.3.2. Characterization of GO precipitates .....	72
4.3.3 Application of GO precipitation for DSSCs.....	78
<b>4.4 Conclusion.....</b>	<b>79</b>
<b>Chapter 5 Three-Dimensional Honeycomb-like Structured Graphene.....</b>	<b>81</b>

<b>5.1 Introduction .....</b>	<b>81</b>
<b>5.2 Thermodynamic Calculation.....</b>	<b>83</b>
<b>5.3 Experimental.....</b>	<b>84</b>
5.3.1 Synthesis of graphene with honeycomb-like structure.....	84
5.3.2 Characterization.....	85
<b>5.4 Results and Discussion .....</b>	<b>88</b>
5.4.1 X-ray diffraction measurement.....	88
5.4.2 Morphology of honeycomb structured graphene.....	90
<b>5.5 Conclusion.....</b>	<b>96</b>
<b>Chapter 6 Three-Dimensional Honeycomb Structured Graphene as Counter Electrode Catalysts for Dye-sensitized Solar Cells .....</b>	<b>98</b>
<b>6.1 Introduction .....</b>	<b>98</b>
<b>6.2 Experimental.....</b>	<b>101</b>
6.2.1 Fabrication of DSSCs .....	101
6.2.2 Characterization.....	102
<b>6.3 Results and Discussion .....</b>	<b>104</b>
6.3.1 Photovoltaic performance of DSSCs with Honeycomb Structure graphene as CEs.....	104
6.3.2 Electrochemical characteristics of DSSCs with Honeycomb Structure graphene as CEs .....	107
<b>6.4 Conclusion.....</b>	<b>110</b>
<b>Chapter 7 Summary .....</b>	<b>111</b>
<b>References .....</b>	<b>114</b>
<b>Appendix A Copyright Permission of Fig 1.2 and Table 1.1 .....</b>	<b>136</b>
<b>Appendix B Copyright Permission of Fig 1.3.....</b>	<b>138</b>

<b>Appendix C Copyright Permission of Fig 1.4.....</b>	<b>139</b>
<b>Appendix D Copyright Permission of Fig 1.5.....</b>	<b>140</b>
<b>Appendix E Copyright Permission of Fig 1.6.....</b>	<b>141</b>
<b>Appendix F Copyright Permission of Fig 1.7 .....</b>	<b>142</b>
<b>Appendix G Copyright Permission of Fig 1.8 .....</b>	<b>144</b>
<b>Appendix H Copyright Permission of Chapter 1.....</b>	<b>145</b>
<b>Appendix I Copyright Permission of Chapter 3 .....</b>	<b>147</b>
<b>Appendix J Copyright Permission of Chapter 4.....</b>	<b>148</b>
<b>Appendix K Copyright Permission of Chapter 5 and Chapter 6.....</b>	<b>150</b>
<b>Appendix L Copyright Permission of Chapter 6 .....</b>	<b>152</b>

## List of Figures

<b>Fig.1.1.</b> Working principle of a DSSC .....	5
<b>Fig.1.2.</b> Structure and performance of solar cell based on graphene electrodes. ....	15
<b>Fig.1.3.</b> The fabricated device with structure graphene/PEDOT:PSS/P3HT:PCBM/LiF/Al .....	18
<b>Fig.1.4.</b> The conductivity of reduced GO films fabricated by spin-coating on quartz with thermal reduction in the temperature range of 600-1000 °C.....	20
<b>Fig.1.5.</b> Electrical measurements of G-CNT and ITO films (a) before and (b) after 10 times of bending by 60°. ....	22
<b>Fig.1.6.</b> Structure and performance of solar cell based on graphene electrodes. ....	29
<b>Fig.1.7.</b> Application of graphene-TiO <sub>2</sub> interfacial layer to prevent back-transport reaction of electrons.....	33
<b>Fig.1.8.</b> Operational principle of the device: the introduced 2D graphene bridges perform as an electron acceptor and transfer the electrons quickly.....	34
<b>Fig.3.1.</b> Scintag XDS2000 Powder Diffractometer.....	42
<b>Fig.3.2.</b> SDT Q600 Thermogravimetric Analyzer.....	43
<b>Fig.3.3.</b> Jobin-Yvon LabRAM HR800 Raman Spectrometer. ....	43
<b>Fig.3.4.</b> Micromeritics ASAP2000 sorptometer .....	44
<b>Fig.3.5.</b> Jasco Fourier Transformed Infrared (FTIR) Spectrometer. ....	45
<b>Fig.3.6.</b> Hewlett-Packard 5970 Series Mass Selective Detector. ....	46
<b>Fig.3.7.</b> Hitachi S-4700 FE-SEM. ....	46
<b>Fig.3.8.</b> JEOL JEM-4000FX TEM. ....	47
<b>Fig.3.9.</b> FTIR spectra of graphite oxides prepared with various oxidation times .....	48
<b>Fig.3.10.</b> TGA curves of graphite oxides prepared with various oxidation times.....	49



<b>Fig.3.11.</b> TPD-MS spectrum of of graphite oxide .....	50
<b>Fig.3.12.</b> Variation of the oxygen content of graphite oxide with the oxidation time of preparation .....	51
<b>Fig.3.13.</b> XRD patterns of graphite oxides prepared with various oxidation times .....	52
<b>Fig.3.14.</b> FE-SEM images of graphite (a) and graphite oxidized for 2 h (b) and TEM image of graphite oxide for 2 h (c). .....	53
<b>Fig.3.15.</b> Relationship between the interplanar distance and oxygen content of graphite oxides. ....	54
<b>Fig.3.16.</b> Relationship between BET surface areas of graphite oxides and their oxygen contents .....	55
<b>Fig.3.17.</b> Raman spectra of pristine graphite and graphite oxides prepared with various oxidation times.....	56
<b>Fig.3.18.</b> The relationship between intensity ratios of Raman D to G bands of graphite oxides and their oxygen contents.....	57
<b>Fig.4.1.</b> Shimadzu UV-2450 Spectrometer.....	62
<b>Fig.4.2.</b> Newport Sunlight Simulator and Keithley 2400 Multi-meter.....	62
<b>Fig.4.3.</b> Precipitation in aqueous solutions of GO, 0.4 M LiCl-GO, 0.4 M HCl-GO, and 0.4 M LiOH-GO (from left to right) after (a) 0 min, (b) 10 min, (c) 2 h, (d) 24 h, (e) 48 h, and (f) 72 h.....	64
<b>Fig.4.4.</b> Precipitation of LiCl-GO solutions with different concentrations of LiCl (0, 0.1, 0.2, 0.4, 0.6, and 0.8 M, from left to right) after (a) 0 min, (b) 10 min, (c) 2 hr, (d) 24 hr, (e) 48 hr, and (f) 72 hr.....	65
<b>Fig.4.5.</b> Precipitation of HCl-GO solutions with different concentrations of HCl (0, 0.1, 0.2, 0.4, 0.6, and 0.8 M, from left to right) after (a) 0 min, (b) 10 min, (c) 2 hr, (d) 24 hr, (e) 48 hr, and (f) 72 hr.....	66
<b>Fig.4.6.</b> Precipitation of LiOH-GO solutions with different concentrations of LiOH (0, 0.1, 0.2, 0.4, 0.6, and 0.8 M, from left to right) after (a) 0 min, (b) 10 min, (c) 2 hr, (d) 24 hr, (e) 48 hr, and (f) 72 hr. ....	66
<b>Fig.4.7.</b> Precipitation in aqueous solutions of GO, 0.4 M KCl-GO, 0.4 M KBr-GO, and 0.4 M LiBr (from left to right) after (a) 0 min, (b) 2 hr, (c) 24 hr, and (d) 72 hr. ....	67

<b>Fig.4.8.</b> UV-vis absorption spectra of (a) GO solution, (b) top supernatant of 0.4 M LiCl-GO solution after precipitation, (c) top supernatant of 0.4 M HCl-GO solution after precipitation, and (d) top supernatant of 0.4 M LiOH-GO after precipitation. ....	68
<b>Fig.4.9.</b> UV-vis absorption spectra of GO solution (a) and top supernatants (after precipitation) of LiCl-GO solutions with various LiCl concentrations: (b) 0.1 M, (c) 0.2 M, (d) 0.4 M, (e) 0.6 M, and (f) 0.8 M. ....	68
<b>Fig.4.10.</b> UV-vis absorption spectra of GO solution (a) and top supernatants (after precipitation) of HCl-GO solutions with various concentrations of HCl: (b) 0.1 M, (c) 0.2 M, (d) 0.4 M, (e) 0.6 M, and (f) 0.8 M. ....	69
<b>Fig.4.11.</b> UV-vis absorption spectra of GO solution (a) and top supernatants (after precipitation) of LiOH-GO solutions with various LiOH concentrations: (b) 0.1 M, (c) 0.2 M, (d) 0.4 M, (e) 0.6 M, and (f) 0.8 M. ....	69
<b>Fig.4.12</b> UV-vis absorption spectra of GO precipitates from (a) 0.4 M LiCl-GO solution, (b) 0.4 M HCl-GO solution, and (c) 0.4 M LiOH-GO solution .....	72
<b>Fig.4.13.</b> TEM images of (a) GO sheets from GO solution, (b) LiCl-induced GO precipitate, (c) HCl-induced GO precipitate, and (d) LiOH-induced GO precipitate. ....	74
<b>Fig.4.14.</b> Raman spectra of (a) GO sheets from GO solution, (b) HCl-induced GO precipitate, and (c) LiOH-induced GO precipitate .....	76
<b>Fig.4.15.</b> FTIR spectra of (a) GO sheets from GO solution, (b) HCl-induced GO precipitate, and (c) LiOH-induced GO precipitate. ....	77
<b>Fig.4.16.</b> FESEM images: (a) FTO glass substrate and (b) FTO glass coated with HCl induced GO precipitate. ....	79
<b>Fig.5.2.</b> Relationships of Gibbs free energy change ( $\Delta G$ ) and reaction enthalpy change ( $\Delta H$ ) with temperature for reaction between $\text{Li}_2\text{O}$ and $\text{CO}$ to graphene and $\text{Li}_2\text{CO}_3$ . ....	84
<b>Fig.5.3.</b> JEOL JEM2010F Electron Microscope .....	86
<b>Fig.5.4.</b> SPECS surface nano analysis .....	87
<b>Fig.5.5.</b> CEC 240 XA Elemental Analyzer.....	87
<b>Fig.5.6.</b> Jandel four-point probe system with RM3 test unit. ....	88
<b>Fig.5.7.</b> XRD patterns of solid products from reaction between $\text{Li}_2\text{O}$ and $\text{CO}$ at $550^\circ\text{C}$ with three reaction times (12, 24, and 48h). ....	89

<b>Fig.5.8.</b> XRD patterns of HSG powder obtained from reaction between $\text{Li}_2\text{O}$ and CO at 550 °C (followed by hydrochloride acid wash). .....	90
<b>Fig.5.9.</b> FESEM images of graphene sheets produced from reaction between CO and $\text{Li}_2\text{O}$ for different time: (a) 12 h; (b) 24 h; (c) and (d) 48 h. ....	91
<b>Fig.5.10.</b> TEM image and electron diffraction pattern of graphene sheets produced from reaction between CO and $\text{Li}_2\text{O}$ for (a), (b)12 h; (c), (d) 48 h. ....	92
<b>Fig.5.11.</b> High-angle annular dark field (HAADF) image and b EELS for locations 1-4 for graphene sheets produced from reaction between CO and $\text{Li}_2\text{O}$ at 550°C for 48h.....	93
<b>Fig.5.12.</b> XPS spectra of (a) HSG-12h (honeycomb structured graphene synthesized from reaction between CO and $\text{Li}_2\text{O}$ for 12h), (b) HSG-24h and (c) HSG-48h.....	95
<b>Fig.5.13.</b> Raman spectra of honeycomb structured graphene (HSG) after heat treatment at 550 °C for 12 h, 24 h, and 48 h. ....	96
<b>Fig.6.1.</b> Counter electrode in a DSSC.....	99
<b>Fig.6.2.</b> Newport IPCE Kit .....	102
<b>Fig.6.3.</b> CHI660 Electrochemical Workstation .....	103
<b>Fig.6.4.</b> EG&G Princeton Applied Research Electrochemical Workstation .....	103
<b>Fig.6.5.</b> I-V curves of DSSCs with honeycomb-structured graphene as a counter electrode .....	105
<b>Fig.6.6.</b> IPCE of DSSCs with honeycomb structured graphene counter electrodes.....	107
<b>Fig.6.7.</b> EIS of DSSCs with honeycomb structured graphene counter electrodes .....	108
<b>Fig.6.8.</b> CV curves of DSSCs with honeycomb structured graphene counter electrodes .....	110

## List of Tables

<b>Table 1.1.</b> Performance of the solar cells based on TGF and ITO anodes.....	15
<b>Table 4.1.</b> Photovoltaic characteristics of DSSCs with GO precipitates on ITO glasses as the counter electrode .....	79
<b>Table 5.1.</b> EDS analysis of honeycomb structured graphene.....	94
<b>Table 6.1.</b> The photovoltaic performances of DSSCs with honeycomb-structured graphene counter electrodes.....	105
<b>Table 6.2.</b> The electrochemical characteristics of DSSCs with honeycomb structured graphene counter electrodes.....	109

## Preface

Graphene, a two-dimensional carbon nanomaterial, has been a rising star in material science due to its unique properties. Dye-sensitized solar cells (DSSCs) are currently the leading photovoltaic device (PV) among third generation solar cells due to their low production cost, ease of manufacturing and acceptable power conversion efficiency. Graphene are attracting much attention for the development of solar cells.

My PhD work was supervised by Professor Yun Hang Hu, who is the role model in my research study. The work in my PhD research has been published in 10 peer-reviewed journals. Professor Hu and I are the only two authors in 7 published papers. I performed all the materials synthesis, characterization, solar cell fabrication, data analysis and most writing in Chapter 3 “Effect of Oxygen Content on Structures of Graphite Oxides”, Chapter 4 “Electrolyte-induced Precipitation of Graphene Oxide in Its Aqueous Solution” and Chapter 6 “Three-Dimensional Honeycomb Structured Graphene as Counter Electrode Catalysts for Dye-sensitized Solar Cells”. I performed all the materials synthesis, most characterization (except TEM and XPS) and writing in Chapter 5 “Three-Dimensional Honeycomb-like Structured Graphene”. B. Hu contributed to the writing of 1.3 part of Chapter 1 “Background”. Dr. K. Sun contributed to the TEM data collection, while Dr. D.J. Stacchiola and Dr. F. Tao contributed to the XPS data collection and analysis in Chapter 5. I performed all the experiments and wrote papers under the guidance of Professor Hu for the work in this dissertation. This work would not be possible without the guidance, encouragement, and support from Professor Hu.

## **Acknowledgement**

First of all, I would like to thank my advisor with deepest gratitude, Professor Yun Hang Hu, for his guidance, encouragement, financial support, and help in making this dissertation possible. I would like to thank him very much for giving me the opportunity to pursue my Ph.D. studies. He is an outstanding role model not only as a scientist with hard-working ethic and extensive experiences but as a person with a great personality. I learned from him the way how to do research and how to behave with faith, responsibility, and confidence. I know what I have learned from him will benefit me throughout my career.

Next, I would like to thank all faculties and staffs in Materials science and Engineering department at Michigan Tech for helping me accomplish my Ph.D. study. I would like to thank my committee members: Professor Stephen Hackney, Professor Calvin White, and Professor Feng Zhao for reading my dissertations, listening to my presentation, and giving helpful suggestions. I also want to express my appreciation to: Professor Stephen Kampe, Professor Mark Plichta and Professor Jiann-Yang Huang for their guidance and encouragement. I also would like to thank Professor Dennis Meng and Professor Wenzhen Li, for their suggestions on my proposal defense.

I also want to thank Owen P. Mills, Edward A. Latitila, Paul Fraley, Patrick Quimby, Margaret Rothenberger, Beth Ruohonen, Ruth Kramer, Felica Nip, and Mick Small for their help and support in lab operations, experiments setting up, and materials characterizations.

Special thanks are given to my research group members, Dr. Lei Zhang, Dr. Yan Huo, Dr. Sanchai Kuboon, Dr. Junqing Zhang, Peifu Cheng, Bing Han, Wei Wei and Pubodee Ratana Arsanarom, for their assistance and help on my research projects. I also would like to thank my friends, Fengde Ma, Fei Li, Yan Yu, Ben Wang, Liwei Geng, Jie Zhou, Jingtuo Zhang, Weilue He, and other friends for all their supports and encouragements. I had the best time in Houghton with them.

Finally, I would like to thank my parents (Mr. Jirun Wang and Mrs. Yanfeng Shi), my sister, brother and other family members. They were always supporting me and encouraging me with their best wishes. Special thank is given to my husband Mr. Liang Yan, who always understand, help and encourage me during my life. Without him, I would never have accomplished what I have.

This dissertation is dedicated to all the people who had encouraged, supported, and helped me.

## List of Abbreviations

---

Abbreviation	Full name
2D	Two-dimensional
3D	Three-dimensional
BET	Brunauer-Emmett-Teller
CNT	Carbon nanotube
CE	Counter electrode
CEG	Chemical exfoliation of graphite
CV	Cycle voltammetry
CVD	Chemical vapor deposition
DW	De-ionized water
DSSC	Dye-sensitized solar cells
EDS	Energy dispersive spectroscopy
EELS	Electron energy loss spectroscopy
EIS	Electrochemical impedance spectra
EQE	External quantum efficiency
FE-SEM	Field emission scanning electron microscopy
FF	Fill factor

---



---

FTIR	Fourier transform infrared spectroscopy
FTO	Fluorine doped tin oxide
G	Graphene
GO	Graphene oxide
HOMO	Highest occupied molecular orbital
HOPG	Highly ordered pyrolytic graphite
HSG	Honeycomb structured graphene
IPCE	Incident photon-to-current conversion efficiency
ITO	Indium doped tin oxide
$J_{sc}$	Short-circuit current density
LUMO	Lowest unoccupied molecular orbital
OPV	Organic photovoltaic
P3HT	Poly(3-hexylthiophene)
P3OT	Poly(3-octylthiophene)
PB	1-pyrenebutyrate
PCBM	Phenyl-C61-butyric acid methyl ester
PCE	Power conversion efficiency ( $\eta$ )
PEDOT	Poly(3,4-ethylene-dioxythiophene)

---

---

PSS	Poly(styrenesulfonate)
SAED	Selected area electron diffraction
SWCNT	Single-walled carbon naotube
TCO	Transparent conductive oxide
TEG	Thermally exfoliated graphene
TEM	Transmission electron microscopy
TGA	Thermal gravimetric analysis
TGF	Transparent graphene films
TPD-MS	Temperature-programmed decomposition-mass spectrum
UV	Ultra-violate
$V_{oc}$	Open-circuit voltage
XPS	X-ray photoelectron spectroscopy
XRD	X-ray diffraction

---

## Abstract

Graphene, which is a two-dimensional carbon material, exhibits unique properties that promise its potential applications in photovoltaic devices. Dye-sensitized solar cell (DSSC) is a representative of the third generation photovoltaic devices. Therefore, it is important to synthesize graphene with special structures, which possess excellent properties for dye-sensitized solar cells.

This dissertation research was focused on (1) the effect of oxygen content on the structure of graphite oxide, (2) the stability of graphene oxide solution, (3) the application of graphene precipitate from graphene oxide solution as counter electrode for DSSCs, (4) the development of a novel synthesis method for the three-dimensional graphene with honeycomb-like structure, and (5) the exploration of honeycomb structured graphene (HSG) as counter electrodes for DSSCs.

Graphite oxide is a crucial precursor to synthesize graphene sheets via chemical exfoliation method. The relationship between the oxygen content and the structures of graphite oxides was still not explored. In this research, the oxygen content of graphite oxide is tuned by changing the oxidation time and the effect of oxygen content on the structure of graphite oxide was evaluated. It has been found that the saturated ratio of oxygen to carbon is 0.47. The types of functional groups in graphite oxides, which are epoxy, hydroxyl, and carboxyl groups, are independent of oxygen content. However, the interplanar space and BET surface area of graphite oxide linearly increases with increasing O/C ratio.

Graphene oxide (GO) can easily dissolve in water to form a stable homogeneous solution, which can be used to fabricate graphene films and graphene based composites. This work is the first research to evaluate the stability of graphene oxide solution. It has been found that the introduction of strong electrolytes (HCl, LiOH, LiCl) into GO solution can cause GO precipitation. This indicates that the electrostatic repulsion plays a critical role in stabilizing aqueous GO solution. Furthermore, the HCl-induced GO precipitation is a feasible approach to deposit GO sheets on a substrate as a Pt-free counter electrode for a dye-sensitized solar cell (DSSC), which exhibited 1.65% of power conversion efficiency.

To explore broad and practical applications, large-scale synthesis with controllable integration of individual graphene sheets is essential. A novel strategy for the synthesis of graphene sheets with three-dimensional (3D) Honeycomb-like structure has been invented in this project based on a simple and novel chemical reaction ( $\text{Li}_2\text{O}$  and  $\text{CO}$  to graphene and  $\text{Li}_2\text{CO}_3$ ). The simultaneous formation of  $\text{Li}_2\text{CO}_3$  with graphene not only can isolate graphene sheets from each other to prevent graphite formation during the process, but also determine the locally curved shape of graphene sheets. After removing  $\text{Li}_2\text{CO}_3$ , 3D graphene sheets with a honeycomb-like structure were obtained. This would be the first approach to synthesize 3D graphene sheets with a controllable shape. Furthermore, it has been demonstrated that the 3D Honeycomb-Structured Graphene (HSG) possesses excellent electrical conductivity and high catalytic activity. As a result, DSSCs with HSG counter electrodes exhibit energy conversion efficiency as high as 7.8%, which is comparable to that of an expensive noble Pt electrode.

# Chapter 1 Background\*

## 1.1 Photovoltaic cells

The current consumption of power is 13 terawatts (TW) worldwide. This amount is likely to increase to 30 TW by the year 2050 due to the increase in population and the improvement of living standards.<sup>1</sup> If fossil fuels are exploited to meet this requirement, the concentration of carbon dioxide in the atmosphere would be more than double, enhancing global warming. Therefore, it is a great challenge to provide the world with 30 TW power without contribution to environmental issues. Light from the sun is the ideal source of energy. The sun deposits 120 000 TW of radiation on the earth, which is the largest single available source of clean energy. Although technologies have been developed to exploit solar energy efficiently, they are still no economically viable alternative to fossil fuels.<sup>2</sup> So far, only about 5 GW power is generated from solar energy by solar cells.<sup>3</sup> A combination of increased energy prices and fears over global warming are pushing up demand for solar cells.<sup>4</sup>

Currently, the vast majority of solar cells on the market are single-junction silicon wafer devices including single crystal and multicrystalline silicon, which are known as first generation solar cells.<sup>5</sup> The second generation of photovoltaic material was developed to reduce the fabrication cost through the deposition of thin films,<sup>5</sup> particularly

---

\*The material contained in this chapter was previously published in journal *ChemSusChem*, 2010, 3, 782-796 by Hui Wang and Yun Hang Hu. See Appendix H for documentation of permission to republish this material.

Si thin films and Cu-based ternary semiconductor films, such as CdS/CuInSe<sub>2</sub> and Cu(In,Ga)Se<sub>2</sub>.<sup>6-10</sup> These thin film devices with a single junction constitute a rapidly growing segment of the solar cell market.<sup>5</sup> The third generation PVs are designed to exceed the limits of single-junction devices, to lead to a high efficiency and to reduce production costs. Various attempts to develop the third generation cells exist, such as multi-junction cells, intermediate-band cells, hot carrier cells, organic cells, and dye sensitized solar cells.<sup>1,4,5</sup>

### **1.1.1 Crystalline Si solar cells**

Silicon solar cell was firstly developed by Bell Laboratories in 1954 with an efficiency of 6%.<sup>11</sup> The efficiency was rapidly increased to 10% and then to 30%. The development of Si solar cell benefited greatly from the high standard of silicon technology, which provides high quality single crystal silicon. General silicon crystal growth techniques include Czochralski (Cz) and float zone technique.<sup>12</sup> In Czochralski growth process, a seed of single-crystal silicon contacts the top of molten silicon and is slowly withdrawn under rotation. As the seed is slowly raised, atoms of the molten silicon solidify in the pattern of the seed and extend the single-crystal structure. In float zone technique, a rod of highly purified polycrystalline silicon is melted by induction heating and a single crystal is pulled from this molten zone. Float zone material is exceptional purity with very low oxygen contamination, but it is much more expensive than Czochralski technique. To further reduce the cost of a solar cell, polycrystalline silicon technology was developed,<sup>13</sup> in which silicon blocks are sawn into bars and then

wafers. Polycrystalline silicon is cheaper than single crystal materials but yields solar cells with a lower efficiency due to the grain boundaries.

The main drawback of Si crystalline solar cell is associated with their indirect optical band gap that requires a thick active layer for the solar conversion and thus costly fabrication of large area materials. Furthermore, those cells suffer many efficiency losses for energy conversion, such as “red losses” that photons with energies below the band gap of the device cannot be absorbed and “blue losses” that photons with energies above the band gap lose their excess energy as heat.

### **1.1.2 Thin film solar cells**

Thin film solar cells, also known as the second generation solar cells, include amorphous silicon solar cells, copper indium (gallium) diselenide (CIGS) solar cells, cadmium telluride (CdTe) solar cells, and so on. The second generation devices share the same performance restrictions as the first generation ones.

Amorphous silicon (a-Si) is silicon that appears to be solid but has no long-range crystal structure. The action between photons and silicon atoms occurs more frequently in amorphous silicon than in crystal silicon. As a result, amorphous silicon absorbs solar radiation 40 times more effectively than single-crystal silicon. For this reason, the amorphous silicon cells can employ thin silicon film (about 1  $\mu\text{m}$  thick). The common used method to deposition thin a-silicon film is plasma enhanced chemical vapor deposition (PECVD). The first publications on a-Si relevant for solar cells can date back to 1970s.<sup>14,15</sup> Until now, the efficiency of a-Si solar cells are around 15% for

laboratories<sup>16,17</sup> and 6-8% for module cells. Amorphous silicon solar cells suffer from the issue of light induced degradation caused by Staebler-Wronski effects.<sup>18</sup>

Copper indium diselenide (CIS,  $\text{CuInSe}_2$ ), can absorb 99% of sunlight in its first micrometer. Furthermore, the introduction of small amounts of gallium into the CIS layer can boost its band gap and improve the voltage and thus the efficiency of the device. Typical CIGS solar cells are depositing CIGS films on Mo coated glass substrates at a substrate temperature above 500 °C. The heterojunction is formed by chemical deposition of a thin CdS layer from a solution containing Cs-ions. High efficiency approaching 20% of CIGS solar cells was reported for laboratory scale devices.<sup>19</sup>

Thin-film solar cell based on CdTe was first reported by Cusano<sup>20</sup> in a p-Cu<sub>2</sub>Te/N-CdTe heterojunction and succeeded in obtaining 6% efficiency. CdTe is a nearly ideal material for thin-film photovoltaics because not only its ideal optical band gap close to the optimum for solar energy conversion but also it is easy for thin-film deposition processes. The active layers of CdTe based solar cells are deposited on SnO<sub>2</sub> or indium tin oxide coated glass. High efficiency cells use very thin chemically deposited CdS. The fabrication of the CdTe-CdS heterojunction is one of the keys to efficient devices.

### **1.1.3 Dye-sensitized solar cells**

Third generation PVs, which represent the cutting edge of solar technologies, are designed to exceed the limits of single-junction devices for a high efficiency and a low production cost.<sup>5</sup>



Dye-sensitized solar cells (DSSCs) are currently the leading photovoltaic device with regards to third generation PVs due to its low production cost, ease of manufacturing and acceptable power conversion efficiency.<sup>21,22</sup> Since a prototype for DSSCs was reported in 1991 by O'Regan and Gratzel,<sup>21</sup> they have aroused an intense interest.<sup>23-26</sup> As shown in Fig. 1, a typical dye-sensitized solar cell consists of a dye, a nanocrystalline TiO<sub>2</sub> film at the photoanode, a counter electrode (CE) and an electrolyte with a redox couple in the liquid or solid state.<sup>27-29</sup> In principle, photoexcitation of the dye in a DSSC leads to a rapid electron injection to the conduction band of the semiconductor (i.e. TiO<sub>2</sub>), followed by electron transfer to the photoelectrode, where the original state of the dye is restored by electron donation from the electrolyte. The collected electrons in the photoelectrode are transported through an external circuit to the counter electrode, and the circuit is completed through regenerating the electrolyte at the counter electrode. Although the solar power conversion efficiency of DSSCs is lower than that of classic crystalline silicon cells, there is a high potential for improvement of the energy conversion efficiency.

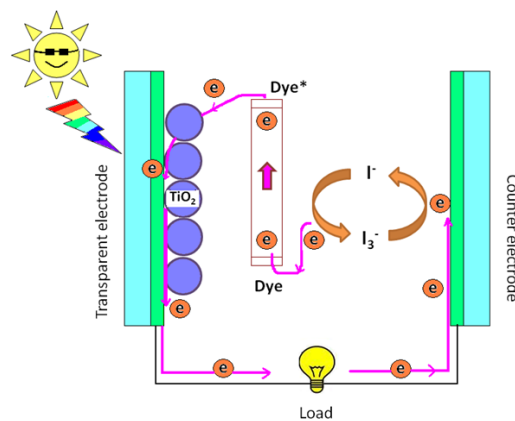


**Fig.1.1. Working principle of a DSSC.**

## 1.2 Graphene

Because of the bonding flexibility of carbon, carbon-based materials exhibit various structures with a large variety of physical properties. Three-dimensional carbon allotropes (graphite and diamond) have been well-known for a long time. The zero-dimensional carbon fullerenes and one-dimensional carbon nanotubes were discovered within the last 25 years. However, studies of two-dimensional graphene, which is a one-atom thick layer made out of carbon atoms in a hexagonal “honeycomb” carbon lattice, had been neglected.<sup>30</sup> Graphene constitutes the basic structure of other carbon allotropes, namely, graphite, fullerenes, and nanotubes, which can be formed by stacking, wrapping and rolling-up graphene, respectively. The properties of graphene have been studied theoretically for about 60 years.<sup>31-37</sup> About 25 years ago, it was predicted that graphene could represent a condensed matter analogue of quantum electrodynamics in two spatial and time dimensions.<sup>34-36</sup> However, such a significant prediction did not attract much attention because it was generally recognized that isolated graphene could not exist.<sup>38-40</sup> This situation was completely changed with the demonstration of exfoliated graphene in 2004.<sup>30,41</sup> Within the last five years, graphene has become an exciting and promising model system for two-dimensional solids.<sup>42-49</sup> This material has many exciting and unique properties, such as high carrier mobility, a weak dependence of mobility on carrier concentration and temperature, and an unusual quantum Hall effect.<sup>42,43,50</sup>

### 1.2.1 Preparation

There are two types of approaches to synthesize graphene: (1) physical approach—“mechanical exfoliation” and (2) chemical approach—“epitaxial growth” (including chemical vapor deposition) and “reduction of graphite oxide”.

Single-layer graphene is generally prepared by mechanical exfoliation, in which highly oriented pyrolytic graphite (HOPG) is peeled using scotch tape and the subsequent release of the graphene flake on Si/SiO<sub>2</sub> after the tape is removed.<sup>30</sup> This simple approach can produce graphene flakes with dimensions of 70–100 μm, which has afforded the evaluation of the properties of single-layer graphene or bilayer graphene.<sup>51</sup> However, the mechanical exfoliation of graphene is not suitable for large-scale synthesis of a single- or few-layer graphene due to its low yield.

The epitaxial growth process has also been exploited to prepare single-layer graphene via the sublimation of Si of SiC or the catalytic decomposition of hydrocarbon (or carbon oxide). The epitaxial growth of graphene can be carried out by heating a SiC substrate in ultra high vacuum at a high temperature (typically greater than 1000 °C; i.e., a sublimation of Si atoms from the surface results in the formation of a graphene sheet on the top of SiC).<sup>51-56</sup> The number of graphene layers can be controlled by the time or temperature of the heating treatment. This process can provide a higher yield with much less defects than the exfoliation method, but cannot easily fabricate a large-area graphene. By using catalytic decomposition of hydrocarbons or carbon oxide, graphene can also be grown epitaxially on metal surfaces.<sup>57-60</sup> When the metal surfaces are heated, hydrocarbon (or carbon oxide) decomposes into carbon atoms and hydrogen gas (or

oxygen gas), and the carbon atoms then form a graphene monolayer. This approach has been well-known as chemical vapor deposition (CVD).<sup>61-66</sup> However, the large amount of carbon sources absorbed on metals usually generates thick graphite crystals rather than thin graphene films. To solve this issue, low pressure or high dilution of hydrocarbons have been used to form thin graphene films on metals.<sup>67-69</sup> Furthermore, the obtained graphene films on a transition metal surface can be transferred to other substrates via metal etching. For example, Kim et al. deposited thin layers of nickel (thinner than 300 nm) on a SiO<sub>2</sub>/Si substrate using an electron-beam evaporator, followed by heating to 1000 °C under an argon atmosphere.<sup>67</sup> At 1000 °C, the obtained Ni/SiO<sub>2</sub>/Si was treated by a reaction gas mixture (CH<sub>4</sub>/H<sub>2</sub>/Ar=50:65:200 standard cubic centimeters per minute) flow and then rapidly cooled to room temperature by argon flow. This produced the mono- and bilayer graphene film on the nickel layer. Furthermore, after etching nickel and the SiO<sub>2</sub> layers, the isolated graphene film was transferred to the Si substrate. Therefore, by using the pre-patterned nickel substrate, one can transfer various sizes and shapes of graphene film to an arbitrary substrate, which is very important for device applications. Recently, this approach was employed to prepare large-area, continuous, few-layered graphene as anodes for organic photovoltaic devices.<sup>70</sup>

The reduction of graphite oxide has been a promising route to achieve mass production of graphene through three steps: oxidation of graphite, exfoliation of graphite oxide into graphene oxide, and reduction of graphene oxide.<sup>71,72</sup> As early as in 1859, Brodie explored oxidation of graphite by adding potassium chlorate (KClO<sub>3</sub>) into a slurry of graphite in fuming nitric acid (HNO<sub>3</sub>).<sup>73</sup> The obtained graphite oxide had a chemical composition of C<sub>2.19</sub>H<sub>0.80</sub>O<sub>1.00</sub>. About 100 years later, Hummers and Offeman developed

an alternate oxidation method by reacting graphite with a mixture of potassium permanganate ( $\text{KMnO}_4$ ) and concentrated sulfuric acid ( $\text{H}_2\text{SO}_4$ ), achieving similar levels of oxidation (C/O ca. 2:1).<sup>74</sup> Although other slightly modified processes have been developed, these two methods are the primary routes for the synthesis of graphite oxide.<sup>72</sup> A variety of thermal and mechanical approaches can be used to exfoliate graphite oxide to single-layer graphene oxide (GO), but sonicating and/or stirring graphite oxide in a solvent are most common. Finally, the single-layer graphene oxide can be reduced by hydrazine or other reducing agents, resulting in single-layer graphene sheets.<sup>71,75-77</sup> In addition, graphite oxide can also be reduced by high-temperature treatment,<sup>77-81</sup> electrochemical reaction,<sup>82,83</sup> and photographic camera flash.<sup>84</sup>

### 1.2.2 Physical properties

Graphene is a unique mixture of a semiconductor (zero density of states) and a metal (gaplessness) with unusual properties. It has extraordinary electronic excitations described in terms of Dirac fermions that move in a curved space.<sup>37</sup> Unlike in the case of metals or common semiconductors, the electrons in graphene, which obey the Dirac equation rather than the Schrödinger equation, are almost insensitive to disorder and electron–electron interactions. Although the typical carrier mobility at room temperature is about  $15,000 \text{ cm}^2 \text{ V}^{-1} \text{ s}^{-1}$ ,<sup>45</sup> it can reach  $200,000 \text{ cm}^2 \text{ V}^{-1} \text{ s}^{-1}$  in suspended graphene at a charge carrier concentration of  $4 \times 10^{-9} \text{ cm}^{-2}$ .<sup>85</sup> As a result, the room temperature mean-free path for ballistic transport is about 300–500 nm. Although the resistivity of graphene is strongly dependent on the gate voltage, it is not quite sensitive to temperature change.<sup>86,87</sup> The important properties of graphene are summarized in Table 1.

In contrast to the extensive effort on electrical transport, optical study of graphene has been limited.<sup>88-96</sup> It was shown that the optical transparency ( $T_r$ ) of graphene is dependent on its optical conductivity  $\sigma(\omega)$  where  $\omega$ =frequency and  $c$ =the light velocity:<sup>97,98</sup>

$$T_r(\omega) = [1 + 2\pi\sigma(\omega) / c]^{-2}$$

Furthermore, Geim et al. experimentally found that the optical transparency of graphene was 0.977, which is independent of  $\omega$ , in the visual regime (450 nm<wavelength<750 nm).<sup>99</sup> This experimental observation could be theoretically explained by describing graphene as noninteracting Dirac particles with optical conductivity as follows:<sup>100</sup>

$$\sigma^{(0)}(k_B T \leq \omega \leq D) = \frac{\pi e^2}{2h}$$

where  $D$  is the upper cutoff energy for the linear dispersion and  $T$  is the temperature. Assuming  $\sigma = \sigma^{(0)}$  gives

$$Tr(\omega) = (1 + \pi\alpha_{QED} / 2)^{-2}$$

where,  $\alpha_{QED} = e^2 / (hc) = 1/137.035999$ , which is the fine structure constant of quantum electrodynamics. Therefore, one can obtain:

$$Tr(\omega) = 0.9774629$$

This is in excellent agreement with the experimental measurements, indicating that the optical transparency of noninteracting graphene is solely determined by the value of the fine structure constant of quantum electrodynamics. Furthermore, the opacity, which is 2.3% for a single graphene layer, was found to increase with membrane

thickness (i.e., each graphene layer adds another 2.3%). Therefore, such a unique optical property with its unusual electrical property constitutes an ideal candidate as transparent electrodes for solar cells. Furthermore, the ability of a single-layer graphene to absorb 2.3 percent of incident light over a broad wavelength range can allow it to be used as ultrafast transistor-based photodetectors.<sup>95</sup>

### **1.2.3 Chemical properties**

Graphene is currently at the center of attention in physics. However, its chemistry has not yet been largely explored. Currently, the knowledge about graphene chemistry is mainly limited to the adsorption and desorption of atoms, molecules, and functional groups, such as H, K, NO<sub>2</sub>, NH<sub>3</sub>, and OH.<sup>49</sup> Adsorbed molecules, which are weakly attached to graphene surface, can act as donors or acceptors.<sup>46,61</sup> In this case, the high conductivity of graphene can be maintained.<sup>46</sup> However, the electron-donor molecules decrease the conductivity of graphene, whereas the electron-acceptor molecules increase the conductivity.<sup>75</sup> Such a conductive response of graphene to its chemical environment can allow it to be exploited as an effective sensor to detect individual gas molecules.<sup>46</sup> In contrast, the strong bonding of an atom or group (such as H and OH) to graphene can destroy its conductivity, generating its poorly conductive derivatives, such as graphene oxide<sup>47</sup> and hydrogenated graphene.<sup>48</sup> Furthermore, the partial substitution of C atoms in a graphene sheet by B or N could strongly affect the structure and properties of graphene.<sup>61,75</sup>

Although graphite consists of graphene sheets, they should have different chemical properties. Graphite possesses a flat surface, however, graphene typically

exhibits nanometer-scale corrugation.<sup>44a</sup> Such associated strain and curvature can markedly enhance the local reactivity of graphene, such as fullerenes. Furthermore, the absence of an obscuring contribution from the bulk makes properties of graphene more sensitive to chemical inductions.<sup>46</sup>

The functionalization of graphene can be expected to play an important role in the modifications of graphene for specific applications. For example, the graphene paper is porous, fragile, and metallic if it is made of nonfunctionalized graphene flakes<sup>44b</sup> and dense, stiff, and strong if it is made of graphene oxide.<sup>47</sup>

## **1.3 Graphene for photovoltaic solar cells**

### **1.3.1 Transparent electrode**

Organic and inorganic thin film solar cells are being pursued as viable alternatives to silicon solar cells. A critical aspect of these solar cells is the current conduction across the illuminated side of the device in the transparent conductor (TC), namely, the illuminated side (electrode) should be transparent with good conductance. Currently, two materials can meet those requirements: indium tin oxide (ITO) and fluorine tin oxide (FTO). Although ITO is more effective than FTO, ITO still has several drawbacks:<sup>78, 81, 101,103</sup> (1) limited resource of indium on the earth; (2) the ion diffusion from ITO into polymer layers in organic solar cell, which reduces overall efficiency; (3) the poor transparency in near infrared region, which restricts their ability to gather a wider range of solar energy; (4) instability of ITO at acid or base conditions; and (5) the brittleness of



ITO, which limits its application for flexible organic photovoltaics. To solve these issues, searching for new window electrodes with low cost and better performance is being focused on carbon materials.

To obtain effective materials with low sheet resistance and high optical transparency in the visible and infrared spectral range, carbon nanotube (CNT) network film has been explored for applications as electrodes of solar cells.<sup>103-106</sup> However, the conductivity versus transparency values attained by using the films of carbon nanotubes are still much lower than those of ITO thin films, due to the tendency of suspended CNTs to form bundles. Another drawback is the high surface roughness of the CNT film, which may limit its further application in commercial products. In addition, CNTs are still an expensive material.

Several research groups evaluated the relationships between preparation conditions and the properties of graphene films.<sup>70, 68, 103, 107, 108</sup> Wang et al. found that the graphene films, which were fabricated via the bottom-up approach using a monodispersed molecular nanographene as building units, showed stronger interactions with the substrate than that of graphite oxide-induced film.<sup>102</sup> Furthermore, the graphene films (prepared by using bottom-up approach) with thicknesses of 4, 12, and 22 nm exhibited transparencies of 90, 80, and 66% at a wavelength of 500 nm, respectively. Such transparent graphene films (TGF) were evaluated as window electrodes in organic solar cells, which were fabricated using a blend of poly(3-hexyl)thiophene (P3HT) and phenyl-C61-butyric acid methyl ester (PCBM) (Fig.1.2 a and b). The photoactive composite layer was sandwiched between a TGF/quartz and an Ag electrode. The TGF

on quartz had a sheet resistance of 18 k $\Omega$ /sq and a transmittance of 85% at a wavelength of 500 nm. When the devices were illuminated with a monochromatic light, the highest external quantum efficiency (*EQE*) of around 43% was achieved at a wavelength of 520 nm (Fig.1.2 c). This efficiency is comparable to the highest *EQE* value of 47% for a reference device fabricated by replacing TGF/quartz with ITO/glass as an anode. The current-voltage (*I-V*) characteristics of the device showed a distinct diode behavior under monochromatic light with a wavelength of 510 nm (Fig.1.2 d). Furthermore, as shown in Table 1.1, one can see that, under the monochromatic light with a wavelength of 510 nm, the power conversion efficiency of the TGF based cell was 1.53%, which was almost the same as that of ITO-based cell (1.5%). However, under the illumination of the simulated solar light, the overall efficiency of the TGF-based cell (0.29%) was lower than that of the ITO-based cell (1.17%). The open-circuit voltage of the TGF-based cell was comparable to that of ITO based cells, indicating that the graphene has an appropriate work function for this type of organic solar cells. The relative low short-circuit photocurrent density and filling factor of the cell may be due to the high resistance of the as prepared graphene films.<sup>102</sup>

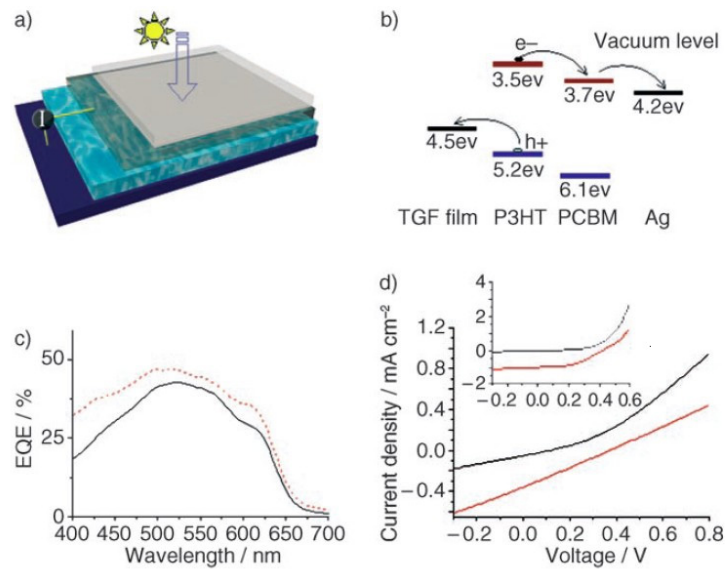


**Fig.1.2. Structure and performance of solar cell based on graphene electrodes.** (a) Structure of the solar cell (the four layers from bottom to top are Ag, a blend of P3HT and PCBM, TGF, and quartz, respectively); (b) A schematic representation of charge transfer and transport as an energy level diagram; (c) EQEs of a TGF-based cell (solid black curve) and an ITO-based cell (red dashed curve); (d) I-V curves of a TGF-based cell and an ITO-based cell (inset) illuminated under simulated solar light (red curve) and with monochromatic light of wavelength 510 nm (black curve).<sup>102</sup> (See Appendix A for permission to republish this material.)

**Table.1.1 Performances of the solar cells based on TGF and ITO anodes.<sup>102</sup>**

Light	Anode	$J_{sc}$ (mA/cm <sup>2</sup> )	$V_{oc}$ (V)	$FF$	$\eta$ (%)
Monochromatic light of 510 nm	ITO	0.04	0.14	0.3	1.5
	TGF	0.052	0.13	0.23	1.53
Simulated solar light	ITO	1.0	0.41	0.48	1.17
	TGF	0.36	0.38	0.25	0.29

Note:  $V_{oc}$ —open-circuit voltage,  $J_{sc}$ —short-circuit current density,  $FF$ —fill factor, and  $\eta$ —power conversion efficiency.

Chen and his co-workers examined the effects of preparation conditions and treatments on graphene films. They found that the thin films (~3 nm thick), which were fabricated by spin-coating with a low GO-concentration solution (<2 mg/mL), were continuous and the edges of individual sheets could be distinguished.<sup>78</sup> In contrast, the thicker films (~20 nm) coated from high GO-concentration solutions (12-15 mg/mL) were rougher with extensive networks of long and broad wrinkles across the film surface. Furthermore, chemical and thermal reduction treatments showed effects on the morphology of GO films. The AFM images showed that, after the chemical reduction of ~3 nm GO film via exposure to an atmosphere of hydrazine monohydrate vapor at 40 °C for 18 h and dried in a vacuum oven at 80 °C for 3 h, individual well-defined-sheets were still present and the overall roughness was comparable to that of the untreated film. It was found that the sheet resistance followed the order: unreduced graphene > graphene reduced by hydrazine vapor > graphene reduced by hydrazine plus 400 °C annealing > graphene graphitized at 1100 °C. Furthermore, XPS measurements showed that the conductivity enhancement from the film treated with hydrazine to those treated with the combination of hydrazine and 400 °C annealing was due to a chemical difference instead of the improvement of sheet contact during the annealing step. Those graphene films (4~7 nm thick), which had the transmittance of 85~95% and the sheet resistance of 100~500 kΩ/sq, were evaluated as transparent conductive anodes for organic photovoltaic (*OPV*) cells.<sup>107</sup> For a typical cell with layer structure of 35 nm CuPc/50 nm C<sub>60</sub>/10nm BCP on graphene or ITO (where the graphene film was reduced by vacuum annealing), the short-circuit current density ( $J_{SC}$ ), open circuit voltage ( $V_{OC}$ ), fill factor

(*FF*), and power conversion efficiency (*PCE*) were 2.1 mA/cm<sup>2</sup>, 0.48 V, 0.34, and 0.4% for the cell with graphene and 2.8 mA/cm<sup>2</sup>, 0.47 V, 0.54, and 0.84% for the cell with ITO respectively. The lower efficiency of the graphene-based cell is mainly due to its lower  $J_{sc}$  and *FF*, which are associated with the high sheet resistance of the graphene film.

Wang et al. synthesized a large-area graphene film on Ni-coated SiO<sub>2</sub>/Si wafer using chemical vapor deposition (CVD) process.<sup>70</sup> For 6~30 nm thick graphene film, the average sheet resistance varied from 1350 to 210 Ω/sq, which are lower than that of chemically fabricated graphene oxide films by a factor of 2~3. However, the transparency (72~91% in the visible light wavelength range) and conductivity of the CVD graphene are still lower than those of ITO, which had sheet resistance of 10 Ω/sq on glass (with almost 80% transparency) and 100-300 Ω/sq on polyethylene terephthalate. Furthermore, they exploited the graphene film as an anode for the organic photovoltaic device. As shown in Fig.1.3, the performance of photovoltaic cell was measured by using a simulated illumination (AM1.5G) under nitrogen atmosphere. Its open-circuit voltage ( $V_{oc}$ ), short-circuit current density ( $J_{sc}$ ), and fill factor (*FF*) were 0.32V, 2.39 mA/cm<sup>2</sup>, and 27%, respectively. This indicates that the cell with the CVD graphene anode had a poor performance. This happened because the hydrophobic property of graphene cannot form the uniform coating of PEDOT/PSS. To improve the surface wettability, the graphene anode was modified by UV/ozone treatment, in which the aromatic rings of graphene can be turned into hydrophilic ones via introducing C=O groups. Indeed, after the UV treatment of graphene film for 10 min, they can obtain  $V_{oc}$  of 0.55 V,  $J_{sc}$  of 5.56 mA/cm<sup>2</sup>, and *FF* of 24.3%. As a result, its efficiency was increased to 0.74%. In this case, although the surface was rendered more hydrophilic by the presence of oxygenated

groups, the good conducting properties of graphene were compromised, due to the disruption of the aromatic structures caused by covalent bonding with oxygen groups. Therefore, noncovalent functionalization with pyrene buanoic acid succidimidyl ester (PBASE) was employed to modify graphene. It was found that graphene anode modified by self-assembled PBASE exhibited excellent performance characteristics ( $V_{oc} = 0.55$  V,  $J_{sc} = 6.05$  mA/cm<sup>2</sup>,  $FF = 51.3\%$ , and  $PCE = 1.71\%$ ). At the same condition, the photovoltaic performance of a reference device made with ITO anode showed  $V_{oc}$ ,  $J_{sc}$ ,  $FF$  and  $\eta$  of 0.56 V, 9.03 mA/cm<sup>2</sup>, 61.1%, and 3.10%, respectively. This indicates that the solar cell with a PBASE-modified graphene anode has reached 55.2%  $PCE$  of a structurally identical cell with ITO anode.

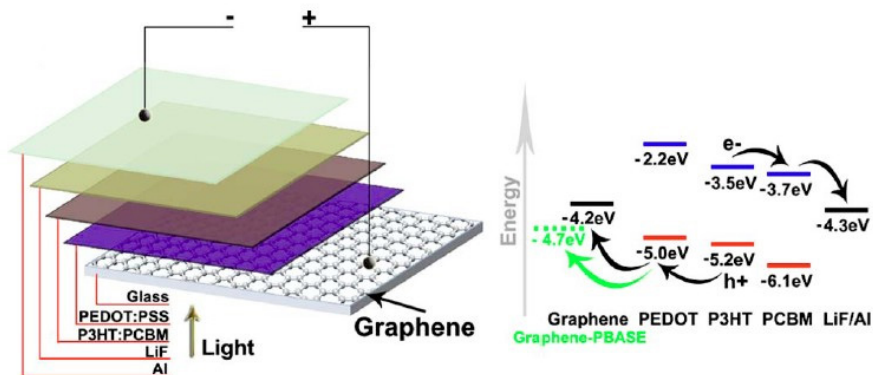


**Fig.1.3. The fabricated device with structure graphene/PEDOT:PSS/P3HT:PCBM/LiF/Al.**<sup>70</sup>

(See Appendix B for permission to republish this material.)

The oxidation of graphite into graphene oxide (GO) sheets could cause initial structural defects on the basic carbon sheets.<sup>109</sup> Liang et al. developed a novel procedure using acetylene (C<sub>2</sub>H<sub>2</sub>) as a supplemental carbon source to repair the structural defects

within GO sheets, leading to the enhancement of graphitization of synthesized graphene electrodes.<sup>108</sup> Their Raman spectra and X-ray photoelectron spectroscopy (XPS) showed that the graphitization degree of the reduced GO films (about 3.5 nm thick) fabricated on a quartz substrate was higher in acetylene ( $C_2H_2$ ) than in inert argon. Furthermore, the assistance of acetylene enhanced electrical conductivity of graphene film by a factor of 2~4 compared to argon (Fig.1.4). For the reduced GO film, which was fabricated via thermal treatment at 1000 °C under acetylene ( $C_2H_2$ ) atmosphere, had a conductivity of up to 1425 S/cm with an optical transmittance of more than 70% at 500 nm. This value is significantly higher than those previously reported for graphene-based electrode materials.<sup>78,81</sup> This great enhancement of conductivity confirms the improvement of the graphene structural quality via acetylene-assisted thermal treatment. This happened because acetylene can provide a carbon-rich atmosphere to mend the pristine defects in GO sheets. Furthermore, abundant carbons in radical form may also inhibit the loss of carbon atoms from the frameworks during the heat treatment to remove oxygen-containing groups.<sup>110</sup>

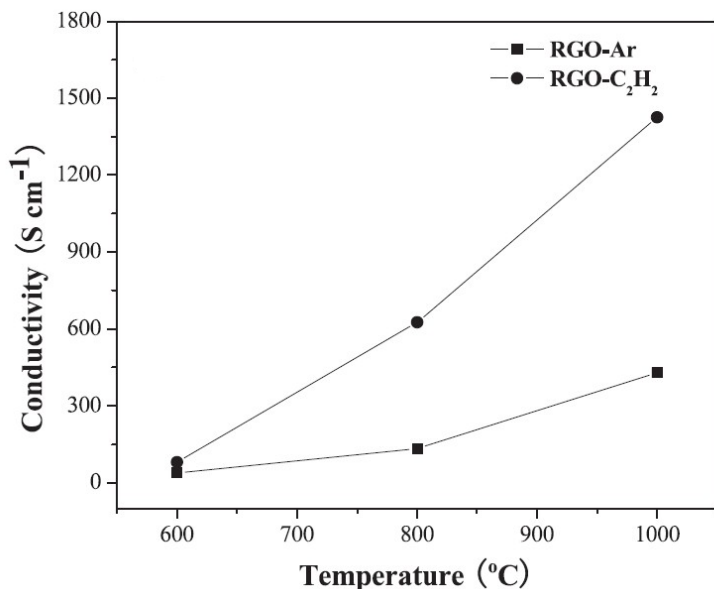


**Fig.1.4. The conductivity of reduced GO films fabricated by spin-coating on quartz with thermal reduction in the temperature range of 600-1000 °C.<sup>108</sup> (See Appendix C for permission to republish this material.)**

The stability of electrode is important for solar cells. Zhao et al demonstrated the excellent stability of solar cells with graphene electrodes.<sup>111</sup> They prepared transparent, conductive, and uniform graphene films as electrodes for the electrochromic devices of polyaniline. Polyaniline films on both graphene and the indium tin oxide (ITO) electrodes showed similar electrochemical and spectroelectrochemical properties. However, graphene electrodes exhibited much higher electrochemical stability than ITO in aqueous acidic electrolytes. This happened because ITO electrodes are unstable in aqueous electrolytes with low pH values due to the gradual dissolution of their oxide coatings. As shown in Table 3, in the first cycle of electrochromic test, the device with PANI-ITO electrode performed better than that with PANI-Graphene electrode. However, after 300



cycles, the performances of PANI-ITO device declined greatly, its optical contrast value halved, and the switching time increased from 0.6 s to longer than 7 s. In contrast, the performance of PANI-Graphene device was quite stable, namely, its optical contrast and electrochromic efficiency decreased only by 10 and 14%, respectively, and the switching time remained almost unchanged. For practical applications as electrochromic windows and displays, switching cycles of the device should be more than 10<sup>4</sup> with the switching time of 0.1–10 s.<sup>112</sup> Therefore, graphene electrode is more suitable than ITO for the PANI electrochromic devices.

To evaluate the mechanical stability of graphene electrode, Tung et al. prepared graphene-carbon nanotube (G-CNT) hybrid electrodes by spin-coating G-CNT on poly(ethylene terephthalate)(PET).<sup>113</sup> For the densest film, a resistance was as low as 44  $\Omega/\text{sq}$  with 55% transmittance. The effect of bending a G-CNT film and a standard ITO film (on PET electrodes) on their current-voltage characteristics was examined (Fig.1.5). After bending to 60° more than 10 times, the resistance of the brittle ITO film was increased by a factor of 3, whereas the G-CNT electrode remained almost unchanged. This indicates that G-CNT hybrid electrodes have a much better mechanical stabilities than ITO electrodes.

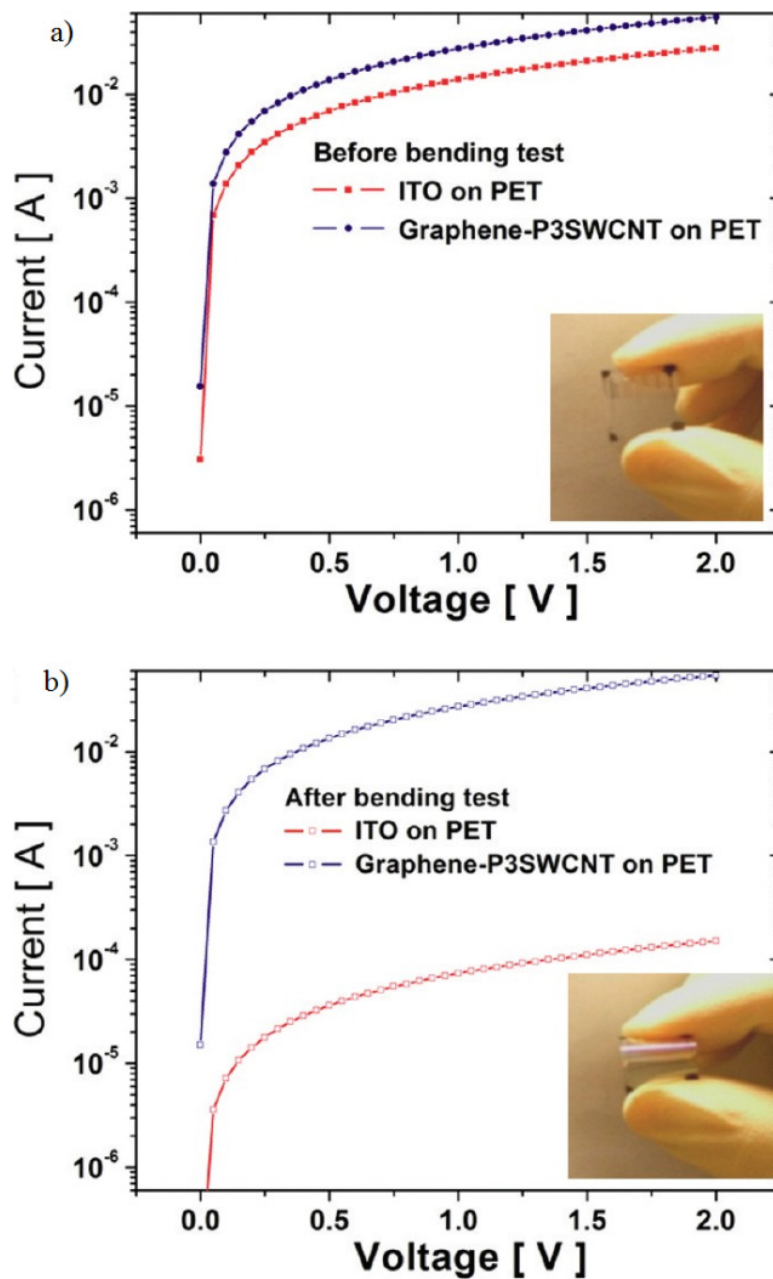


Fig. 1.5. Electrical measurements of G-CNT and ITO films (a) before and (b) after 10 times of bending by  $60^\circ$ .<sup>113</sup> (See Appendix D for permission to republish this material.)

### **1.3.2 Functionalized Graphene as Hole Collecting Materials**

It was demonstrated that the introduction of Cl into singlewalled carbon nanotube (SWCNT) thin films resulted in p-type doping and enhanced sheet conductance.<sup>114</sup> A similar property could be expected for graphene. Recently, the possibility of Cl-doped graphene film as hole collecting materials was explored.<sup>115</sup> Eda et al. reported the preparation of transparent and conductive graphene film by vacuum filtration of graphite oxide to form a film, followed by hydrazine vapor reduction and low temperature annealing under nitrogen to reduce the resistance of the film.<sup>115</sup> They found that the treatment of the film with  $\text{SOCl}_2$  reduced the resistance by a factor of 5, which occurred because the film obtained p-type doping with Cl of  $\text{SOCl}_2$ . The obtained graphene film was fabricated into organic solar cells with PEDOT:PSS, poly(3-hexylthiophene) (P3HT) and phenyl-C61-butyric acid methyl ester as active material and aluminum as a top electrode. The efficiency of the device was approximately 0.1%. In contrast, the device fabricated with PEDOT: PSS without the Cl-doped graphene film did not work, which was attributed to the hole-collecting role of the Cl-doped graphene. However, no direct evidence was obtained to confirm such a hole collection in the Cl-doped graphene.

### **1.3.3 Functionalized Graphene as Electron-Accepting Material**

Polymer-based organic photovoltaic (OPV) materials are being developed for a solution-processable, flexible, and lightweight solar energy conversion platform. In the conjugated polymers that have highly conjugated p-systems, an electron is excited (by photon absorption) from the highest occupied molecular orbital (HOMO) to the lowest

unoccupied molecular orbital (LUMO), resulting in a strongly bound electron-hole pair. The separation of the electron-hole pair can be achieved by creating a heterojunction with an acceptor material that has an electron affinity (EA) larger than that of the polymer, but still smaller than its ionization potential (IP). Furthermore, the acceptor material should have a lower HOMO level than the conjugated polymer so that the photoexcited conjugated polymer can transfer an electron to the acceptor material and retain the hole in its valence band.<sup>116</sup> Two types of heterojunctions have been widely employed: bilayer planar heterojunction structure<sup>117</sup> and an intermixed bulk heterojunction (BHJ) structure.<sup>118,119</sup> The efficiency of the planar heterojunction device is limited by the exciton diffusion length and the interface area between donor and acceptor. However, such an exciton diffusion bottleneck can be effectively solved by applying the BHJ structure, in which all excitons are formed within the exciton diffusion length in an interpenetrating network of the donor and acceptor materials.<sup>120</sup> Furthermore, compared to the planar heterojunction, the BHJ has a larger interface area, which can increase the efficiency of the heterojunction.<sup>121</sup> In the recent years, various BHJ photovoltaic devices have been made of polymer composites,<sup>119,122–125</sup> polymers with dyes,<sup>126–128</sup> polymers with fullerenes, and small-organic-molecule composites.<sup>129–131</sup> Furthermore, research efforts in solution-processed OPV materials have been dominated by using a fullerene derivative, [6, 6]-phenyl C61-butyric acid methyl ester (PCBM), as the electron acceptor. So far, the most successful OPV cells have had the BHJ structure consisting of soluble poly(3-hexylthiophene) (P3HT) and/or poly(3-octylthiophene) (P3OT) as a donor and PCBM as an acceptor.<sup>132–137</sup> However, the power conversion efficiency of those OPV devices is still low compared to that of conventional inorganic devices. Therefore, new

materials for both donor and acceptor with better HOMO/LUMO matching, stronger light absorption, and higher charge mobility are much needed. This has prompted the studies of carbon nanomaterials as acceptors, including single- and multiwalled carbon nanotubes (SWNTs and MWNTs).<sup>138-142</sup> However, some unfavorable factors, such as their insolubility, impurities, and bundling structure, greatly limit the performance of carbon nanotube-based devices. Recently, functionalized graphene has been explored as an electron acceptor for OPV devices. Chen and his co-workers found that the P3HT solution showed strong photoluminescence between 525 and 750 nm with excitation at 422 nm.

However, the photoluminescence was remarkably reduced after the solution-processable functionalized graphene (SPFG) was introduced.<sup>143</sup> These results show that the excited fluorophore in the P3HT backbone was quenched by the electronic interactions at the P3HT/SPFG interfaces. This efficient quenching of the photoluminescence emission indicates that SPFG can be used as an effective electron-acceptor material for organic photovoltaic applications. Indeed, the overall performance of the P3HT/SPFG-based photovoltaic device was much higher than that of the control device based on pristine P3HT. This indicates that there was an obvious charge transfer from the P3HT donor to the SPFG acceptor. Under illumination, the PCE,  $J_{sc}$ ,  $V_{oc}$ , and FF were 0.005%, 0.04 mA, 0.42 V, and 0.27 for the device based on pristine P3HT and 0.15%, 0.46 mA, 1.1 V, and 0.30 for the P3HT/SPFG-based cell, respectively. Furthermore, the devices with 2.5, 5, 10, and 15 wt% SPFG content had power conversion efficiencies of 0.09, 0.1, 0.15, and 0.13%, respectively, indicating that the peak efficiency was reached at 10 wt% SPFG content. The maximum values of open-

circuit voltage (1.1 V) and fill factor (0.3) were also obtained at 10 wt% SPFG content. In addition, the annealing treatment at the appropriate temperature (160 °C for 10 min) greatly improved the device performance. However, annealing at excessive conditions, such as at 210 °C, resulted in a decrease of the device efficiency. P3OT/SPFG was also fabricated.<sup>144</sup> It had the similar performance as a P3HT/SPFG-based photovoltaic device.

### **1.3.4 Photocatalysts of Graphene–Semiconductor**

Very recently, Williams et al. reported that graphene oxide nanosheets of TiO<sub>2</sub>-graphene (or ZnO–graphene) suspensions in ethanol could be reduced in a UV-assisted photocatalytic process,<sup>54, 145</sup> which could occur because ethanol could scavenge the holes to produce ethoxy radicals, leading to the accumulation of the electrons in TiO<sub>2</sub> particles. The accumulated electrons can interact with the graphene oxide sheets to reduce the functional groups.

The photocatalytic methodology not only provides an on-demand UV-assisted reduction technique but also opens an effective way to obtain photoactive graphene-semiconductor composites. Very recently, Akhavan et al. found that graphene–TiO<sub>2</sub> exhibited a higher photocatalytic activity than TiO<sub>2</sub> alone for photoinactivation of bacteria under solar light irradiation.<sup>146</sup> The bare TiO<sub>2</sub> thin film showed weak antibacterial activity with a relative reduction rate of  $8.6 \times 10^{-3} \text{ min}^{-1}$  under solar light irradiation. However, after the photocatalytic reduction of the annealed graphene oxide-TiO<sub>2</sub> thin film under UV/Vis light irradiation for 0.5 h, the antibacterial activity was improved by 60 %. Furthermore, the improved reduction of the graphene oxide (i.e., the

better conductivity of the platelets) resulted in higher photocatalytic performance of the TiO<sub>2</sub> thin film. The photocatalytic reduction of the graphene oxide for 4 h improved the antibacterial activity of the graphene oxide/TiO<sub>2</sub> thin film by a factor of about six compared to that of the annealed graphene oxide/TiO<sub>2</sub> thin film. It is well known that the photocatalytic and bactericidal activities of TiO<sub>2</sub>-based materials can be enhanced by incorporating noble metal (nano) particles to decrease the optical band gap of TiO<sub>2</sub> and/or the recombination rate of the photoexcited pairs.<sup>147–151</sup> In the metal–semiconductor oxide composites, the photoexcited electrons accumulate on the incorporated metal and holes remain on the photocatalyst surface, leading to a reduction in recombination rate of the photoexcited pairs due to the improvement of charge separation between them. The reduced graphene oxide platelets on the surface of the TiO<sub>2</sub> thin film could play a similar role as the incorporated metallic particles in TiO<sub>2</sub>-based materials. The UV/Vis spectrophotometry showed that the optical band gap energy of the TiO<sub>2</sub> films was not significantly changed by incorporating the graphene (oxide) platelets. Therefore, the enhancement of the photocatalytic activity of the TiO<sub>2</sub> film under sunlight irradiation would be due to the action of the reduced graphene oxide platelets as electron acceptors to decrease the rate of recombination of the photoexcited pairs and thus to increase the quantum efficiency of the photocatalytic process.<sup>145</sup>

## 1.4 Graphene for Dye-sensitized Solar Cells

### 1.4.1 Transparent electrode

Graphene is an ideal two-dimensional material as a transparent electrode for solar cells due to its unique properties:<sup>30,152</sup> (1) the capability to be assembled into film electrode with ultra-smooth surface;<sup>81</sup> (2) the atomic thickness to exhibit very high transparency in both the visible and near-infrared regions<sup>99</sup> and (3) low cost to prepare graphene.<sup>76</sup>

Very recently, Wang et al. explored a graphene film as a window electrode for dye-sensitized solar cells (Fig.1.6).<sup>81</sup> The graphene film was prepared by using exfoliated graphite oxide as starting material, followed by film deposition and thermal reduction. The sheet resistance ( $R_s$ ) and the calculated average conductivity of a graphene film (ca. 10 nm thick) were 1.8 k $\Omega$ /sq and ca. 550 S/cm, respectively. When the film thickness was increased to 30 nm, the conductivity of graphene film increased to 727 S/cm and  $R_s$  decreased to 0.46 k $\Omega$ /sq. At a wavelength of 1000 nm, a ca. 10 nm thick film had a transmittance of 70.7%. Furthermore, its transmittance can be enhanced to over 80.0% by decreasing film thickness. In contrast to FTO and ITO that have strong absorptions in the infrared region of 0.75-3  $\mu$ m, the graphene films remain transparent in this region. Those unique properties of the graphene films constitute an outstanding window electrode material for optoelectronics applicable to a wide range of wavelengths. A dye-sensitized solid solar cell, which was based on spiro-OMeTAD1 (as a hole transport material) and porous TiO<sub>2</sub> (for electron transport) with the graphene film as transparent anode and Au as cathode (Fig.1.6 a and b), exhibited a short-circuit photocurrent density



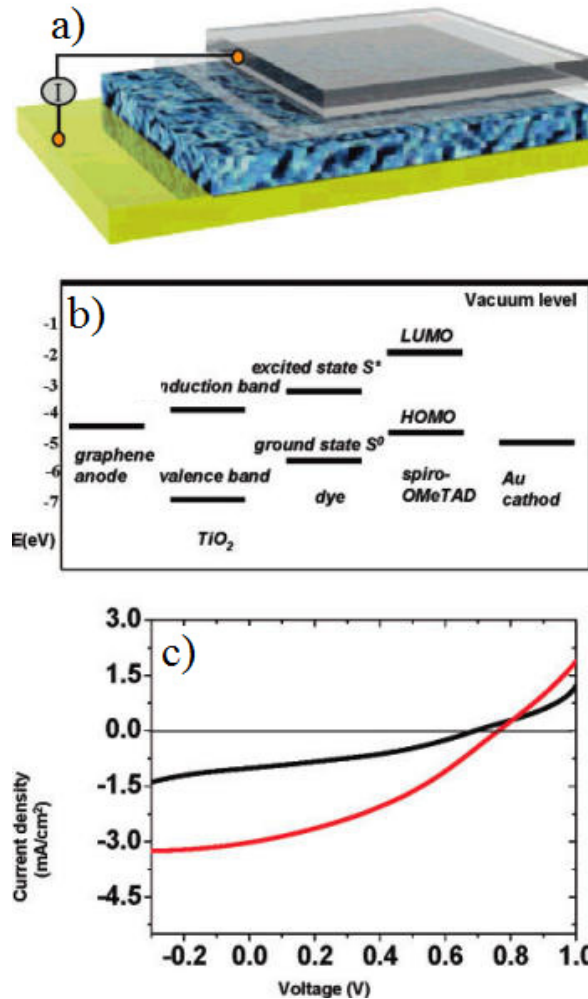


**Fig.1.6. Structure and performance of solar cell based on graphene electrodes.** (a) Structure of dye-sensitized solar cell using graphene film as electrode (the four layers from bottom to top are Au, dye-sensitized heterojunction, compact TiO<sub>2</sub>, and graphene film). (b) The energy level diagram of graphene/TiO<sub>2</sub>/ dye/spiro-OMeTAD/Au device. (c) I-V curve of graphene-based cell (black) and the FTO-based cell (red), illuminated under AM solar light (1 sun).<sup>81</sup> (See Appendix E for permission to republish this material.)

( $J_{sc}$ ) of 1.01 mA/cm<sup>2</sup> with an open-circuit voltage ( $V_{oc}$ ) of 0.7 V, calculated filling factor ( $FF$ ) of 0.36, and overall power conversion efficiency ( $PCE$ ) of 0.26% under illumination

of simulated solar light. When the graphene film electrode was replaced with FTO, the cell provided  $J_{sc}$  of 3.02 mA/cm<sup>2</sup>,  $V_{oc}$  of 0.76 V, FF of 0.36, and PCE of 0.84%. Therefore, one can see that the  $J_{sc}$  and  $PCE$  of the graphene film-based cell are still somewhat low. This happened because of the series resistance of the device, the relatively lower transmittance of the electrode, and the electronic interfacial change.

#### 1.4.2 Promoter in Photoelectrode for DSSCs

1D nanomaterials (such as carbon nanotubes), which have special charge transfer properties, were introduced into the electrodes of TiO<sub>2</sub>-based dye-sensitized solar cells (DSSCs).<sup>52,53</sup> However, the improvement in efficiency of DSSCs was limited by the point of contact between nanosphere TiO<sub>2</sub> and column-shaped 1D nanomaterials. In contrast, graphene, which is a 2D soft single-atomic layer, can have excellent contact with TiO<sub>2</sub> nanoparticles.<sup>54</sup> In other words, nanocrystalline TiO<sub>2</sub> can anchor on the graphene flake to form graphene bridges. The bridge graphene, which has excellent electrical conduction, can accelerate the electron transport from the conduction band (CB) of TiO<sub>2</sub> at the anchor position and thus reduce the recombination of charges,<sup>55</sup> leading to the enhancement of charge separation. Furthermore, graphene has a very high light transparency and can be assembled into film electrode with an ultra-smooth surface. These constitute an ideal 2D material as a transparent electrode for solar cells.

TiO<sub>2</sub> nanoparticles with average particle size 15–20 nm are typically deposited as a porous layer on a transparent conductive oxide (TCO) during the fabrication of a DSSC.<sup>153,154</sup> The rough surface of fluorine doped tin oxide (FTO) glass might short

circuit the cells.<sup>155</sup> When the thick TiO<sub>2</sub> layer is formed by the doctor blade method, the rough FTO surface may not be completely covered by the TiO<sub>2</sub> particles, leading to the formation of some voids between the TiO<sub>2</sub> nanoparticles and FTO glass interface.<sup>156</sup> As a result, some parts of the FTO surface, which are not covered by TiO<sub>2</sub>, can directly contact electrolytes, leading to a decrease of  $V_{oc}$  via the electron back-transport reaction [ $\frac{1}{2}\text{FTO} (2e^-) + \text{I}_3^- \rightarrow \text{FTO} + 3\text{I}^-$ ]. Furthermore, the transportation of photogenerated electrons across the TiO<sub>2</sub> nanoparticle network, which competes with the charge recombination, constitutes a major bottleneck for the development of DSSCs. To solve those issues, several groups incorporate graphene into TiO<sub>2</sub> nanostructure photoanode. Kim et al. employed graphene–TiO<sub>2</sub> as an interfacial layer between FTO layer and nanocrystalline TiO<sub>2</sub> (NC-TiO<sub>2</sub>) film.<sup>157</sup> They prepared graphene oxide (GO) by using Hummer’s method,<sup>74</sup> followed by mixing with TiO<sub>2</sub> colloidal suspension. The graphene oxide was reduced by UV radiation and then mixed with TiO<sub>2</sub> to form a graphene-TiO<sub>2</sub> solution, which was finally spin-coated over FTO glass substrate. The graphene-coated FTO was used as a transparent electrode for the DSSC with dye-sensitized nanocrystalline TiO<sub>2</sub> film as active material and Pt-coated FTO as a counter electrode. It was found that the influence of the graphene–TiO<sub>2</sub> interfacial layer on the performance of the DSSCs was evaluated. The introduction of graphene-TiO<sub>2</sub> interfacial layer into the DSSC increased the open-circuit voltage from 0.687 to 0.741 V and the photoconversion efficiency from 4.89 to 5.26%. Those improvements were attributed to the elimination of the direct contact between I<sub>3</sub><sup>-</sup> ions and FTO electrode, preventing the back-transport of electrons from the FTO electrode to the I<sub>3</sub><sup>-</sup> ions (Fig.1.7).<sup>157</sup> However, Yang et al.<sup>55</sup> and Sun et

al.<sup>158</sup> showed that the main promotion effect of graphene might be the enhancement of the charge transport rate, which can inhibit the charge recombination, because graphene has the excellent electrical conduction. Yang et al. incorporate 0.6 wt% graphene into TiO<sub>2</sub> nanostructure photoanode for a DSSC.<sup>147</sup> The graphene increased short-circuit current density from 11.25 to 16.29 mA/cm<sup>2</sup> (without sacrificing the open-circuit voltage) and the total conversion efficiency from 5.01 to 6.97%. Furthermore, the electrochemical impedance spectra (EIS) indicated that incorporating graphene into the TiO<sub>2</sub> nanocrystalline anode increased the electron transport rate to restrain the charge recombination. Therefore, Yang et al. proposed a mechanism about how the graphene can improve the efficiency of the DSSC as follows (Fig.1.8): The conduction band (CB) of semiconductor TiO<sub>2</sub> receives the electrons from photoexcited dye under illumination. Because the TiO<sub>2</sub> is anchored with 2D graphene that is homogeneous in the system, the excited electrons are captured by the graphene without any obstruction. The collected electrons can transport from TiO<sub>2</sub> to the conductive substrate quickly and effectively through graphene bridges, suppressing the adverse reactions (recombination and back reaction). Sun et al. also evaluated graphene-TiO<sub>2</sub> composite photoanodes for DSSCs.<sup>158</sup> They incorporated 0.5 wt% graphene in the TiO<sub>2</sub> photoanode by using the heterogeneous coagulation between Nafion-coated graphene and commercial TiO<sub>2</sub> nanoparticles, which ensured a tight interfacial binding between them. The DSSC based on the graphene-TiO<sub>2</sub> photoanode exhibited a power conversion efficiency of 4.28 %, which is higher than that (2.7%) without graphene. The enhanced efficiency was attributed to both the inhibition of charge recombination and the increase of dye adsorption. The charge recombination could be inhibited because Nafion-functionalized graphene was dispersed

homogeneously into the matrix of TiO<sub>2</sub> to form the effective and continuous 2D conductive network, in which electrons could obtain very long mean free paths and extend the electron lifetime. The introduction of graphene resulted in surface morphologies with more sites for the absorption of dye molecules, which harvests more light and leads to more photoinduced electrons injected from excited state of dye into conduction band of TiO<sub>2</sub>.

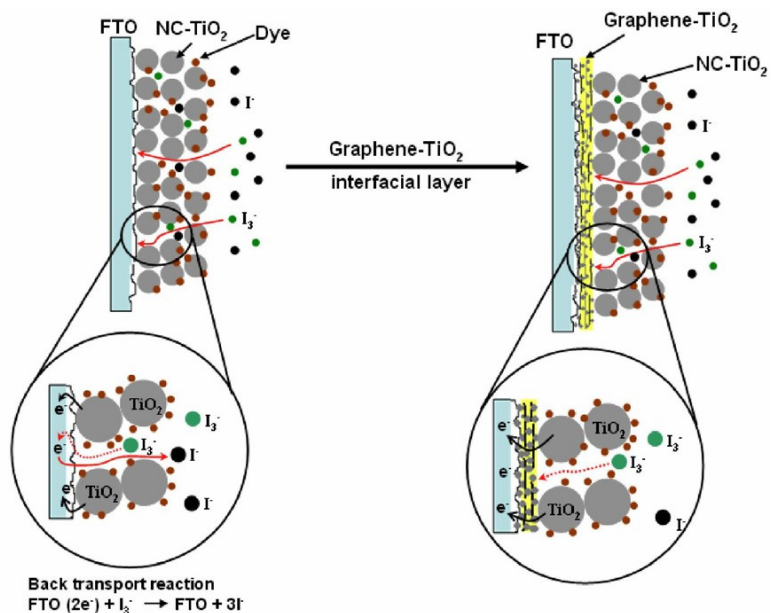


**Fig.1.7. Application of graphene-TiO<sub>2</sub> interfacial layer to prevent back-transport reaction of electrons.**<sup>157</sup> (See Appendix E for permission to republish this material.)

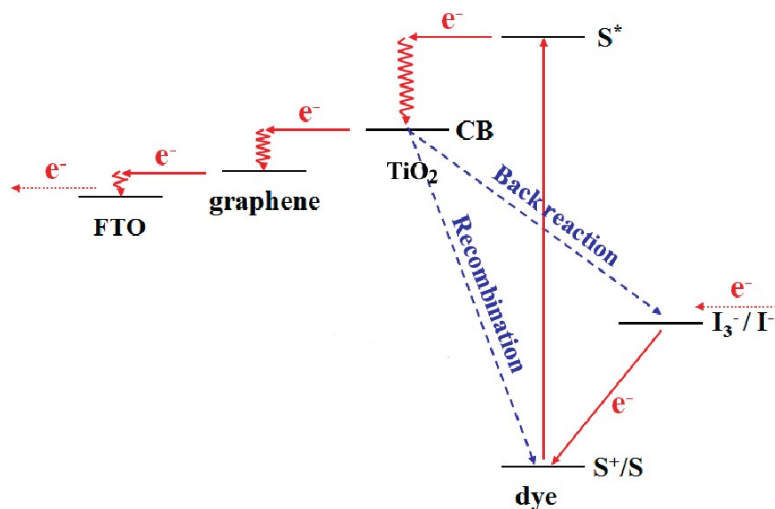


**Fig.1.8. Operational principle of the device:** the introduced 2D graphene bridges perform as an electron acceptor and transfer the electrons quickly. Hence, the recombination and back reaction are suppressed.<sup>147</sup> (See Appendix E for permission to republish this material.)

### 1.4.3 Counter Electrode for DSSCs

Dye-sensitized solar cells (DSSCs) have attracted considerable attention due to their low production cost and relatively high energy conversion efficiency. Counter electrode is an indispensable component in DSSCs, which catalyzes the reduction of I<sub>2</sub> to I<sup>-</sup> after electron injection.<sup>159</sup> Because the most commonly used Pt catalytic material is expensive, developing alternative materials with low cost is attracting much attention.

Recently, Shi and his co-workers prepared stable aqueous dispersions of graphene sheets through non-covalent functionalization with 1-pyrenebutyrate (PB).<sup>160</sup> The G-PB was spin-coated on a FTO substrate to form a graphene-modified FTO (G/FTO) as the counter electrode in DSSCs. For control experiments, bare FTO or platinum-coated FTO (Pt/FTO) was used as a counter electrode. All control experiments were performed under

the same conditions. The performances of the DSSCs were measured under simulated sun light (AM 1.5). The power conversion efficiencies were 0.048, 2.2, and 3.98% for FTO, G/FTO, and Pt/FTO DSSCs, respectively. This indicates that the performance of G/FTO DSSC is much better than that of the bare FTO DSSC, but poorer than that of the Pt/FTO DSSC. The relatively low efficiency of G/FTO DSSC is due to its relatively low conductivity ( $200\text{--}300\text{ Sm}^{-1}$ ).<sup>160</sup> It is well known that PEDOT:PSS has a higher conductivity and much better film-forming ability.<sup>161,162</sup> To take advantage of the PEDOT:PSS, Hong et al. fabricated the composite films of graphene and PEDOT:PSS as counter electrode for a DSSC by spin-coating the aqueous mixture of PB stabilized graphene and PEDOT:PSS on an ITO substrate at room temperature.<sup>163</sup> The power conversion efficiency of the DSSC reached 4.5% upon the excitation of AM 1.5 white light. The performance was comparable to that of the DSSC with Pt/ITO as a counter electrode (6.3%), and higher than that of the cell with PEDOT:PSS as a counter electrode (2.3%).

## Chapter 2 Goals and Hypotheses

Based on the background in Chapter 1, one can see that graphene, a two-dimensional carbon sheet, has attracted great interests due to its unique properties. To explore its practical applications, large-scale synthesis methods with controllable integration of individual graphene sheets to advanced multi-functional structures are essential. So far, numerous approaches have been developed for graphene synthesis, including mechanical cleavage, the epitaxial growth and chemical vapor deposition. All of those techniques are widely used to prepare flat graphene sheets on a substrate. Chemical oxidation and reduction of graphite is considered to be a very promising approach due to its low cost, easy preparation and high yield. It has been applied to prepare graphene oxide solutions, graphene-based composite materials and substrate-free graphene sheets. Besides, the development of novel graphene synthesis methods is also urgent.

Chemical oxidation and reduction of graphite method includes three steps: oxidation of graphite, exfoliation of graphite oxide into graphene oxide, and reduction of graphene oxide.<sup>71,72</sup> The oxidation of graphite produces hydrophilic graphite oxide, which can be easily exfoliated into graphene oxide in solvents, and further reduced to graphene by chemical, thermal reduction approaches. For graphite oxide, oxygen functional groups attach on both sides of the single layer and around the edges of the graphene structure. So far, however, no result has been reported about the relationship between the oxygen content and the structures of graphite oxides. This prompted us to investigate how the



oxygen content affects the functional groups, crystal structures, and surface areas of graphite oxides in Chapter 3.

Graphene oxide is a promising precursor for the chemical functionalization of graphene and the formation of graphene based composites.<sup>164-168</sup> For this reason, the investigation of graphene oxide is attracting much attention. Two reverse interactions exist between GO sheets: electrostatic repulsion and van der Waals attraction.<sup>169,170</sup> The electrostatic repulsion keeps the separation between GO sheets and thus stabilizes the solution, whereas the van der Waals attraction causes the aggregation of GO sheets and thus destabilizes the solution. Therefore, we hypothesized that the elimination or even reduction of GO charges in its solution should destabilize GO solution and cause the aggregation of GO sheets, leading to GO precipitation. This hypothesis could allow us to evaluate the stability of GO solution (Chapter 4). Furthermore, it was demonstrated that the HCl-induced GO precipitation is a feasible approach to deposit GO on a substrate as a Pt-free counter electrode for a dye-sensitized solar cell, which exhibited 1.65% power conversion efficiency.

To explore practical applications, large-scale synthesis with controllable integration of individual graphene sheets is essential. Especially, it is believed that developing 3D structures of graphene will further expand its significance in applications. We developed a novel strategy for the synthesis of graphene with 3D Honeycomb-like Structure via a simple reaction between  $\text{Li}_2\text{O}$  and  $\text{CO}$ . In this experiment, we designed  $\text{Li}_2\text{O}$  reacted with  $\text{CO}$  to form  $\text{Li}_2\text{CO}_3$  and graphene simultaneously. The formation of  $\text{Li}_2\text{CO}_3$  not only can isolate graphene sheets from each other to prevent graphite

formation during the process, but also play a role in determining the locally curved shape of graphene sheets. Honeycomb structured graphene could be obtained after removing  $\text{Li}_2\text{CO}_3$  by acid washing (Chapter 5).

For an efficient DSSC, the counter electrode (CE) is to reduce redox species in liquid solar cells, which are used as mediators in the regeneration of the sensitizer after electron injection. The ideal counter electrode material should possess the lowest possible sheet resistance, excellent catalytic activity for the reduction of the redox electrolyte, high chemical stability and a low cost. Platinum-loaded conducting glass has been widely employed as the standard CE for DSSCs due to its high catalytic activity and excellent conductivity as well as its high corrosion stability against iodine in the electrolyte.<sup>171–173</sup> However, the combination between the limited resource of platinum and the large application of platinum-based catalysts in the vehicle industry makes platinum extremely expensive and in diminishing supply. Therefore, it is important to explore Pt-free materials to replace the Pt counter electrode for DSSCs.<sup>174</sup> Due to the excellent conductivity and catalytic ability of honeycomb structured graphene, we hypothesized that it could be an effective counter electrode in DSSCs. This hypothesis was proved and the results were discussed in Chapter 6.

## Chapter 3 Effect of Oxygen Content on Structures of Graphite

### Oxides\*

#### 3.1 Introduction

Since experimentally demonstrated the existence of isolated graphene sheets in 2004, the synthesis methods of graphene attract people much attention. Novoselov et al. fabricated single- and few-layer graphene junctions on oxidized Si substrates by mechanical exfoliation of highly oriented pyrolytic graphite (HOPG).<sup>30</sup> Although this method is easy to apply at a low cost, it suffers the drawback of a low yield.<sup>86</sup> The epitaxial growth of graphene can be carried out by heating a SiC substrate in an ultrahigh vacuum at a high temperature (typically greater than 1000 °C).<sup>52,53</sup> This process can provide a higher yield with much fewer defects than the exfoliation method, but it cannot easily fabricate a large-area graphene sheet. The chemical vapor deposition (CVD)<sup>61-63,175</sup> method can be used to form a graphene monolayer on the surface of a metal catalyst via the catalytic decomposition of hydrocarbon or carbon monoxide. However, complicated pretreatment of metal substrates and a subsequent crucial chemical etching process limit its applications.<sup>108</sup>

---

\* The material contained in this chapter was previously published in *Industrial & Engineering Chemistry Research* 2011, 50(10), 6132-6137 by Hui Wang and Yun Hang Hu. See Appendix I for documentation of permission to republish this material.

The oxidation-reduction of graphite is considered a promising route to achieving mass production of graphene via three steps: oxidation of graphite, exfoliation of graphite oxide into graphene oxide, and reduction of graphene oxide.<sup>71,176</sup> The oxidation of graphite produces hydrophilic graphite oxide, which can be easily exfoliated into graphene oxide in solvents.

The history of graphite oxide can date back to almost 200 years ago. As early as 1859, Brodie first explored the oxidation of graphite by introducing potassium chlorate (KClO<sub>3</sub>) into a slurry of graphite in fuming nitric acid (HNO<sub>3</sub>).<sup>73</sup> This approach produced graphite oxide with an O/C ratio of 0.46. To increase the acidity of the reactants, Staudenmaier modified the method via replacing nitric acid with a mixture of sulfuric acid and nitric acid.<sup>177</sup> Furthermore, Hummers and his coworker developed a less hazardous oxidation process by reacting graphite with a mixture of potassium permanganate (KMnO<sub>4</sub>) and concentrated sulfuric acid (H<sub>2</sub>SO<sub>4</sub>), achieving a similar level of oxidation (O/C  $\approx$  0.5).<sup>74</sup> Although other slightly modified processes have been developed, those three methods are the primary routes for the synthesis of graphite oxide. Because graphite oxide is considered to be an important precursor to prepare graphene oxide and graphene, the investigation of graphite oxide is necessary.

The oxidation process breaks the  $\pi$ - $\pi$  conjugation in the original graphite structure to form graphite oxide. Lerf and co-workers<sup>178,179</sup> proposed the most popular structural model to describe the chemical structure of graphite oxide, namely, the single layer of graphite oxide is viewed as oxygen functional groups on both sides of the single layer and around the edges of the graphene structure. NMR measurements prove that this

model can best describe the structure of graphite oxide.<sup>180</sup> So far, however, no result has been reported about the relationship between the oxygen content and the structures of graphite oxides. This prompted us to investigate how the oxygen content affects the functional groups, crystal structures, and surface areas of graphite oxides in this work.

## **3.2 Experimental**

### **3.2.1 Sample preparation**

Graphite oxide was prepared from graphite powders (Sigma-Aldrich) via the modified Hummers method,<sup>71,181</sup> described as follows: potassium permanganate (3 g) was slowly added into the mixture of graphite (0.5 g), sodiumnitrate (0.5 g), and sulfuric acid (25 mL) at room temperature, followed by heating to 35 °C with a water-bath and then stirring at 35 °C for a selected oxidation time (10 min, 30min, 1 h, 1.5 h, 2 h, or 5 h) to form a thick paste. Deionized water (40 mL) was added into the thick paste with stirring, followed by heating to 90 °C over 30 min, then adding more deionized water (100 mL), and finally gradually adding 3 mL of H<sub>2</sub>O<sub>2</sub> (30%). The obtained sample was filtered and washed with 100 mL of deionized water. The filter sediment was dispersed in deionized water again, followed by ultrasonic treatment for 5 min and then centrifugal treatment to separate the solid from the water. The obtained solid sample of graphite oxide was dried in a vacuum furnace at 50 °C.

### 3.2.2 Characterization

**X-Ray Diffraction (XRD):** Crystal structures of graphite and graphite oxides were determined by using a Scintag XDS 2000 powder diffractometer with Cu K $\alpha$  ( $\lambda = 1.5406 \text{ \AA}$ ) radiation at a scan speed of  $1^\circ/\text{min}$  and a step size of  $0.03^\circ$  in the range of  $5^\circ \leq 2\theta \leq 70^\circ$ .



**Fig.3.1. Scintag XDS2000 Powder Diffractometer.**

**Thermal Gravimetric Analysis (TGA):** TGA was carried out for graphite oxide powders in a nitrogen atmosphere (100 mL/min) at a constant rate of 10 °C/min, using SDT Q600 equipment.

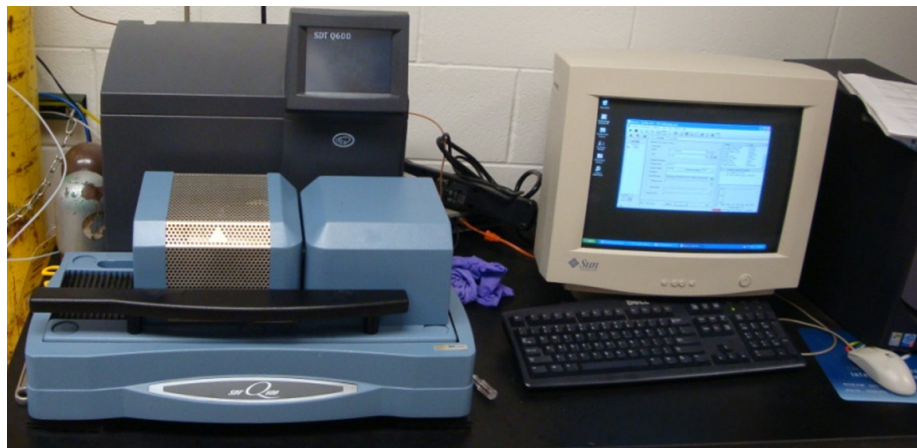


**Fig.3.2. SDT Q600 Thermogravimetric Analyzer.**

**Raman Spectroscopy:** Raman spectra of graphite oxides were obtained by using an Olympus BX41 spectrometer with a helium-neon laser to excite the samples.

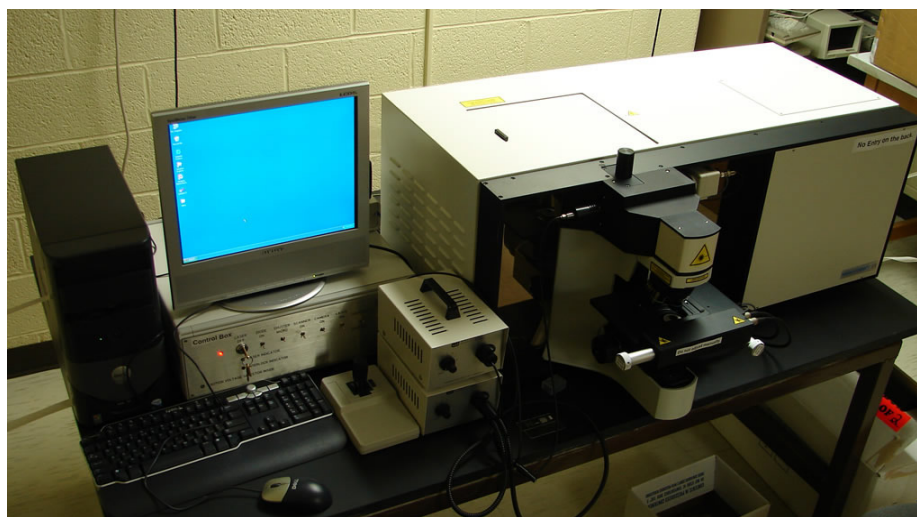


**Fig.3.3. Jobin-Yvon LabRAM HR800 Raman Spectrometer.**

**BET Surface Area Measurements:** Nitrogen adsorption at liquid nitrogen temperature (77 K) was used to measure surface areas of pristine graphite and graphite oxide with a Micromeritics ASAP 2000 sorptometer. Before the adsorption measurement, samples were degassed at 105 °C to remove water, and the surface area values were calculated by the BET model.<sup>182</sup>



**Fig.3.4. Micromeritics ASAP 2000 Sorptometer.**



**Fourier Transform Infrared Spectroscopy (FTIR):** FTIR measurements for graphite oxides were carried out by using an FT/IR-4200 spectrometer (Perkin-Elmer Spectrum).

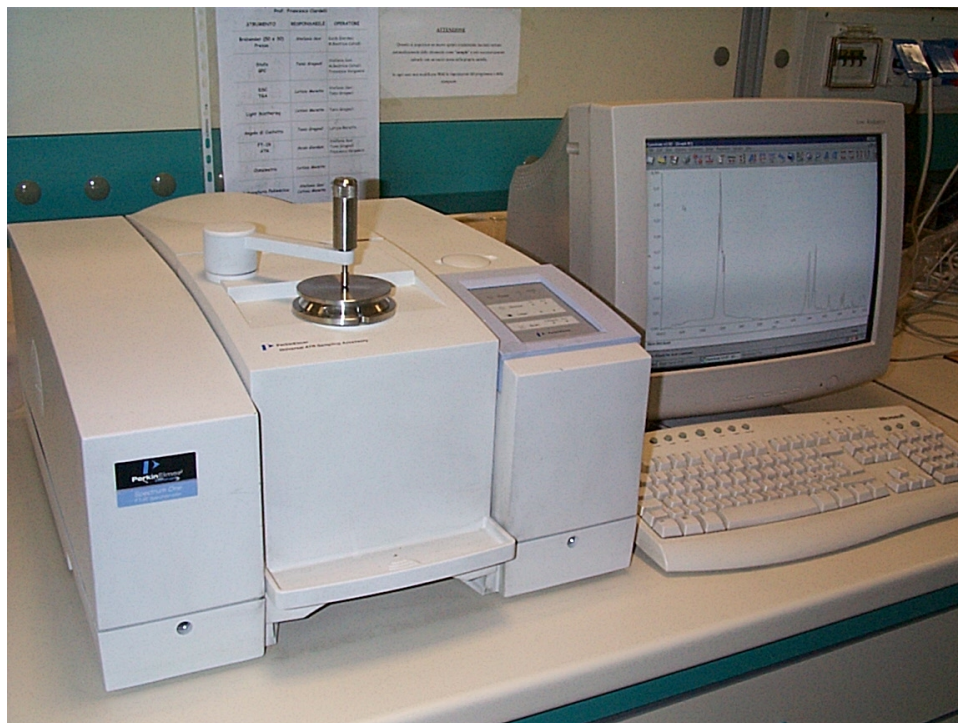


**Fig.3.5. Fourier Transformed Infrared (FTIR) Spectrometer.**

**Temperature-Programmed Decomposition-Mass Spectrum (TPD-MS):** TPD-MS analysis was carried out for graphite oxides from 25 to 625 °C at a rate of 10 °C per min, and the gas products were continuously analyzed with an online Hewlett-Packard 5970 series mass selective detector.



**Fig.3.6. Hewlett-Packard 5970 Series Mass Selective Detector.**

**Field Emission Scanning Electron Microscopy (SEM):** Graphite and graphite oxides were imaged with a Hitachi S-4700 FE-SEM, using an accelerating voltage of 1.5 kV at a working distance of 1.5-1.6 mm.

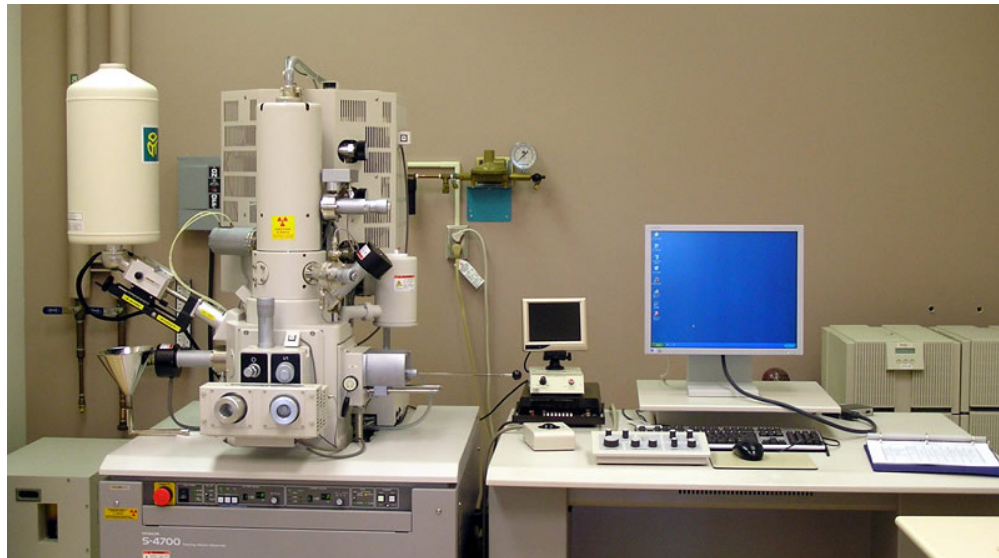


**Fig.3.7. Hitachi S-4700 FE-SEM.**

**Transmission Electron Microscopy (TEM):** The morphology of graphite oxide was also analyzed with a JEM-4000FX TEM at a 200 kV voltage.



**Fig.3.8. JEOL JEM-4000FX TEM.**

### 3.3 Results and Discussion

Changing the reaction time for the oxidation of graphite was employed to tune the oxygen content of graphite oxide. The obtained graphite oxide samples were first subjected to FTIR measurements. As shown in Fig.3.9, one can see the following absorption bands: a broad and intense band at 3400-3600  $\text{cm}^{-1}$  that can be assigned to O-H stretching vibrations, a band at 1760  $\text{cm}^{-1}$  due to the C=O stretching vibration, and the bands at 1450  $\text{cm}^{-1}$  and 1230  $\text{cm}^{-1}$  corresponding to stretching vibrations of the C-O bond and epoxy C-O-C bond, respectively.<sup>160, 183-185</sup> Furthermore, there is an additional band located at 1630  $\text{cm}^{-1}$ , which can be attributed to the unoxidized graphitic domain.<sup>186</sup> Those indicate that the functional groups of graphite oxides are carboxyl, epoxy, and hydroxyl groups.<sup>164</sup> When the oxidation time of graphite increased from 10 min to 5 h, the positions of FTIR bands remained unchanged, indicating that the types of functional groups are independent of oxidation time.

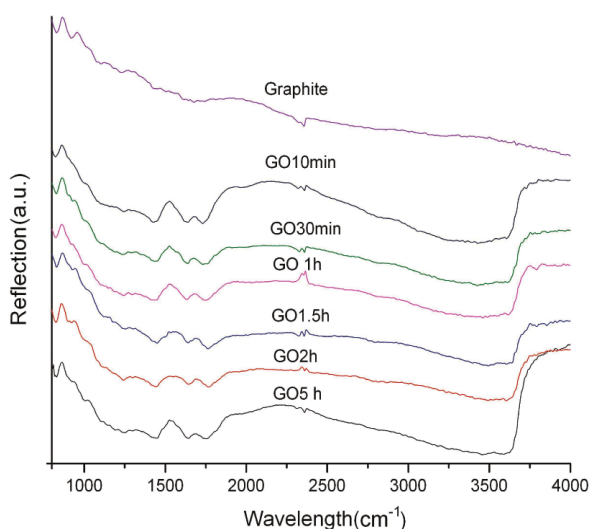


**Fig.3.9. FTIR spectra of graphite oxides prepared with various oxidation times.**

However, as shown by TGA curves (Fig.3.10), the total number of functional groups is dependent on the oxidation time. Fig.3.10 shows that all curves can be divided into three regions: below 100 °C, 100-240 °C, and 240-600 °C. Furthermore, one can see that the most functional groups were removed at temperatures below 240 °C, which is consistent with previous reports.<sup>76,78,84,187</sup> In addition, the total weight losses were 46, 56, 69, and 74% for the samples prepared with oxidation times of 10 min, 30 min, 1 h, and 1.5 h, respectively. This indicates that the total amount of functional groups increases with increasing the oxidation time of graphite from 10 min to 1.5 h. However, graphite oxides prepared with oxidation times longer than 1.5 h have the same weight loss as that with 1.5 h, indicating that the oxidation of graphite reached its saturation in 1.5 h.

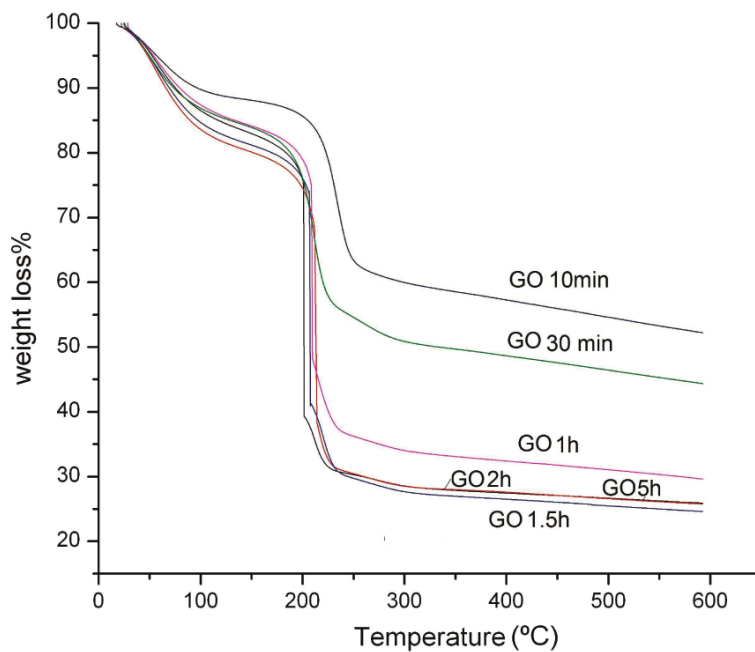


**Fig.3.10. TGA curves of graphite oxides prepared with various oxidation times.**

We further employed TPD-MS to evaluate the thermal decomposition of graphite oxides. As shown in Fig.3.11, one can observe the intense evolution of CO and CO<sub>2</sub> in the temperature range of 180-250 °C, corresponding to a large weight loss in the TGA curves. Two H<sub>2</sub>O peaks occurred: one at 100 °C and another at temperatures above 200 °C. The former one can be attributed to the desorption of adsorbed water, whereas the later one should be associated with decomposition of the functional groups. However, besides those products, a small amount of HC(OH)<sub>3</sub> can also be observed between 200 and 300 °C in our TPD-MS spectrum (Fig.3.11). Furthermore, the ratios of oxygen to carbon (O/C ratios) were calculated from the above TGA and TPD-MS measurements with a small relative error less than 0.1%. Fig.3.12 shows that the oxygen content increased to 0.47 with increasing the oxidation time from 10 to 90 min and then remained unchanged. This indicates that the oxygen content reaches a saturated level (O/C = 0.47) in 90 min.

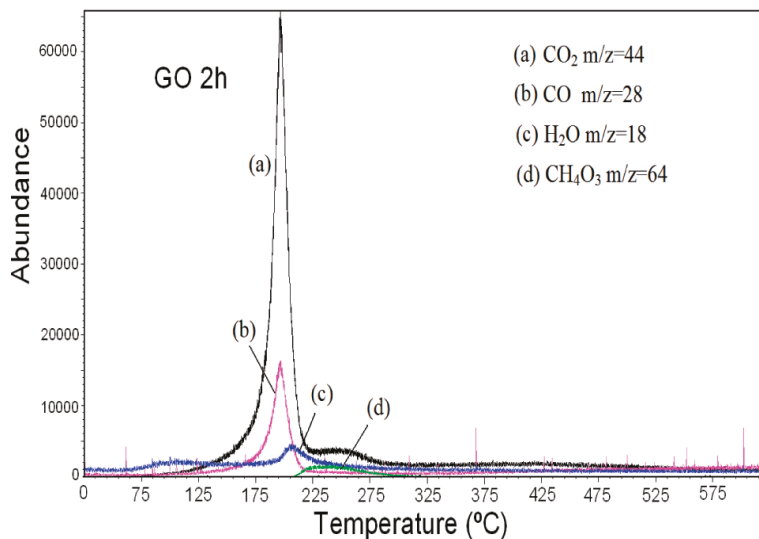


**Fig.3.11. TPD-MS spectrum of graphite oxide (2 h).**

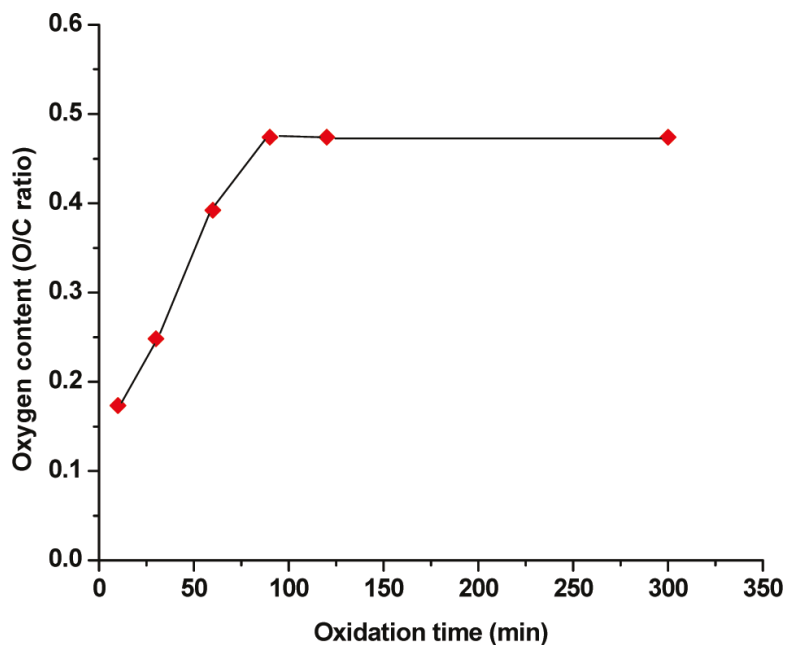


**Fig.3.12. Variation of the oxygen content of graphite oxide with the oxidation time of preparation.**

The crystalline structures of pristine graphite and graphite oxides were evaluated by XRD. As shown in Fig.3.13, one can see that pristine graphite exhibits a high crystalline degree with a strong and sharp diffraction peak at  $2\theta = 26.6^\circ$ , which corresponds to the diffraction of the (002) plane with an interplanar distance of  $3.36 \text{ \AA}$ . In contrast, the crystalline degrees of graphite oxides are very low with a small broad-diffraction peak, which can be attributed to a preserved graphene-like honeycomb lattice in graphite oxides.<sup>166,188</sup> This means that the oxidation of graphite led to the shift of the diffraction peak position from  $26.6^\circ$  to  $12.1\text{-}11.2^\circ$ , corresponding to the increase in the interplanar distance from  $3.36 \text{ \AA}$  to  $7.31\text{-}7.91 \text{ \AA}$ . This happened because oxygen functional groups were attached to both sides of the single graphene layer during its oxidation.<sup>179, 189-191</sup>

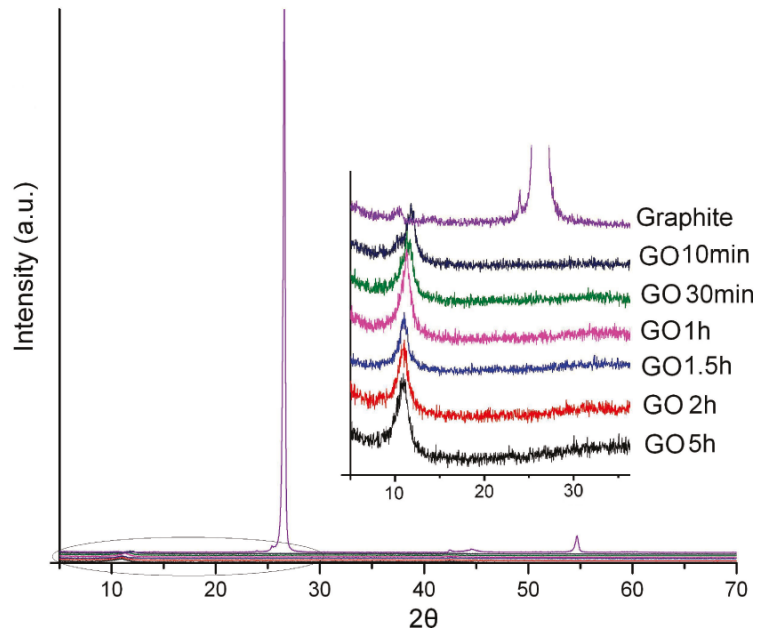


**Fig.3.13. XRD patterns of graphite oxides prepared with various oxidation times.**

The disrupted layer structures of graphite oxides were further supported by FE-SEM images (Fig.3.14 a and b). Graphite shows its flat surface with many small and dispersed flakes and an ordered layer structure. In contrast, graphite oxide exhibits randomly crumpled layer structures, indicating that the ordered layer structure in pristine graphite has been disrupted due to its oxidation. In addition, the exfoliation of graphite oxide can be clearly observed from TEM image (Fig.3.14 c).



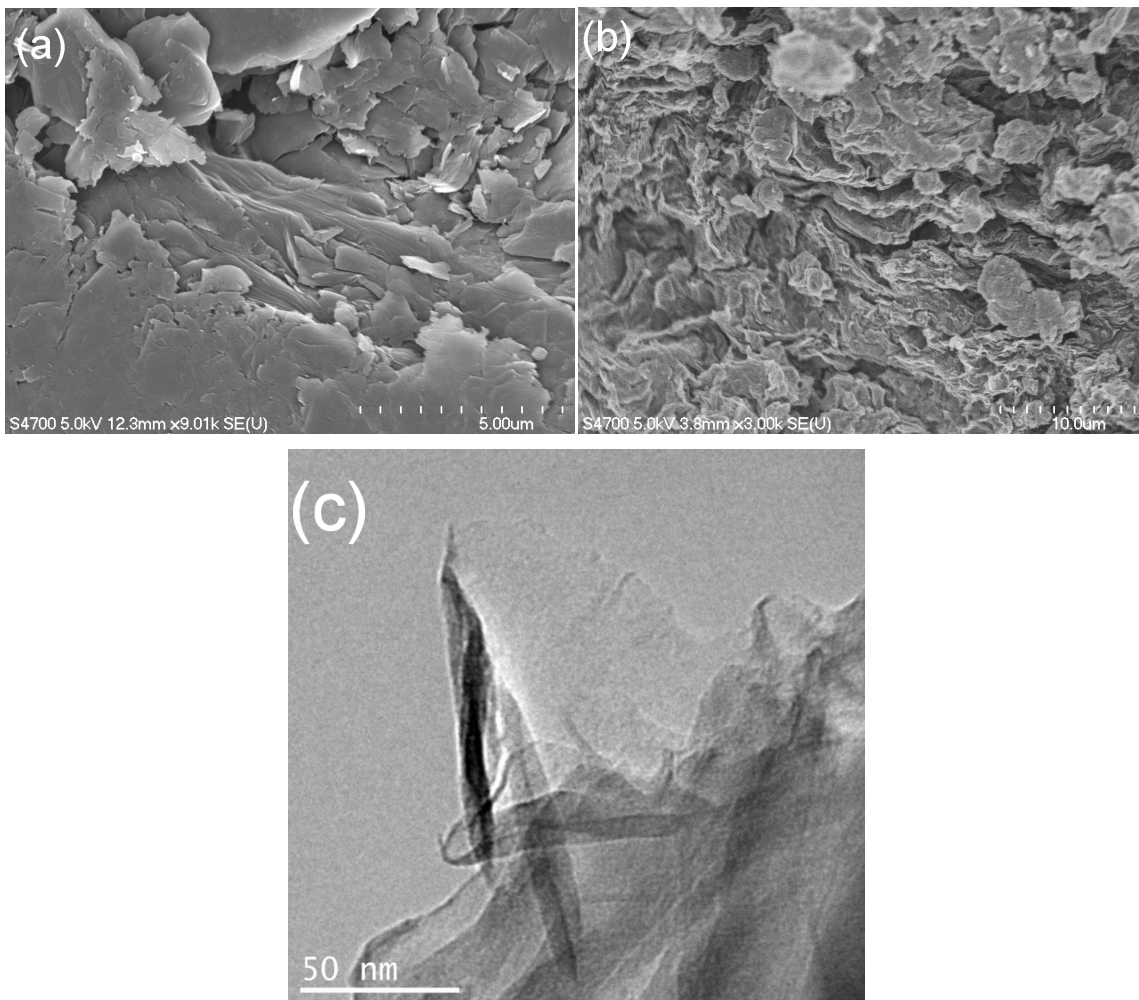


**Fig.3.14. FE-SEM images of graphite (a) and graphite oxidized for 2 h (b) and TEM image of graphite oxide for 2 h (c).**

Furthermore, we correlated interplanar distances of graphite oxides with their O/C ratios, generating a linear relationship (Fig.3.15), which can be expressed by the following linear equation:

$$d = 1.6959C_o + 6.9787 \quad (1)$$

where  $d$  and  $C_0$  are interplanar distance ( $\text{\AA}$ ) and O/C ratio, respectively. This indicates that the expansion is linearly proportional to the oxygen content of graphite oxide. Furthermore, this equation can allow one to predict the interplanar distance from its O/C ratio.

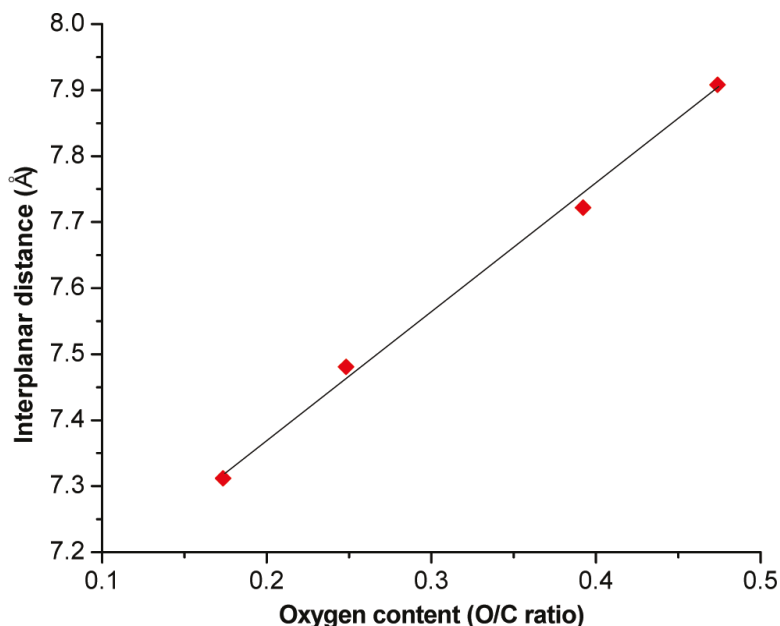


**Fig.3.15. Relationship between the interplanar distance and oxygen content of graphite oxides.**

The effect of oxygen content on surface areas of graphite oxides was also evaluated by nitrogen adsorption. If all carbon atoms are considered surface atoms, the theoretic surface area of graphite should be  $2630 \text{ m}^2/\text{g}$ .<sup>192</sup> However, most atoms in graphite are not surface ones, because the interplanar space is too small to allow gas molecules to enter into the space. Indeed, as shown in Fig.3.16, one can see that the pristine graphite has a very low BET surface area of  $6 \text{ m}^2/\text{g}$ . In contrast, graphite oxides have much larger BET surface areas than pristine graphite, because oxygen groups

expanded the interplanar space, which is large enough for nitrogen molecules to enter inside for N<sub>2</sub> adsorption. Furthermore, the surface areas linearly increased to 295 m<sup>2</sup>/g with increasing O/C ratios as follows:

$$S = 586.64C_o + 6 \quad (2)$$

where S and C<sub>o</sub> are the BET surface area and O/C ratio of graphite oxides, respectively. Therefore, one can exploit the equation to estimate the surface area of a graphite oxide from its oxygen content.

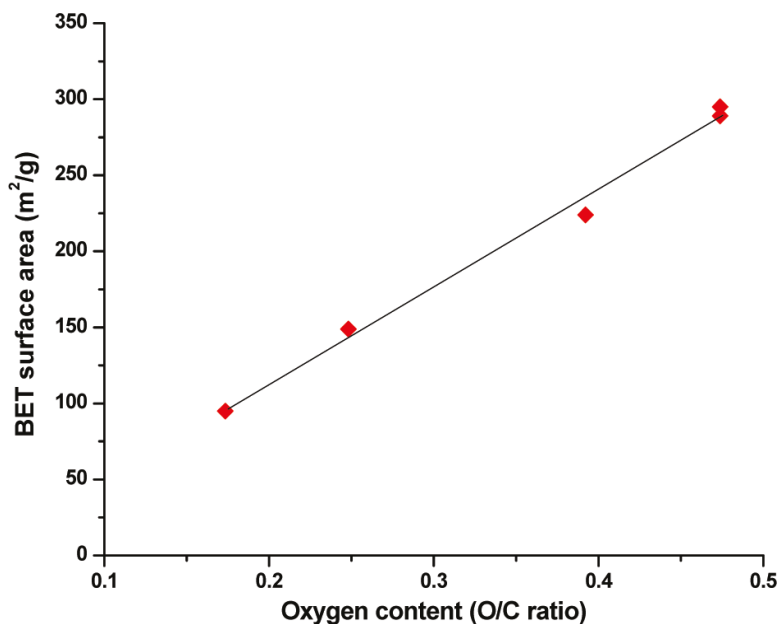


**Fig.3.16. Relationship between BET surface areas of graphite oxides and their oxygen contents.**

Raman spectroscopy is an effective tool for the characterization of carbon materials, which have two characteristic absorption bands, the G band and D band at around 1580 and 1350 cm<sup>-1</sup>, respectively. The G band is associated with bond stretching of the sp<sup>2</sup> carbon pairs in both rings and chains, while the D band is due to the breathing

mode of aromatic rings with dangling bonds in plane terminations.<sup>193-195</sup> Furthermore, the intensity ratio of the D band to the G band is usually employed to determine the disorder degree of structure for carbon materials.<sup>196</sup> As shown in Fig.3.17, one can observe a weak and broad D band with a sharp and strong G peak for pristine graphite, indicating a stacked layer structure. After oxidation, the D-band intensity increased and became comparable to that of the G band. The increase of the D band was due to the presence of functional groups on the planar carbon backbones.<sup>78,189</sup> The D/G intensity ratio of graphite oxide is 6 times larger than that of pristine graphite, which is consistent with other reports.<sup>78,109,186</sup> However, as shown in Fig.3.18, the intensity ratio of D/G did not increase with an increasing O/C ratio. This indicates that the stacked layer structure of graphite can be easily disordered even by partial oxidation.

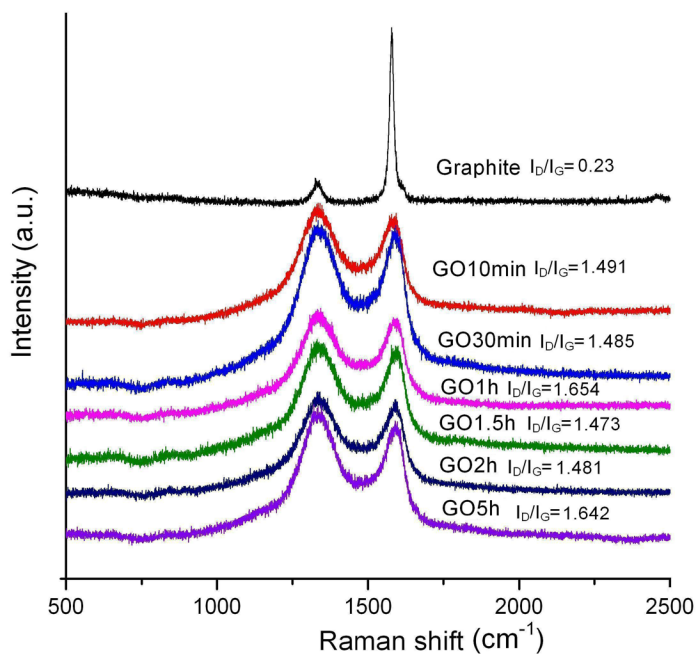


**Fig.3.17. Raman spectra of pristine graphite and graphite oxides prepared with various oxidation times (as marked in the figure).**

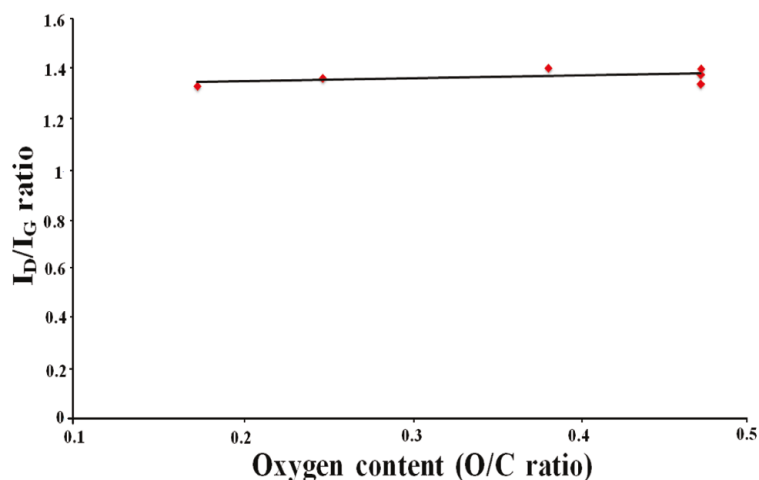


**Fig.3.18.** The relationship between intensity ratios of Raman D to G bands of graphite oxides and their oxygen contents.

### 3.4 Conclusion

The oxygen content of graphite oxide can be tuned by changing the oxidation time via a modified Hummers approach. There are three types of functional groups in graphite oxides (epoxy, carboxyl, and hydroxyl groups), which are independent of the oxidation time. However, the content of oxygen-containing functional groups increased with increasing the oxidation time and reached a saturated level ( $O/C = 0.47$ ) in 1.5 h. Furthermore, the interplanar spaces and BET surface areas of graphite oxides linearly increased with increasing oxygen content. However, the ratio of the D band to the G band in Raman spectroscopy, which is associated with the disorder of the carbon backbone, remained unchanged with increasing oxygen content.

## Chapter 4 Electrolyte-induced Precipitation of Graphene

### Oxide in Its Aqueous Solution\*

#### 4.1 Introduction

Graphene oxide (GO) is a promising precursor to synthesize graphene sheets at high yield with low cost.<sup>197-200</sup> Unlike hydrophobic graphene, GO is hydrophilic and able to form a solution with water. The aqueous solution of GO is promising for many applications, such as GO films and graphene films,<sup>77,201,202</sup> which are ideal candidates as sensors,<sup>203,204</sup> field effect transistors,<sup>205</sup> and transparent electrodes.<sup>81</sup> The GO solution can also be exploited to prepare high-quality graphene-based composites.<sup>206-209</sup> Furthermore, the GO solution was successfully employed to fabricate free-standing graphene and GO papers.<sup>47,160,210</sup> For this reason, the investigation of graphite oxide and graphene oxide is attracting much attention.

Graphene oxide (GO) possesses a unique 2D structure—two abruptly different length scales: atomic thickness and the lateral dimension of up to tens of micrometers. Due to this special structure, the stability of aqueous GO solution might be different with other typical solutions.

---

\*The material contained in this chapter was previously published in *Journal of Colloid and Interface Science*, 2013, 391, 21-27 by Hui Wang and Yun Hang Hu. See Appendix J for documentation of permission to republish this material.

It was known that there are two reverse interactions between GO sheets: electrostatic repulsion and van der Waals attraction,<sup>169,170</sup> namely, GO solution exhibits Derjaguin–Landau–Verwey–Overbeek (DLVO) type behavior.<sup>214</sup> While the electrostatic repulsion keeps the separation between GO sheets and thus stabilizes the solution, the van der Waals attraction causes the aggregation of GO sheets and thus destabilizes the solution. Therefore, the elimination or even reduction of GO charges in its solution should destabilize GO solution and cause the aggregation of GO sheets, leading to GO precipitation. This hypothesis could allow us to evaluate the stability of GO solution. In this work, to test this hypothesis, we introduced strong electrolytes (acid, base, and salt) into GO solution to examine the effect of charges on the stability of GO solution.

## **4.2 Experimental**

### **4.2.1 Sample preparation**

Graphite oxide was prepared from graphite powders (Sigma–Aldrich) via the modified Hummers method,<sup>74</sup> which was described in section 3.2. In this case, graphite was treated for 5 h to achieve full oxidation. The oxidation product was re-dissolved in de-ionized water (DW), followed by ultrasonic treatment (for 24 h) to achieve full exfoliation from graphite oxide to graphene oxide (GO). After deposition and stabilization for 72 h, the upper supernatant was separated carefully from the bottom sediment to obtain the yellow–brown transparent GO solution. Furthermore, the solution was further subjected to a high-speed centrifugation at 3600 rpm to remove some GO pieces, generating the final stable GO solution, with a concentration of about 0.5 mg/ml.

To evaluate the effect of a strong electrolyte on the stabilization of GO solution, 2.5 ml of GO solution was added into the vials containing 0.5 ml aqueous solutions of HCl, LiCl, and LiOH (2.4 M concentration), respectively. The concentration of HCl (LiCl or LiOH) in the obtained solution is 0.4 M. Those three vials were shaken by a hand for 20 s to obtain homogeneous liquid and then remained immobile for the observation of color change and the precipitation of the GO with time. The precipitation process was monitored by digital camera. The same procedure was also employed to evaluate: (a) the concentration effect of HCl (LiCl or LiOH) on GO precipitation, and (b) the effect of other salts (LiBr, KCl, and KBr) on GO precipitation.

#### **4.2.2 Fabrication of DSSCs**

FTO (fluorine doped tin oxide) glass plates were immersed in 40 mM  $\text{TiCl}_4$  solution at 70 °C for 30 min and then coated by  $\text{TiO}_2$  film by a doctor blade printing method as a photoelectrode. The photoelectrode was heated at 325, 375, 450, and 500 °C for 5, 5, 15, and 15 min, respectively. After that, the  $\text{TiO}_2$  photoelectrode was treated again with  $\text{TiCl}_4$  at 70 °C for 30 min and sintered at 500 °C for 30 min. Dye sensitization was carried out by immersing  $\text{TiO}_2$  photoelectrodes in an ethanol solution of 0.3 mM N719 dye. Counter electrodes were prepared by depositing GO sheets via the precipitation (induced by HCl, LiCl, or LiOH) on a FTO glass plate, followed by heating at 400 °C for 20 min.

The dye absorbed  $\text{TiO}_2$  electrode and the GO aggregation-based counter electrode were assembled into a sandwich-type cell with electrolyte between electrodes. The electrolyte consists of 0.025 M LiI, 0.04 M  $\text{I}_2$ , 0.28 M tert-butyl pyridine (TBP), 0.6 M 1-



butyl-3-methylimidazolium iodide (BMII), and 0.05 M guanidinium thiocyanate in acetonitrile/valeronitrile with 85/15 volume ratio. Photocurrent–voltage (I–V) measurements were performed using a Keithley model 2400 measurement unit. The light source (AM 1.5 solar illumination, 100 mW/cm<sup>2</sup>) was generated by a Newport solar simulator equipped with 1.5 G Air mass filter.

#### **4.2.3 Characterization**

**Transmission Electron Microscopy (TEM):** The morphologies of GO and the GO aggregations by HCl, LiCl, and LiOH were observed using a JEM-4000FX TEM at a 200 kV voltage.

**Raman Spectroscopy:** Raman spectra of GO and its aggregations were obtained using an Olympus BX41 spectrometer.

**Fourier Transform Infrared Spectroscopy (FTIR):** The functional groups of GO and its aggregations were evaluated by FT/IR-4200 spectrometer. (Perkin-Elmer Spectrum One).

**Ultraviolet-visible spectroscopy:** The UV–visible absorption of GO solution, top supernatants after the precipitation, and GO precipitates were carried out by UV–Vis spectrophotometer (UV 2450 Shimadzu).



**Fig.4.1. Shimadzu UV-2450 Spectrometer.**

**Photocurrent–voltage (I–V) measurements:** I–V curves were performed using a Keithley Model 2400 measurement unit. The light source (AM 1.5 solar illumination,  $100 \text{ mW/cm}^2$ ) was generated by a Newport solar simulator equipped with a 1.5G air mass filter.



**Fig.4.2. Newport Sunlight Simulator and Keithley 2400 Multi-meter.**

## **4.3 Results and discussion**

### **4.3.1. Electrolyte-induced GO precipitation**

As shown in Fig.4.3, one can see that the precipitation of yellow GO in HCl-GO and LiCl-GO solutions began after 2 h. Furthermore, the precipitation finished in 72 h. As a result, the initially transparent yellow-brown GO solution separated to two parts: a colorless top supernatant and a brown precipitate at bottom. Those observations demonstrate that HCl and LiCl electrolytes destabilized the GO solution, leading to the aggregation of GO sheets. Furthermore, the mixing of LiOH and GO solutions immediately caused a color change of GO solution from yellow-brown to dark-brown (Fig.4.3a). The precipitation of GO started after 10 min, which is much shorter than that (2 h) in HCl-GO and LiCl-GO solutions. The color of final GO precipitate at bottom was black in LiOH-GO solution.

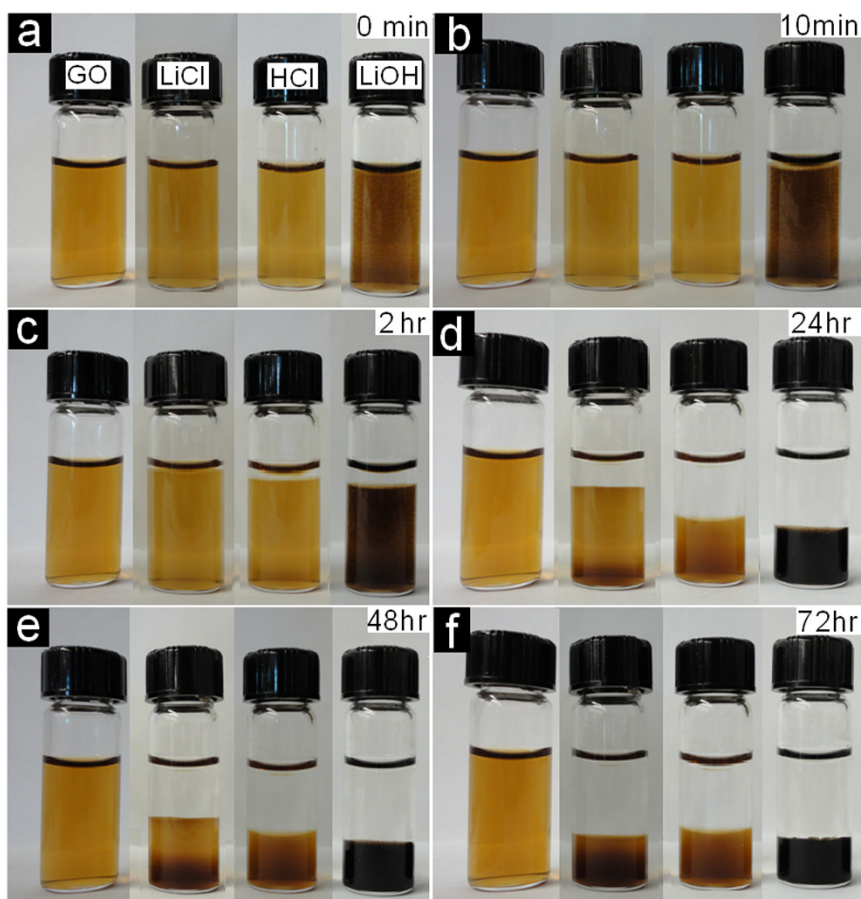


**Fig.4.3. Precipitation in aqueous solutions of GO, 0.4 M LiCl–GO, 0.4 M HCl–GO, and 0.4 M LiOH–GO (from left to right) after (a) 0 min, (b) 10 min, (c) 2 h, (d) 24 h, (e) 48 h, and (f) 72 h.**

To examine the effect of electrolyte concentration on the stability of the GO solution, the GO precipitation of 0.1, 0.2, 0.6, and 0.8 M HCl (LiOH, or LiCl)–GO solutions were also evaluated. The same precipitation was observed for those HCl- and LiCl-added solutions as for 0.4 M HCl (LiCl)-added GO solutions (Fig.4.4 and Fig.4.5). However, when the GO solution was combined with a low concentration of LiOH (0.1 M), homogeneous black suspension was obtained instead of GO precipitation (Fig.4.6). This indicates that the precipitation of GO in a LiOH–GO solution is dependent on the

concentration of LiOH. In addition, the precipitation of GO from its aqueous solution could also be caused by adding KCl, KBr, or LiBr (Fig.4.6), suggesting a common salt effect on the destabilization of the GO solution.

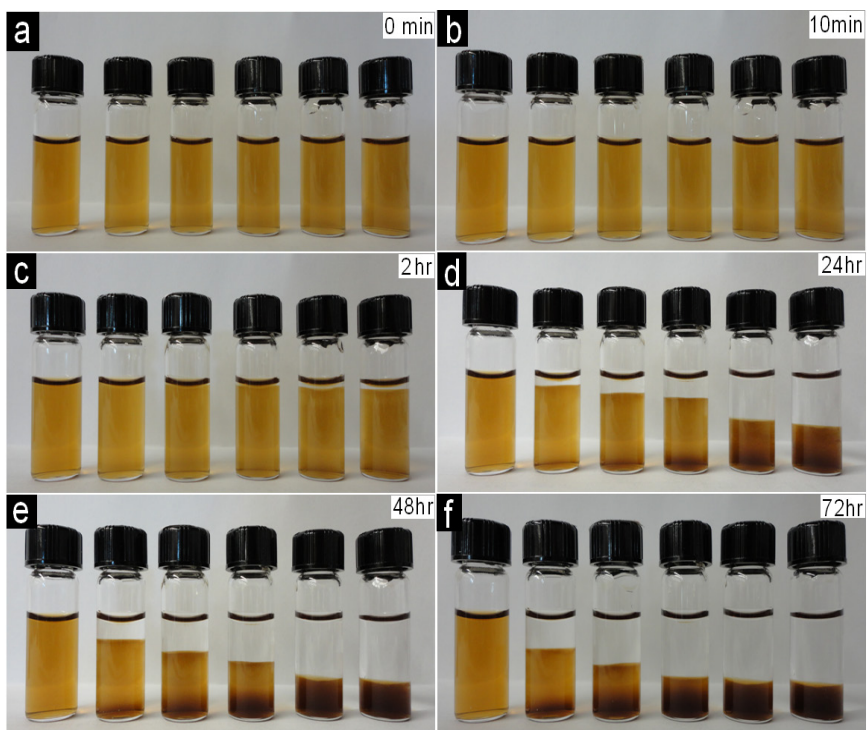


**Fig.4.4.** Precipitation of LiCl-GO solutions with different concentrations of LiCl (0, 0.1, 0.2, 0.4, 0.6, and 0.8 M, from left to right) after (a) 0 min, (b) 10 min, (c) 2 hr, (d) 24 hr, (e) 48 hr and (f) 72 hr.

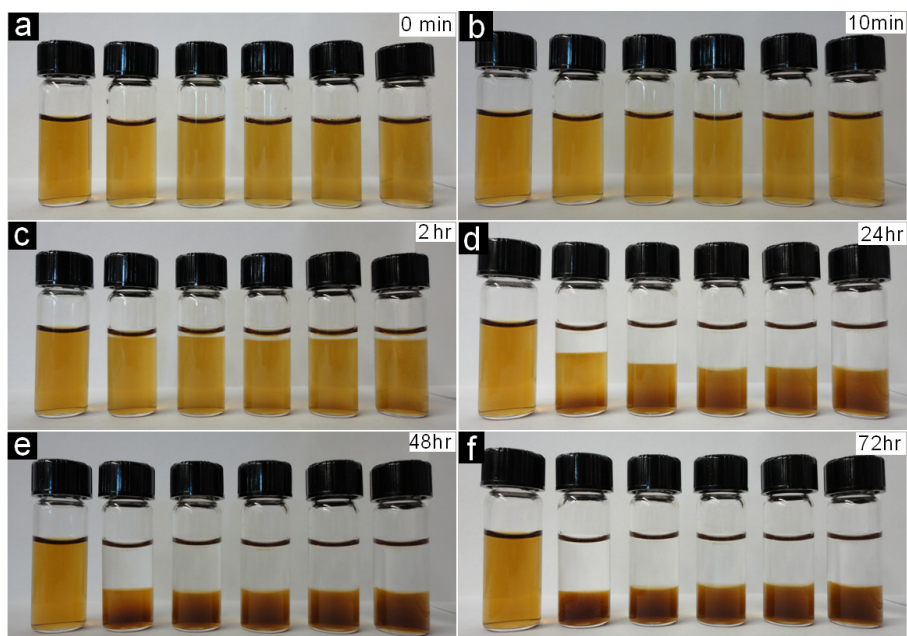


**Fig.4.5. Precipitation of HCl-GO solutions with different concentrations of HCl (0, 0.1, 0.2, 0.4, 0.6, and 0.8 M, from left to right) after (a) 0 min, (b) 10 min, (c) 2 hr, (d) 24 hr, (e) 48 hr and (f) 72 hr.**

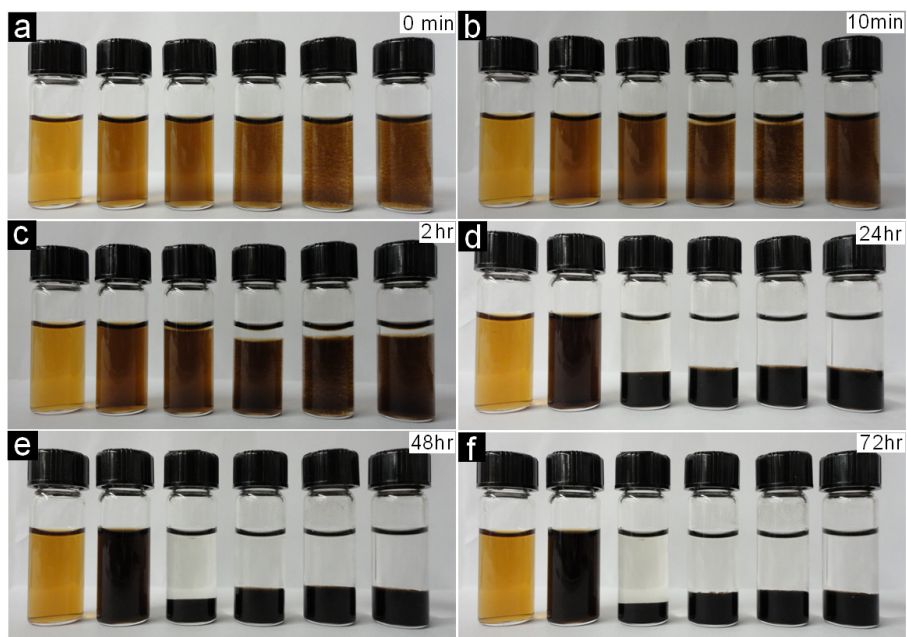


**Fig. 4.6. Precipitation of LiOH-GO solutions with different concentrations of LiOH (0, 0.1, 0.2, 0.4, 0.6, and 0.8 M, from left to right) after (a) 0 min, (b) 10 min, (c) 2 hr, (d) 24 hr, (e) 48 hr, and (f) 72 hr.**

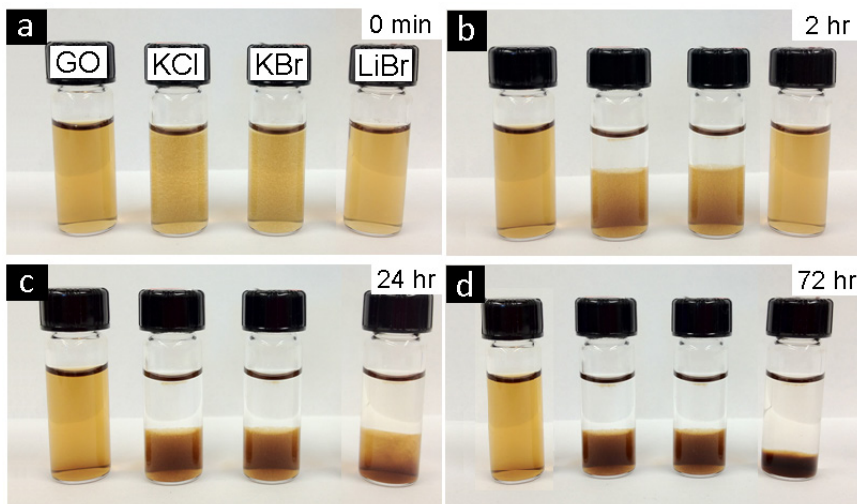


**Fig.4.7. Precipitation in aqueous solutions of GO, 0.4 M KCl-GO, 0.4 M KBr-GO, and 0.4 M LiBr (from left to right) after (a) 0 min, (b) 2 hr, (c) 24 hr, and (d) 72 hr.**

The precipitation phenomenon can be further confirmed by UV–visible spectra of GO solution and colorless top supernatants after introducing HCl, LiCl, and LiOH. As shown in Fig. 4.8a, the pure GO solution has a strong absorbance with a maximum peak at 231 nm and a shoulder at about 300 nm. The peak and the shoulder can be attributed to the  $\pi \rightarrow \pi^*$  transition of aromatic C-C bonds and the  $n \rightarrow \pi^*$  transition of C=O bonds, respectively.<sup>212,213</sup> In contrast, no absorption peak corresponding to GO sheets can be observed in the UV–visible spectra of top supernatants in three cases (Fig.4.8 b–d), indicating that all GO sheets in aqueous solution precipitated. Similar phenomenon happened when LiCl, HCl, and LiOH concentrations were varied. UV–visible spectra of top supernatants in three electrolyte cases were shown in Figs.4.9-11.

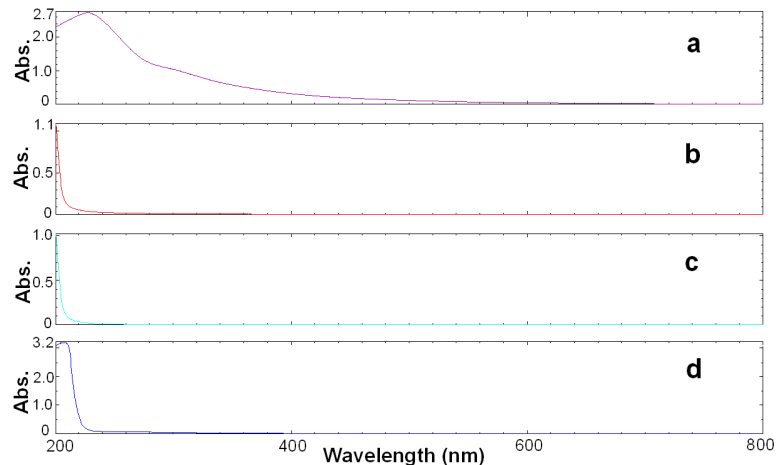


**Fig.4.8. UV-vis absorption spectra of (a) GO solution, (b) top supernatant of 0.4 M LiCl-GO solution after precipitation, (c) top supernatant of 0.4 M HCl-GO solution after precipitation, and (d) top supernatant of 0.4 M LiOH-GO after precipitation.**

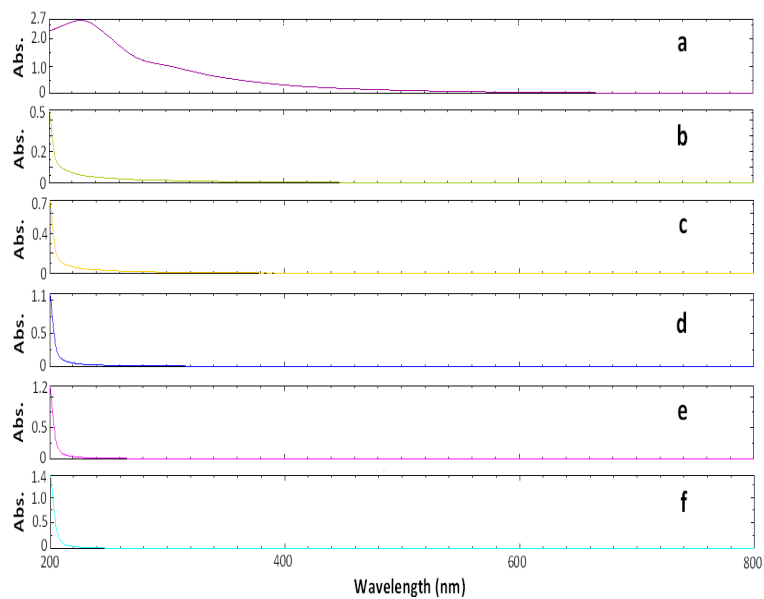


**Fig.4.9. UV-vis absorption spectra of GO solution (a) and top supernatants (after precipitation) of LiCl-GO solutions with various LiCl concentrations: (b) 0.1 M, (c) 0.2 M, (d) 0.4 M, (e) 0.6 M, and (f) 0.8 M.**



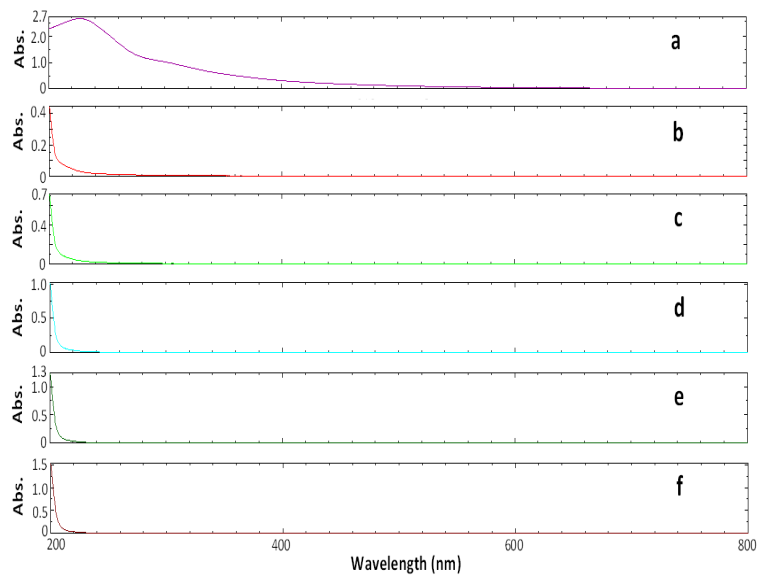


**Fig.4.10. UV-vis absorption spectra of GO solution (a) and top supernatants (after precipitation) of HCl-GO solutions with various concentrations of HCl: (b) 0.1 M, (c) 0.2 M, (d) 0.4 M, (e) 0.6 M, and (f) 0.8 M.**

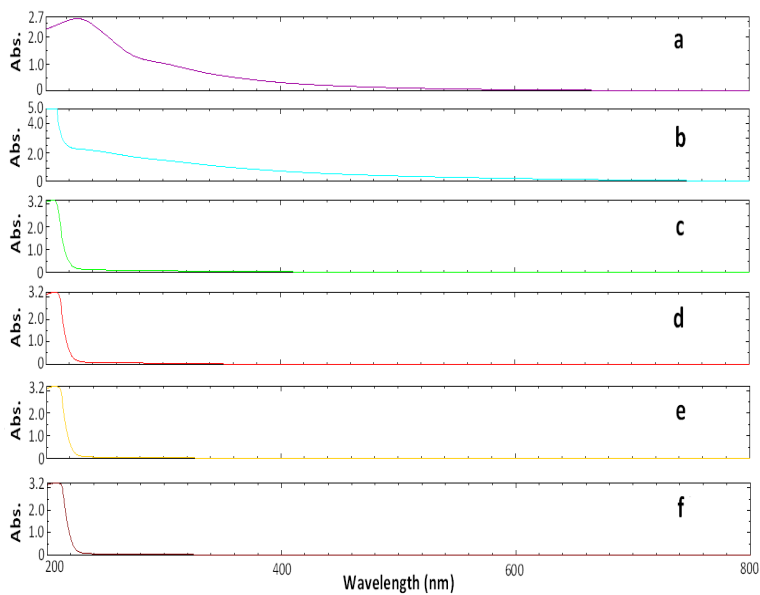


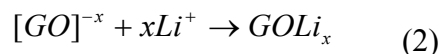
**Fig.4.11. UV-vis absorption spectra of GO solution (a) and top supernatants (after precipitation) of LiOH-GO solutions with various concentrations of LiOH: (b) 0.1 M, (c) 0.2 M, (d) 0.4 M, (e) 0.6 M, and (f) 0.8 M.**

It is well known that, when dispersed in water, GO sheets are highly negatively charged due to ionizable carboxylic acid groups (COOH).<sup>194,197</sup> The negative charges of GO sheets generate repulsive electrostatic interaction between the sheets, which is larger than van der Waals attractive force to prevent the aggregation of GO sheets. Furthermore, the ionization of the carboxylic acid groups could lead to the acidity of GO solution (pH = 6.4), indicating that GO solution is a kind of weak acid. Therefore, GO actually can be represented as  $GOH_x$  and an equilibrium exists in aqueous GO solution as follows:



HCl is a strong acid. When it is introduced into aqueous GO solution, HCl totally dissociates into  $H^+$  and  $Cl^-$  ions. This means that the  $H^+$  ions from HCl can neutralize the negative charge of GO sheets back to  $GOH_x$ , leading to the disappearance of the repulsive electrostatic interaction between GO sheets. As a result, the attractive van der Waals interaction could cause the aggregation of GO sheets. Furthermore, GO lateral dimension of up to tens micrometers further enhances the van der Waals attraction between GO sheets, because the van der Waals interaction between two planes are much larger than two particles at the same distance.<sup>214</sup> This explains our above observation, in which HCl caused GO precipitation (Fig.4.3). When LiCl is added to aqueous GO solution, this strong electrolyte dissociates into  $Li^+$  and  $Cl^-$  ions in water. The  $Li^+$  ions could neutralize the negative charges of GO sheets to form  $GOLi_x$  (Eq. 2). As a result, the attractive van der Waals interaction could cause the aggregation of GO sheets. In the case of LiOH–GO solution, the neutralization reaction between  $OH^-$  and  $H^+$  ions results in the equilibrium (Eq.1) shifting from left to right, which could generate more charges on GO

sheets. However, the original and generated negative charges of GO sheets can quickly be neutralized by  $\text{Li}^+$  ions from  $\text{LiOH}$  to form  $\text{GOLi}_x$  (Eq. 2), resulting in the elimination of GO charges and thus the aggregation of GO sheets. Therefore, the precipitation of GO sheets in aqueous solution (due to the introduction of  $\text{HCl}$  acid,  $\text{LiOH}$  base, or  $\text{LiCl}$  salt) can be explained by the neutralization of charge. In other words, electrostatic repulsion plays the most important role in keeping the stability of aqueous GO solutions.



It would be noted that the effect of a base on the aqueous GO solution may be more complicated. Fan et al. found that a strong base ( $\text{NaOH}$  or  $\text{KOH}$ ) caused the color change of aqueous GO solution.<sup>215</sup> They attributed the color change to the deoxygenation of GO in a strong base. Furthermore, Rourke et al. found that, at high concentration of  $\text{NaOH}$ , the initial transparent brown suspension of GO separated into a black aggregation and a colorless supernatant solution.<sup>216</sup> This aggregation of GO was attributed to the elimination of highly oxidative GO debris (adhered to large GO sheets as an effective surfactant) by  $\text{NaOH}$ . Therefore, a strong base may affect aqueous GO solution via neutralizing charges, deoxygenating, and removing highly oxidative GO debris. That will be further evaluated in the following sections.

It was demonstrated that the high concentration of ions from a strong electrolyte could screen the repulsive force between nanosheets.<sup>217-219</sup> The Debye length, which characterizes the distance for the appearance of significant charge separation, is inversely proportional to ion concentrations in the solution.<sup>220</sup> The addition of strong electrolytes ( $\text{LiCl}$ ,  $\text{HCl}$ , and  $\text{LiOH}$ ) to GO solution decreased the Debye length and increased the

screening of repulsive electrostatic forces. This would also contribute to the electrolyte-induced aggregation of GO sheets.

#### 4.3.2. Characterization of GO precipitates

The UV–visible spectra of GO precipitates in three cases (HCl–GO, LiCl–GO, and LiOH–GO) were obtained and shown in Fig.4.12. In contrast with top supernatants, GO aggregations in three cases all showed strong absorbance in a large range of 200–800 nm. The UV–vis spectra of the precipitates obtained from acid and salt cases exhibited GO characteristic feature—a maximum peak at 231 nm and a weak shoulder at 300 nm. However, the precipitates from GO–LiOH solution showed different feature of UV–vis absorbance, namely, there is enhanced absorbance in 300–800 nm without the maximum peak at 231 nm. This indicates that GO sheets have been partially reduced (or deoxygenated) by LiOH.

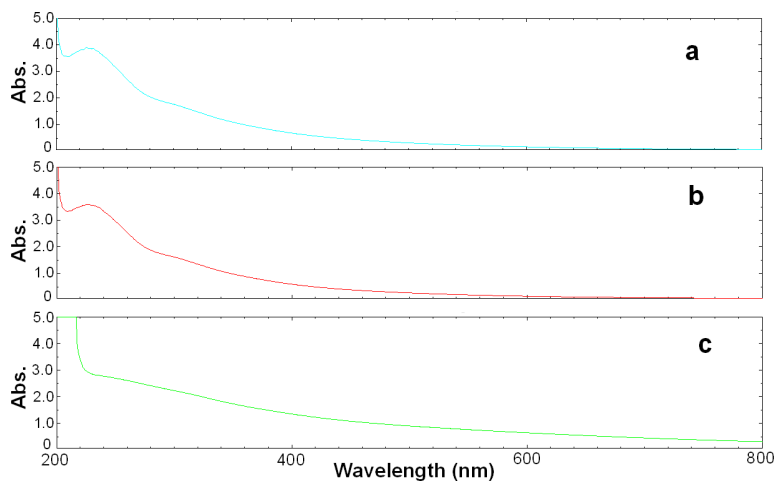


**Fig.4.12. UV–Vis absorption spectra of GO precipitates from (a) 0.4 M LiCl–GO solution, (b) 0.4 M HCl–GO solution, and (c) 0.4 M LiOH–GO solution.**

Transmission electron microscopy (TEM) was employed to evaluate the morphologies of GO sheets. As shown in Fig.4.13a, a large GO sheet from the GO solution is observed. The GO sheet is not perfectly flat, but displays intrinsic wrinkles and corrugations that are common for GO sheets prepared by chemical exfoliation method.<sup>221,222</sup> Those wrinkles and folded GO sheet are formed to minimize the system energy of two dimensional membrane structures.<sup>223</sup> Furthermore, TEM images showed that GO sheets were aggregated together in the precipitates formed by introducing HCl, LiCl, or LiOH into GO solution (Fig.4.13 b-d). This further supports that the neutralization of GO charges caused the GO aggregation in the aqueous GO solution. In addition, a large amount of small pieces were observed in the GO precipitates due to the addition of HCl and LiCl, but not in LiOH-induced precipitates. Rourke et al. demonstrated that the graphene oxide (prepared via graphite oxidation) contains a remarkable amount of small pieces, which are highly oxidative GO debris (such as  $C_{19}H_{15}O_6$  and  $C_{18}H_{15}O_9$ ).<sup>216</sup> They found that the debris, which is colorless in its aqueous solution, could dissolve in a strongly basic NaOH solution. Therefore, the small pieces in HCl- and LiCl-induced GO precipitates should be highly oxidative GO debris. No debris occurred in LiOH-induced GO precipitates because the debris is soluble in aqueous solution of LiOH. Furthermore, no debris was observed in the GO sheets from its aqueous solution without any electrolyte, indicating that the debris also possesses a high solubility in water. However, the oxidative GO debris is insoluble in an acidic or salt aqueous solution.

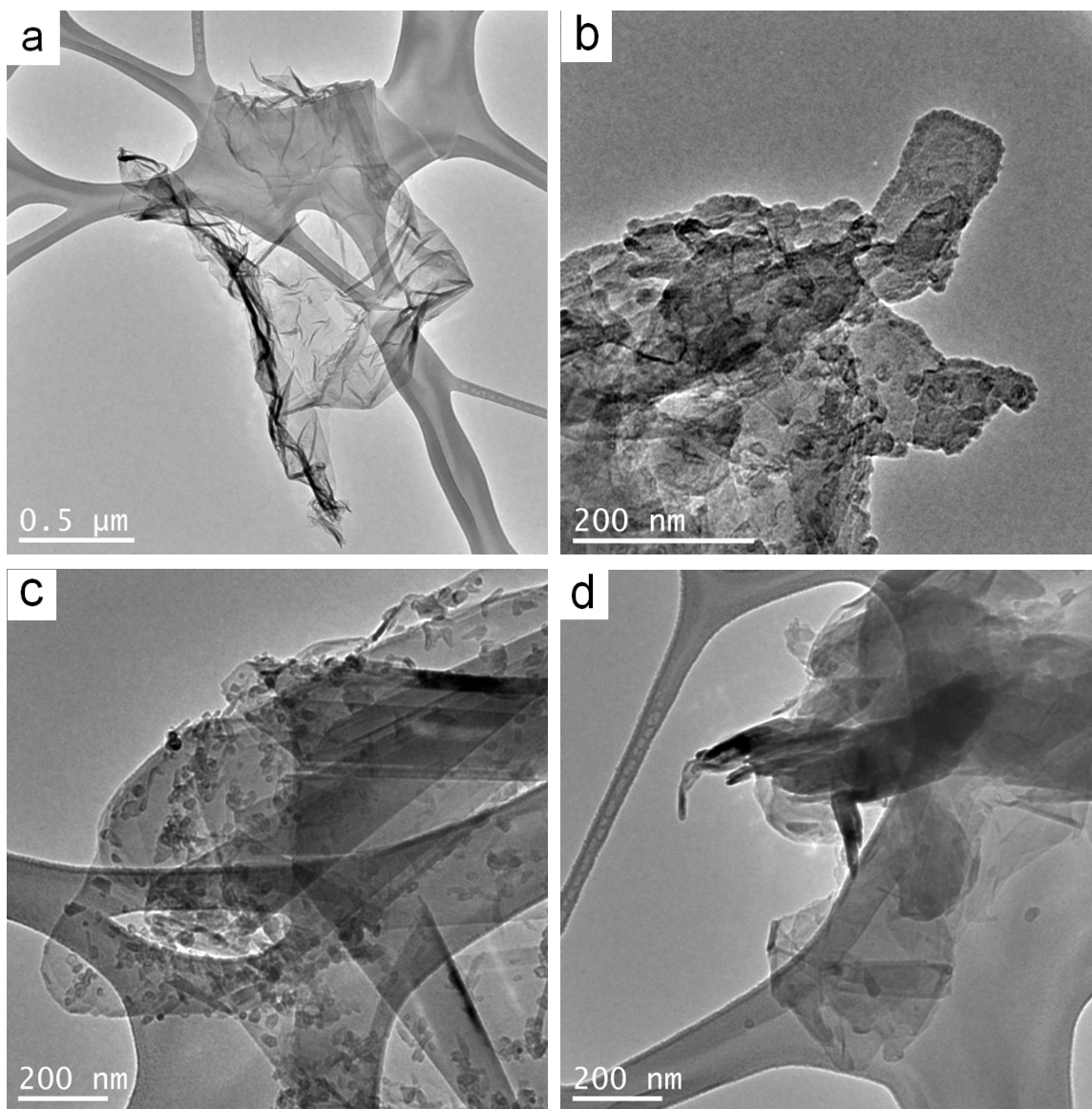


**Fig.4.13. TEM images of (a) GO sheets from GO solution, (b) LiCl-induced GO precipitate, (c) HCl-induced GO precipitate, and (d) LiOH-induced GO precipitate (Note: Straps in a, c and d are the image of sample holder).**

Raman spectroscopy was exploited to characterize the structure of the GO aggregations. It is well-known that two characteristic absorption bands are present in the Raman spectra of carbon materials: the G band at around  $1580\text{ cm}^{-1}$  corresponding to the

bondstretching of  $sp^2$  carbon pairs and the D band at around  $1330\text{ cm}^{-1}$  associated with the breathing mode of aromatic rings with dangling bonds in plane terminations.<sup>88,224</sup> As shown in Fig.4.14a, one can see both G and D bands for GO sample. The intense D bands can be attributed to the presence of defects due to oxygenizing functional groups. This is consistent with reported observations.<sup>189,195</sup> Furthermore, both G and D bands can also be observed for HCl- and LiOH-induced GO precipitates (Fig.4.14 b and c), which should be due to oxygen-containing functional groups (see FTIR spectra in the following paragraph). The ratio of the D band intensity ( $I_D$ ) to the G band one ( $I_G$ ) is usually employed to evaluate the size of the in-plane  $sp^2$  domains for carbon materials.<sup>224</sup> We calculated the  $I_D/I_G$  ratios, which are 1.15, 1.04, and 1.01 for original GO sheets, HCl-induced GO precipitates and LiOH-induced GO precipitates, respectively. The  $I_D/I_G$  ratio of original GO sheets is larger than those of HCl- and LiOH-induced precipitates, indicating that the average size of the  $sp^2$  domains in the GO precipitates increased due to stacking GO sheets.

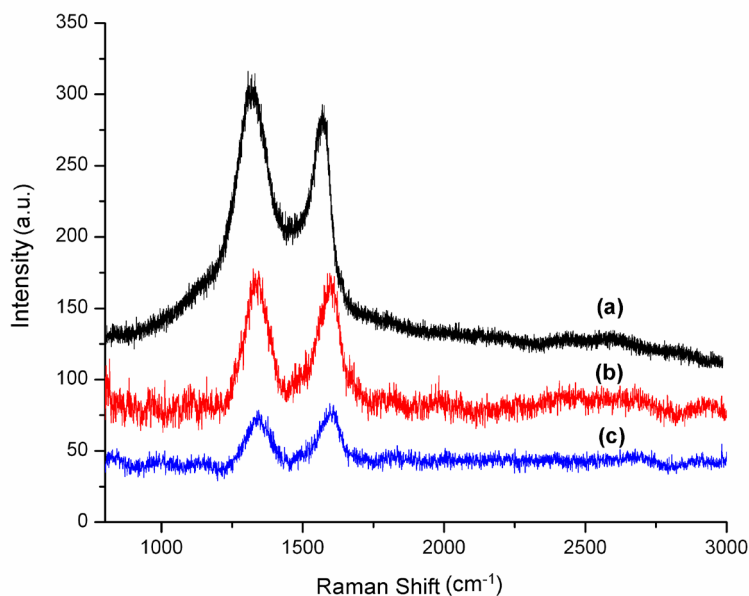


**Fig.4.14. Raman spectra of (a) GO sheets from GO solution, (b) HCl-induced GO precipitate, and (c) LiOH-induced GO precipitate.**

Functional groups in GO aggregations were evaluated by FTIR (Fig.4.15). As shown in Fig.4.15a, one can observe a wide and broad peak at 3400 cm<sup>-1</sup> attributed to O-H stretching vibrations, two peaks associated with the C=O and C-O stretching vibrations of carboxyl group at 1720 and 1400 cm<sup>-1</sup>, a peak due to stretching vibration of C-O of epoxy group at 1100 cm<sup>-1</sup>, and one corresponding to C=C stretching vibration of unoxidized aromatic C=C bonds at 1620 cm<sup>-1</sup>.<sup>226,227</sup> The C-O-H bending vibrations of GO hydroxyl groups (C-OH) can also contribute to the peak at 1400 cm<sup>-1</sup>.<sup>228,229</sup> Therefore, the GO sheets contain three functional groups: carboxyl, epoxy, and hydroxyl groups. After introducing HCl into the GO solution, the obtained GO precipitate exhibited similar FTIR absorption with that of original GO (Fig.4.15 a and b). This indicates that the HCl-induced GO precipitate possesses the same types of functional groups as original GO.



However, the IR spectrum of LiOH-induced GO precipitate exhibits intense absorption peaks at  $3400\text{ cm}^{-1}$ ,  $1620\text{ cm}^{-1}$ , and  $1400\text{ cm}^{-1}$ . The strong peak at  $3400\text{ cm}^{-1}$  can be attributed to the O-H stretching vibration of hydroxyl groups of LiOH and GO. Another strong peak at  $1400\text{ cm}^{-1}$  should be the C-O-H bending vibration of GO hydroxyl groups (C-OH). The disappearance of absorption band at  $1720\text{ cm}^{-1}$ , which is associated with the C=O stretching vibration of carboxyl group, indicates the partial reduction of GO by LiOH. This partial reduction could be further supported by the increased intensity of absorption band at  $1620\text{ cm}^{-1}$ , which corresponds to aromatic C=C stretching vibration. This is consistent with the above UV-visible observation. It is worth to note that a reliable Raman and FTIR spectra could not be obtained for LiCl-induced GO precipitate due to its strong absorption of  $\text{H}_2\text{O}$  from air during measurements.

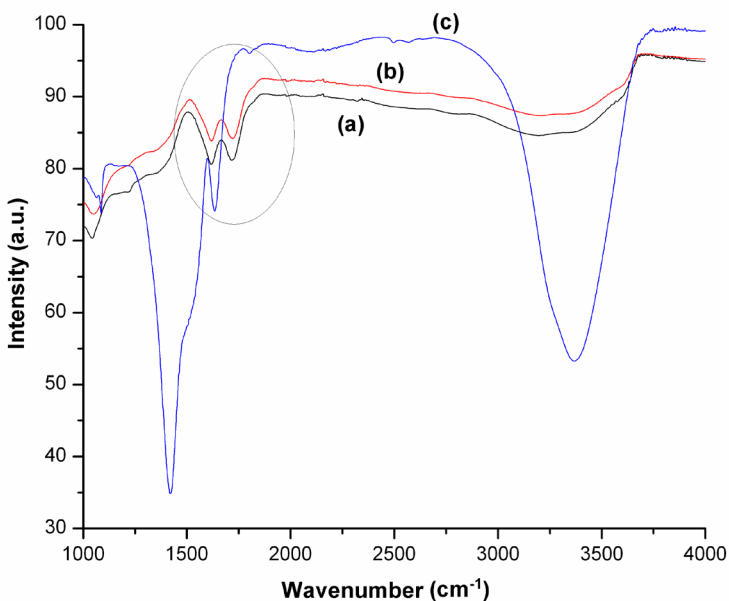


**Fig.4.15. FTIR spectra of (a) GO sheets from GO solution, (b) HCl-induced GO precipitate, and (c) LiOH-induced GO precipitate.**

### 4.3.3 Application of GO precipitation for DSSCs

The dye-sensitized solar cell (DSSC) is a representative of the third generation photovoltaic devices.<sup>21-24</sup> Platinum-loaded conducting glass has been widely exploited as counter electrodes (CEs) for DSSCs. However, the high cost and the rare source of platinum would limit its practical DSSC application. This promoted an interest to develop carbon-based counter electrode catalysts for DSSCs.<sup>230,231</sup> It would be important to find an effective method for coating carbon material on a substrate as counter electrode catalyst. For this reason, we explored the possibility of electrolyte-induced GO precipitation to prepare GO-based counter electrodes. Three DSSC counter electrodes were fabricated by depositing GO on FTO glass plates via HCl-, LiCl-, and LiOH-induced precipitation, respectively. The deposited GO layers were thermally treated at 400 °C, leading to the thermal reduction of GO to graphene. The performance test results of those DSSCs are listed in Table 4.1. The DSSC with HCl-induced GO precipitate as a counter electrode exhibited the power conversion efficiency of 1.65%, whereas the power conversion efficiencies of other two DSSCs (with LiCl- and LiOH-induced GO precipitates as counter electrodes) are negligible. Furthermore, SEM morphology measurements showed that the bare FTO glass has a rough surface structure (Fig. 4.16a). In contrast, the coating via HCl-induced GO precipitation generated a smooth and uniform GO layer on the FTO glass (Fig. 4.16b). This indicates that HCl-induced GO precipitation may be a simple method to prepare GO-based counter electrode for DSSCs. Furthermore, its preliminary efficiency (1.65%), which is not high enough for

commercial application, is good enough for us to pursue the future research for a much higher efficiency.

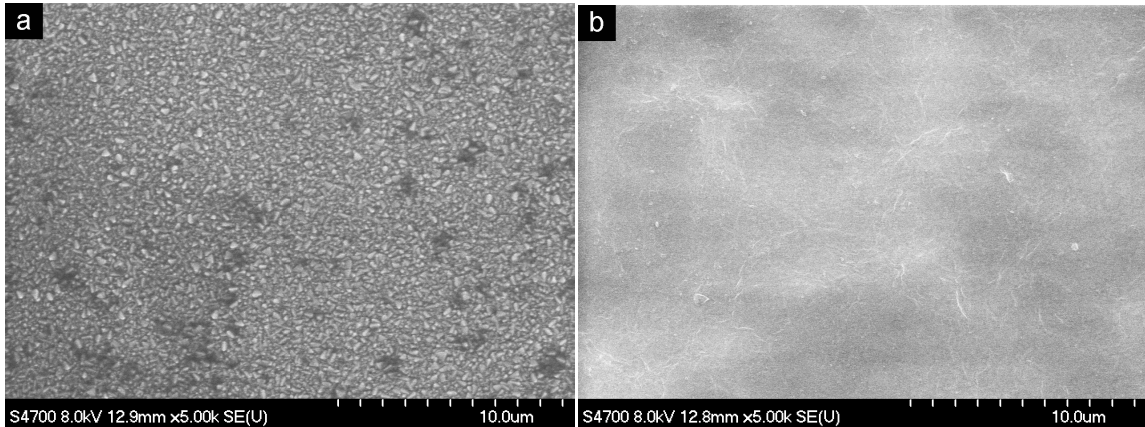


**Fig.4.16. FESEM images: (a) FTO glass substrate and (b) FTO glass coated with HCl-induced GO precipitate.**

**Table 4.1. Photovoltaic performances of DSSCs with GO precipitates on ITO glasses as the counter electrode**

Sample No.	Counter electrode	$J_{sc}$ (mA/cm <sup>2</sup> )	$V_{oc}$ (V)	FF	$\eta$ (%)
1	HCl-GO	13.0	0.67	0.19	1.65
2	LiCl-GO	1.1	0.56	0.21	0.13
3	LiOH-GO	1.7	0.54	0.25	0.23

*Note:  $J_{sc}$  is short circuit current density,  $V_{oc}$  open circuit voltage, FF fill factor, and  $\eta$ : power conversion efficiency.*

#### 4.4 Conclusion

Aqueous GO solution can easily be destabilized by a strong electrolyte (acid, base or salt), leading to GO precipitation. It was showed that electrostatic repulsion plays the most important role in keeping the stability of the aqueous GO solutions. The electrolyte-

induced precipitates were characterized by TEM, Raman spectroscopy, and FTIR. It was found that HCl- and LiCl-induced precipitations could not change the functional groups of GO sheets, which are carboxyl, epoxy, and hydroxyl groups. In contrast, during the LiOH-induced GO precipitation, the carboxyl group of GO sheets disappeared with a remarkable increase in hydroxyl group and aromatic C=C bonds. This indicates that the LiOH-induced GO precipitation resulted in the partial reduction of GO sheets. Furthermore, the HCl-induced GO precipitation is a feasible approach to deposit GO sheets on a substrate as a Pt-free counter electrode for a dye-sensitized solar cell (DSSC), which exhibited 1.65% of power conversion efficiency.

## Chapter 5 Three-Dimensional Honeycomb-like Structured

### Graphene\*

#### 5.1 Introduction

Graphene, a two-dimensional (2D) carbon sheet with one-atom thickness,<sup>30</sup> has attracted great interest due to its unique properties.<sup>99,232</sup> To explore its practical applications, large-scale synthesis with controllable integration of individual graphene sheets is essential. So far, numerous approaches have been developed for graphene synthesis, including mechanical cleavage<sup>30</sup>, epitaxial growth,<sup>233</sup> and chemical vapor deposition.<sup>67</sup> All of those techniques are widely used to prepare flat graphene sheets on a substrate. Chemical exfoliation of graphite has been applied to prepare graphene oxide solutions and graphene-based composite materials.<sup>84,224</sup>

Recently, tuning graphene shapes is attracting much attention.<sup>234-236</sup> It is believed that developing 3D structures of graphene will further expand its significance in applications. Cheng and his co-workers synthesized graphene foam using porous Ni foam as a template for the CVD growth of graphene, followed by etching away the Ni skeleton.<sup>237</sup> The graphene foam consists of an interconnected flexible network of graphene as the fast transport channel of charge carrier for high electrical conductivity.

---

\*The material contained in this chapter was previously published in *Angew. Chem. Inter. Ed.* 2013, 52, 9210-9214 by Hui Wang, Yun Hang Hu and other coauthors. See Appendix K for documentation of permission to republish this material.

Ruoff et al. prepared porous graphene paper from microwave exfoliated graphene oxide by KOH activation.<sup>238</sup> The porous graphene, which possesses an ultra-high surface area and a high electrical conductivity, was exploited for supercapacitor cells, leading to high values of gravimetric capacitance and energy density. Feng, Müllen and their coworkers synthesized hierarchical macro- and mesoporous graphene frameworks (GFs).<sup>239-241</sup> The GFs exhibited excellent performance for electrochemical capacitive energy storage. Yu et al.<sup>242</sup> synthesized graphene tubes on Pd nanowire templates using plasma-enhanced chemical vapor deposition (PECVD), followed by etching metal nanowire. Qu et al.<sup>243</sup> fabricated meter-long graphene microtubes with a tunable diameter that could be selectively functionalized for desirable applications. Choi et al. synthesized macroporous graphene using polystyrene colloidal particles as sacrificial templates in graphene oxide suspension,<sup>244</sup> and the pore sizes can be tuned by controlling template particle size.<sup>245</sup> Actually, those important research works represent a frontier topic—tuning properties of graphene sheets via controlling their shapes.

In this work, we developed a novel strategy for the synthesis of graphene with 3D Honeycomb-like Structure via a simple reaction between  $\text{Li}_2\text{O}$  and  $\text{CO}$ . As shown in Fig.5.1,  $\text{Li}_2\text{O}$  reacts with  $\text{CO}$  to form  $\text{Li}_2\text{CO}_3$  and honeycomb structured graphene simultaneously. The formation of  $\text{Li}_2\text{CO}_3$  not only can isolate graphene sheets from each other to prevent graphite formation during the process, but also play a role in determining the locally curved shape of graphene sheets. Honeycomb structured graphene could be obtained after removing  $\text{Li}_2\text{CO}_3$  by acid washing.

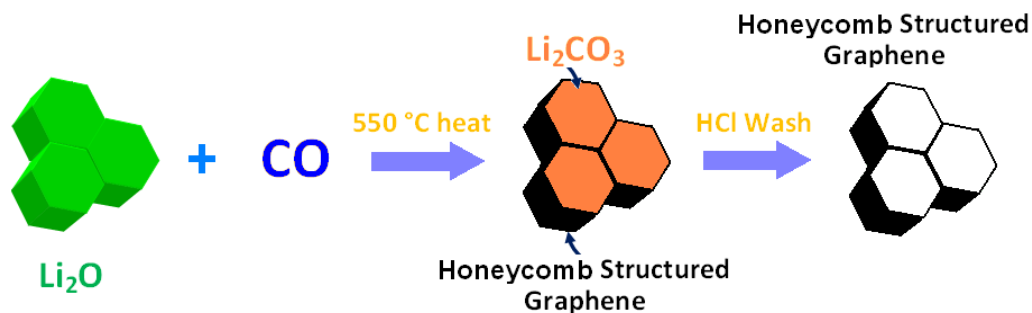
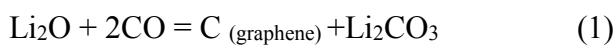


**Fig.5.1.** The proposed synthesis process of Honeycomb Structured Graphene.

## 5.2 Thermodynamic Calculation

$\text{Li}_2\text{O}$  is widely exploited as a promoter in catalysts to inhibit carbon formation.<sup>246</sup> However, this general recognition would be challenged by this work, in which  $\text{Li}_2\text{O}$  is used to react with  $\text{CO}$  to form graphene-structured carbon:



This strategy is supported by our thermodynamic calculations: Its Gibbs free energy change is negative from room temperature to  $1000\text{ }^\circ\text{C}$ , indicating that this reaction is thermodynamically favorable (Fig.5.2). Its negative enthalpy change ( $\Delta H_{298} = -397.5\text{ kJ mol}^{-1}$ ) suggests it as an energy-economic process. Furthermore, simultaneous formation of  $\text{Li}_2\text{CO}_3$  with graphene can isolate graphene sheets from each other to prevent graphite formation during the process. On the other hand, the  $\text{Li}_2\text{CO}_3$  particles will also play a role in determining the locally curved shape of graphene sheets. The feasibility of this novel approach was confirmed by following experiments.

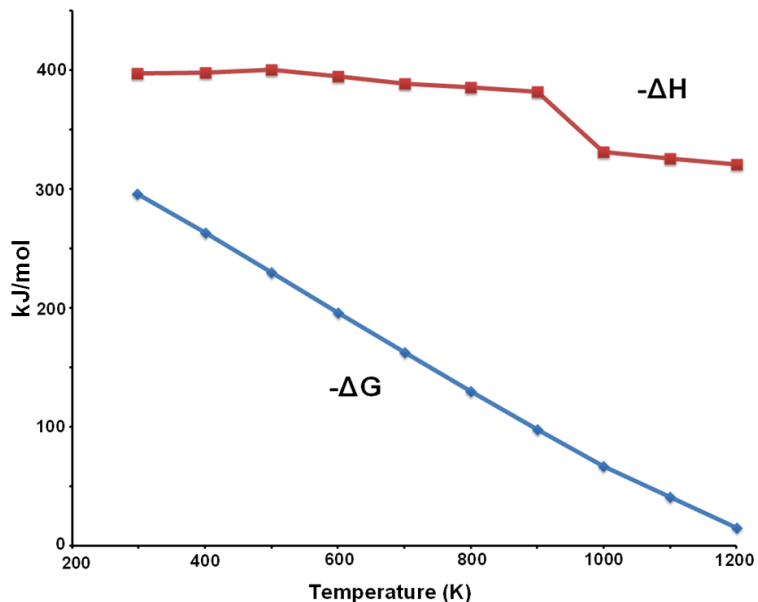


**Fig.5.2. Relationships of Gibbs free energy change ( $\Delta G$ ) and reaction enthalpy change ( $\Delta H$ ) with temperature for reaction between  $\text{Li}_2\text{O}$  and  $\text{CO}$  to graphene and  $\text{Li}_2\text{CO}_3$ . (The drop appeared in enthalpy change is due to phase transformation)**

## 5.3 Experimental

### 5.3.1 Synthesis of graphene with honeycomb-like structure

Lithium oxide ( $\text{Li}_2\text{O}$ ) power (Aldrich) was loaded into a ceramic tube reactor and exposed to  $\text{CO}$  at pressure of 35 psi. The reactor temperature increased from room temperature to target temperature  $550\text{ }^\circ\text{C}$  at a rate of  $10\text{ }^\circ\text{C}/\text{min}$  and then kept at that temperature for 12 h, followed by cooling down to room temperature. This solid product was treated by 36.5 wt% hydrochloric acid ( $\text{HCl}$ ) and washed with de-ionized water ( $\text{DW}$ ) for more than 10 times. The remained solid was separated from water by centrifugation (3600 rpm) and then dried overnight at  $80\text{ }^\circ\text{C}$  to get graphene powder. The



same preparation procedure was repeated to prepare samples treated at 550 °C for 24 h and 48 h, respectively.

### 5.3.2 Characterization

**Powder X-ray diffraction (XRD):** All solid products before and after acid wash were subjected to X-ray diffraction (XRD) measurements by a Scintag XDS 2000 Powder Diffractometer with Cu K $\alpha$  ( $\lambda=1.5406$  Å) radiation in the range of  $10 \leq 2\theta \leq 70^\circ$ .

**Field emission scanning electron microscope (FE-SEM):** The morphology of synthesized graphene was investigated by a Hitachi-4700 field emission scanning electron microscope (FESEM) with energy dispersive spectroscopy (EDS).

**Transmission electron microscopy (TEM):** TEM images, selected area electron diffraction (SAED), and electron energy loss spectroscopy (EELS) were performed in a JEOL JEM2010F electron microscope that can be performed in both TEM and scanning transmission electron microscopy (STEM) modes. EELS was performed in STEM mode with a 0.2 nm probe size and a 12mrad beam convergent angle and 32mrad collection angle, respectively.



**Fig.5.3. JEOL JEM2010F Electron Microscope.**

**Raman spectroscopy:** Raman spectra of graphene were obtained using an Olympus BX41 spectrometer with a helium-neon laser to excite the samples.

**X-ray photoelectron spectroscopy (XPS):** XPS was exploited to analyze the structure of graphene sheets using SPECS surface nano analysis GbmH instrument equipped with Al  $K\alpha$  monochromator.



**Fig.5.4. SPECS Surface Nano Analysis.**

**Elemental Analyses:** The elemental composition of graphene was recorded using a Control Equipment Corp. Model 240XA analyzer.



**Fig.5.5. CEC 240 XA Elemental Analyzer.**

**Sheet resistance measurement:** Sheet resistance of graphene film was measured by Jandel four-point probe system with RM3 test unit.



**Fig.5.6. Jandel Four-Point Probe System with RM3 Test Unit.**

## **5.4 Results and Discussion**

### **5.4.1 X-ray diffraction measurement**

1 mol of lithium oxide ( $\text{Li}_2\text{O}$ ) powder (from Aldrich) reacted with CO in temperature of 550 °C for 12, 24, or 48 h. The products were subjected to X-ray diffraction measurements. As shown in Fig.5.7, diffraction peaks of  $\text{Li}_2\text{CO}_3$  can be observed, confirming the reaction between  $\text{Li}_2\text{O}$  and CO. The diffraction peaks located at 21.5, 30.6, and 31.7° correspond to diffraction planes (110), (-202), and (002) of  $\text{Li}_2\text{CO}_3$ . The conversions of  $\text{Li}_2\text{O}$  are obtained through volume fraction calculation, which are 94, 95, and 97% for 12, 24, and 48h, respectively. The average crystal size of  $\text{Li}_2\text{CO}_3$  is calculated using Debye-Scherrer equation:

$$D = \frac{0.94\lambda}{\beta \cos \theta}$$

where  $\lambda$  is the X-ray wavelength,  $\beta$  the full width at half-maximum (FWHM) of a diffraction peak,  $\theta$  the Bragg angle. The calculation result reveals that  $\text{Li}_2\text{CO}_3$  has the crystal size at around 40 nm. After the products were treated by hydrochloric acid to remove  $\text{Li}_2\text{O}$  and  $\text{Li}_2\text{CO}_3$ , followed by washing with  $\text{H}_2\text{O}$  and drying at 80 °C, the black powder was obtained and identified as carbon by elementary analysis. Furthermore, the XRD patterns of black powders (Fig.5.8) show one broad diffraction peak of  $2\theta=26.4^\circ$ . The broad diffraction peak is due to lack of perfectly ordered layer structure of graphene.

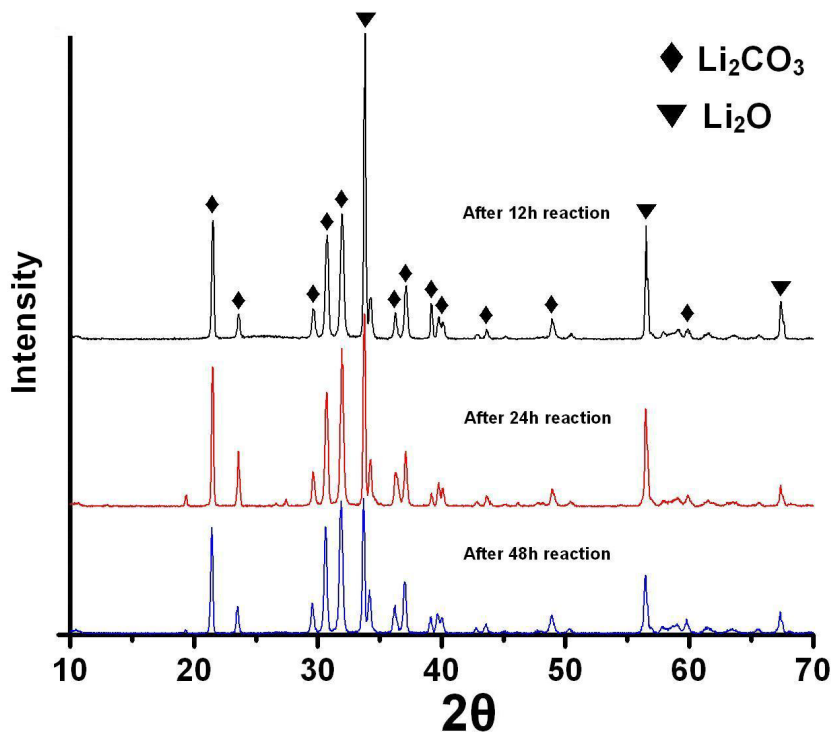


**Fig.5.7.** XRD patterns of solid products from reaction between  $\text{Li}_2\text{O}$  and  $\text{CO}$  at 550°C with three reaction times (12, 24, and 48h).

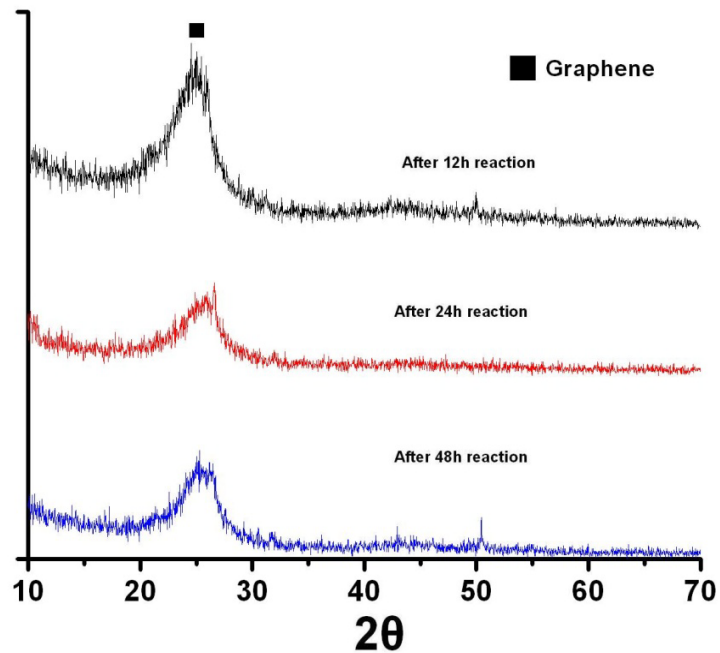


**Fig.5.8. XRD patterns of HSG powder obtained from reaction between  $\text{Li}_2\text{O}$  and  $\text{CO}$  at  $550^\circ\text{C}$  followed by hydrochloride acid wash.**

### 5.4.2 Morphology of Honeycomb Structured Graphene

The morphology of black carbon powder was evaluated by field emission scanning electron microscopy (FESEM). As shown in Fig.5.9, one can see curved graphene sheets with thickness of about 2 nm, which connect to each other and form a three-dimensional honeycomb-like structure. The cell size of graphene honeycomb lies in the range of 50-500 nm. Furthermore, 3D honeycomb-like structure of graphene doesn't show variation as increasing the reaction time from 12 h to 48 h.

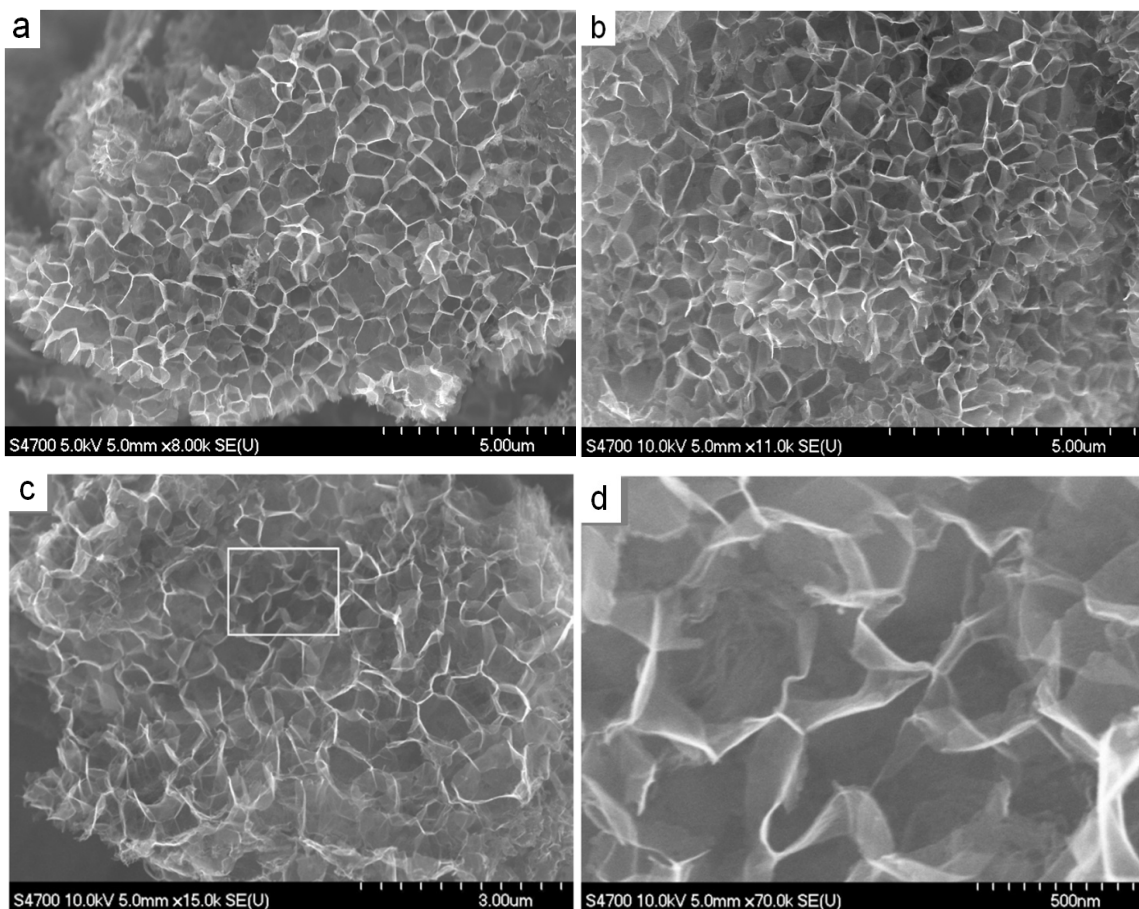


**Fig.5.9. FESEM images of graphene sheets produced from reaction between CO and Li<sub>2</sub>O for different time: (a) 12 h; (b) 24 h; (c) and (d) 48 h.**

The micro-structure of honeycomb cells was further evaluated by transmission electron microscopy (TEM). The TEM image showed the intrinsic wrinkles or corrugations of the cell sheets (Fig.5.10). Furthermore, the curved structures of honeycomb structured graphene (HSG) were further supported by electron diffraction that shows poly-crystalline ring patterns (Fig.5.10 b). Different from spot patterns of flat graphene sheets,<sup>247,248</sup> the ring diffraction patterns would be due to scrolled or folded graphene sheets.<sup>247</sup>

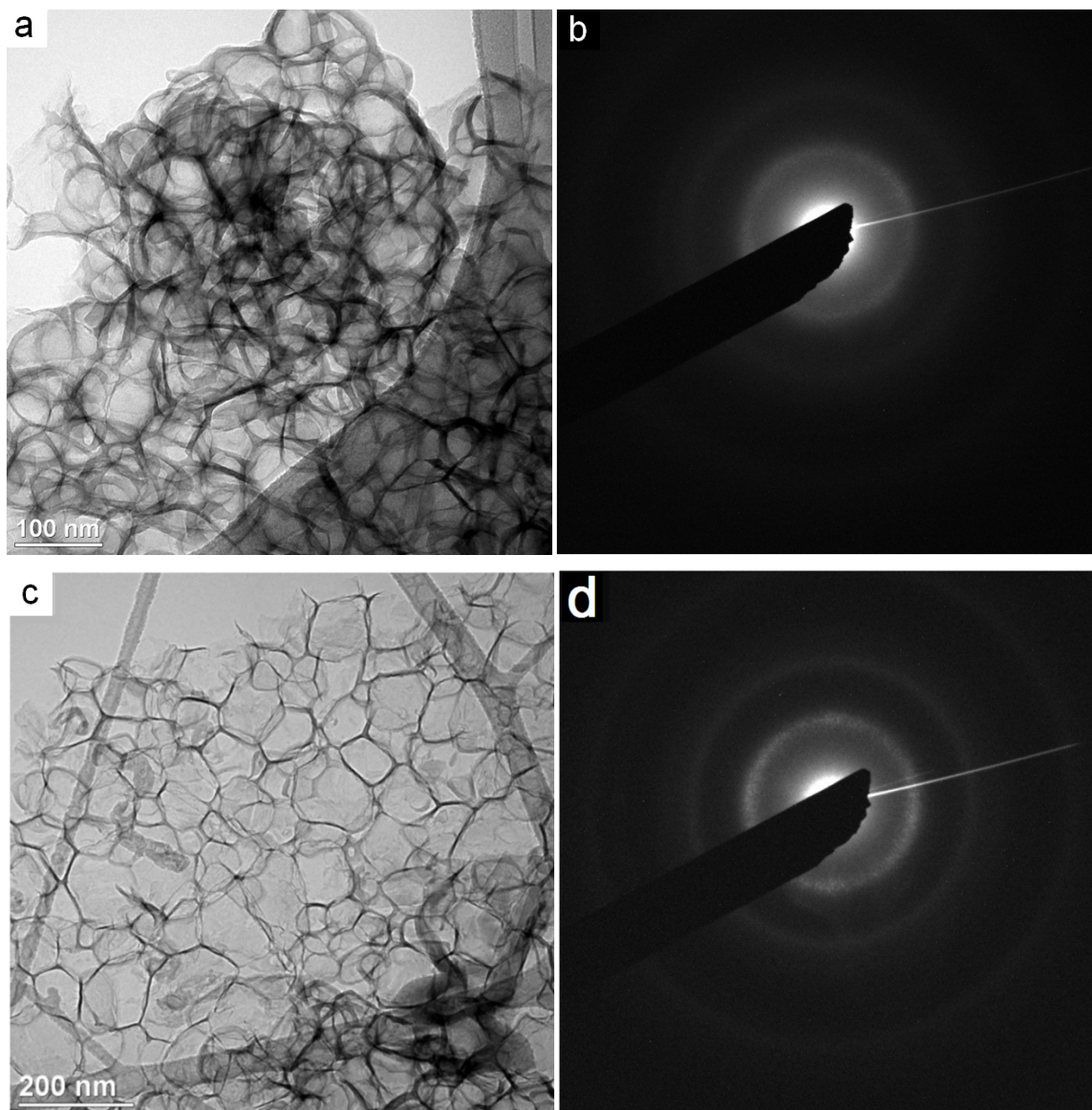


**Fig.5.10.** TEM image and electron diffraction pattern of graphene sheets produced from reaction between CO and  $\text{Li}_2\text{O}$  for (a), (b) 12 h; (c), (d) 48 h.



In addition, electron energy loss spectroscopy (EELS) spectra were used to investigate the local structure of HSG sheets. As shown in Fig. 5.11, for all four selected locations, one can see intensive feature of  $sp^2$  bonded carbon atoms in the carbon K-edge region: a peak at 285 eV corresponding to  $1s-\pi^*$  transition, and a peak at 291 eV associated with  $1s-\sigma^*$  transition.<sup>249</sup> However, obvious differences in K-edge peaks at 532 eV (associated with oxygen groups<sup>250</sup>) can be observed for different locations, namely, a large oxygen K-edge peak at 532 eV occurs at location 4, a small oxygen K-edge peak at locations 1 and 3, and no oxygen K-edge at location 2. This indicates that HSG sheets contain oxygen groups, which are heterogeneously distributed.

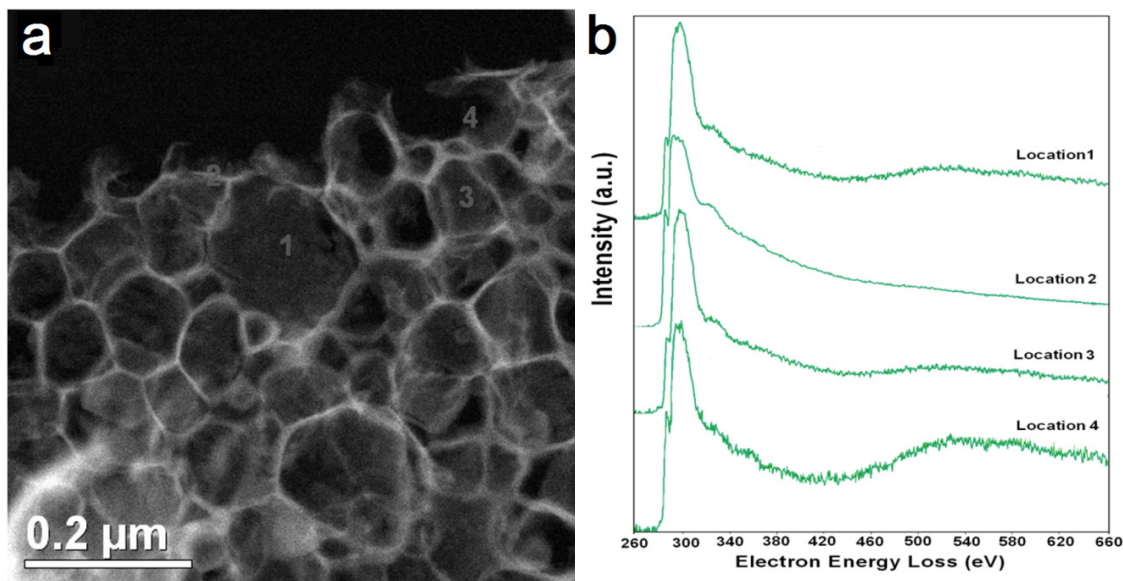


**Fig.5.11.** High-angle annular dark field (HAADF) image and b EELS for locations 1-4 for graphene sheets produced from reaction between CO and  $Li_2O$  at 550°C for 48 h.

The content of the  $sp^2$  and  $sp^3$  bonded carbon as well as oxygen groups was evaluated by X-ray photoelectron spectroscopy (XPS). As shown in Fig.5.12, one can see the C1s peak. The deconvolution of this peak revealed three components centered at 284.9, 285.7, and 286.8 eV, which would be associated with  $sp^2$  carbon,  $sp^3$  carbon, and O-C-O group.<sup>251</sup> The main component is  $sp^2$  bonded carbon (72.6-74.8%), whereas  $sp^3$  carbon (21.7-22.3%) and oxygen groups (3.5-5%) constitute a small part of graphene sheets. This is consistent with the EDS analysis that showed 94.6-97.5% carbon and 2.5-5.4% oxygen in HSG (Table 5.1). Furthermore, with increasing synthesis time for HSG, the content of  $sp^2$  bonded C increases, whereas  $sp^3$  bonded C and the C-O groups decrease.

**Table 5.1. EDS analysis of honeycomb structured graphene**

Samples*	Carbon (atomic ratio)	Oxygen (atomic ratio)
HSG-12h	94.56 %	5.44 %
HSG-24h	96.91 %	3.09 %
HSG-48h	97.44 %	2.56 %

\* *HSG-12h, HSG-24, and HSG-48 denote the honeycomb structured graphene with synthesis time of 12, 24, and 48h, respectively.*

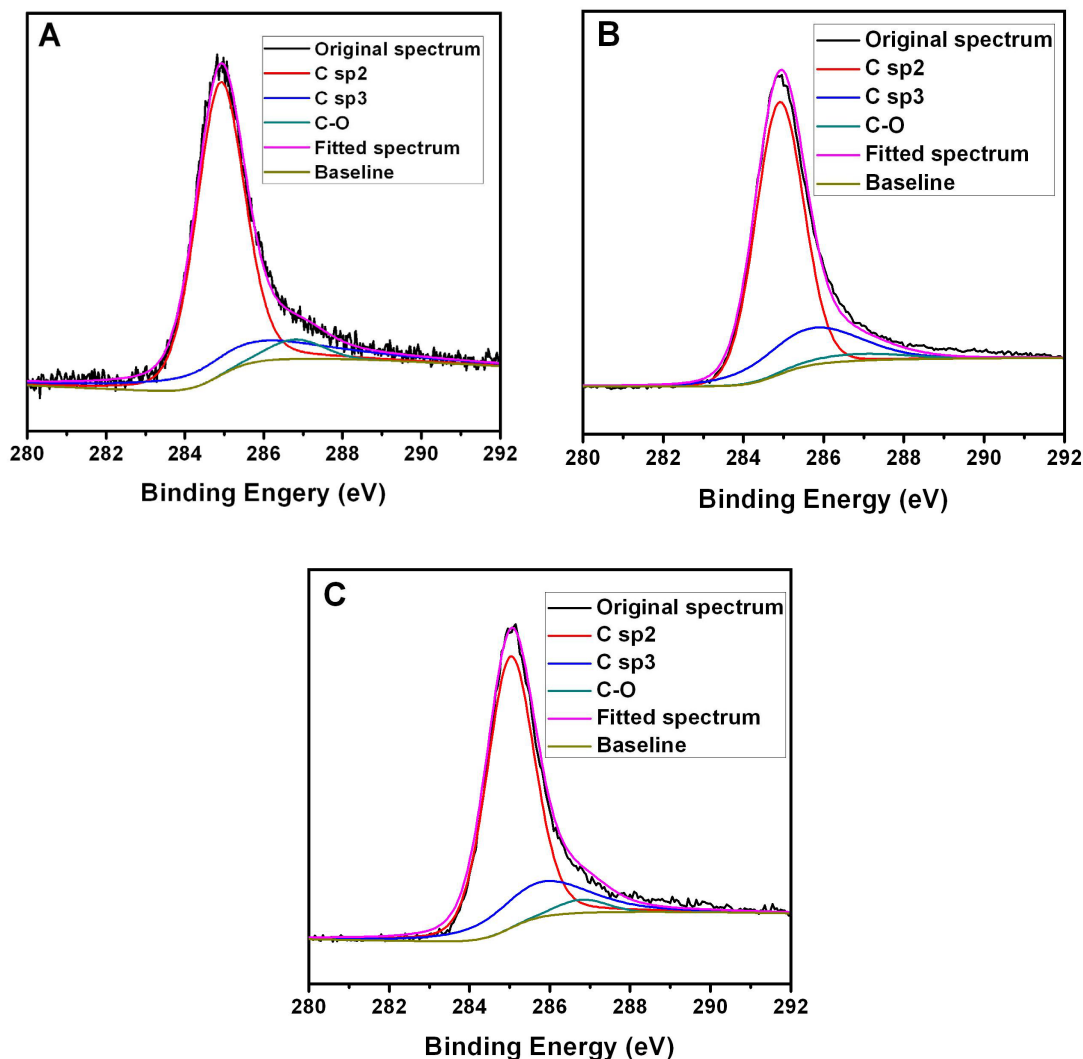


**Fig.5.12.** XPS spectra of (a) HSG-12h (honeycomb structured graphene synthesized from reaction between CO and Li<sub>2</sub>O for 12h), (b) HSG-24h and (c) HSG-48h.

Raman spectroscopy was widely exploited to reveal the defect structure of carbon materials with characteristic Raman peaks at  $\sim 1350\text{ cm}^{-1}$  (D band corresponding to the breathing mode of aromatic rings with dangling bonds) and  $\sim 1580\text{ cm}^{-1}$  (G band associated with the bond stretching of  $\text{sp}^2$  carbon pairs).<sup>88</sup> The Raman spectra of HSG exhibit an obvious G peak at  $\sim 1580\text{ cm}^{-1}$ , providing the evidence of  $\text{sp}^2$  bonded carbon

(Fig.5.13). One can also see a comparable intensity of D peak to G peak, indicating structural defects caused by oxygen-functional groups.<sup>193,252</sup> This is consistent with XPS results (Fig.5.12). Furthermore, sheet resistance of the 20  $\mu\text{m}$  HSG film on bare glass is 3.4  $\text{k}\Omega/\text{sq}$  for HSG-12h, 1.6  $\text{k}\Omega/\text{sq}$  for HSG-24h, and 0.45  $\text{k}\Omega/\text{sq}$  for HSG-48h. In contrast, CEG (graphene synthesized by chemical exfoliation of graphite) has a large sheet resistance (64  $\text{k}\Omega/\text{sq}$ ). This indicates that HSG possesses much higher conductivity than CEG. Therefore, the structural defects and the high conductivity of HSG present unique opportunities for its applications related to energy conversion and storage.

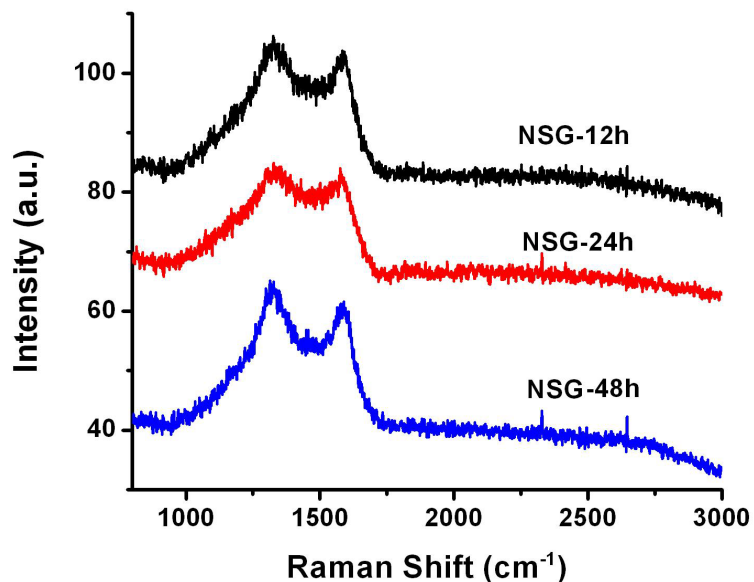


**Fig.5.13.** Raman spectra of honeycomb structured graphene (HSG) after heat treatment at 550 °C for 12 h, 24 h, and 48 h.

## 5.5 Conclusion

In summary, a novel approach, which is based on a simple reaction between  $\text{Li}_2\text{O}$  and  $\text{CO}$ , was exploited to synthesize three dimensional Honeycomb Structured graphene

sheets. The simultaneous formation of  $\text{Li}_2\text{CO}_3$  with graphene not only can isolate graphene sheets from each other to prevent graphite formation during the process, but also play a role in determining the locally curved shape of graphene sheets. After the products were treated by hydrochloric acid to remove  $\text{Li}_2\text{O}$  and  $\text{Li}_2\text{CO}_3$ , graphene sheets with a three-dimensional honeycomb-like structure were obtained. For the honeycomb structured graphene, EDS analysis reveal that there is 94.6-97.5% carbon and 2.5-5.4% oxygen. The main component is  $\text{sp}^2$  bonded carbon (72.6-74.8%), whereas  $\text{sp}^3$  carbon (21.7-22.3%) and oxygen groups (3.5-5%) constitute a small part of graphene sheets. Furthermore, these oxygen groups are heterogeneously distributed. Honeycomb structured graphene sheets have structural defects, but they exhibit excellent conductivity.

# Chapter 6 Three-Dimensional Honeycomb Structured Graphene as Counter Electrode Catalysts for Dye-sensitized Solar Cells\*

## 6.1 Introduction

Dye-sensitized solar cells (DSSCs) are currently the leading photovoltaic device with regards to third generation PVs. Since a prototype for DSSCs was reported in 1991 by O'Regan and Grätzel,<sup>21</sup> they have aroused an intense interest due to their low cost, easy fabrication, and high power conversion efficiency. As shown in Fig.6.1, a typical dye-sensitized solar cell consists of a dye-sensitized nanocrystalline TiO<sub>2</sub> film as the photoanode, a counter electrode (CE) and an electrolyte with a redox couple in the liquid or solid state.<sup>27-29</sup> The CE's task is to reduce redox species in liquid solar cells, which are used as mediators in the regeneration of the sensitizer after electron injection, or to collect holes from the hole conducting material in solid-state DSSCs. For an optimized cell, one must choose a CE material with the lowest possible sheet resistance, excellent catalytic activity for the reduction of the redox electrolyte, high chemical stability and a low cost.

---

\*The material contained in this chapter was previously published in *Angew. Chem. Inter. Ed.* 2013, 52, 9210-9214 by Hui Wang, Yun Hang Hu and other coauthors; *Energy Environ. Sci.* 2012, 5, 8182-8188 by Hui Wang and Yun Hang Hu. See Appendix K and L for documentations of permission to republish these materials.

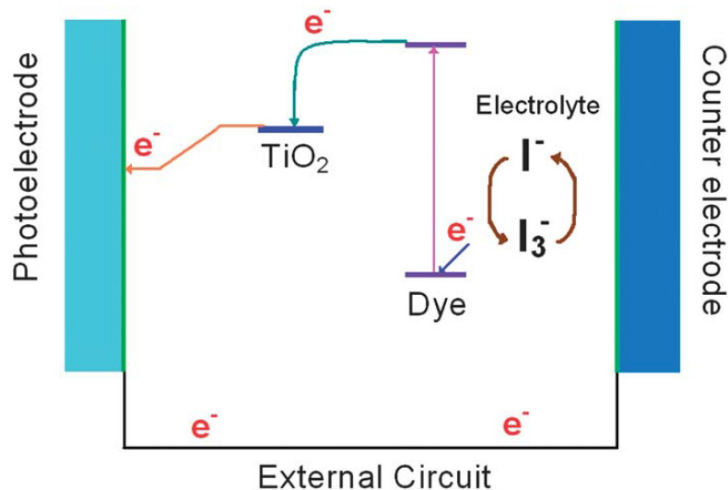
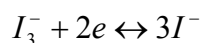


**Fig.6.1. Counter electrode in a DSSC.**

The reactions at the CE are dependent on the type of redox mediator used to transfer charge between the photoelectrode and the CE. In the case of iodide–tri-iodide couple as the redox mediator and the overall redox reaction in DSSCs can be described as following:



The tri-iodides are produced near the dye-sensitized TiO<sub>2</sub> electrode and reduced at the counter electrode. Platinum-loaded conducting glass has been widely employed as the standard CE for DSSCs due to its high catalytic activity and excellent conductivity as well as its high corrosion stability against iodine in the electrolyte.<sup>171-173</sup> However, the combination between the limited resource of platinum and the large application of platinum-based catalysts in the vehicle industry makes platinum extremely expensive and in diminishing supply. Therefore, it is important to explore Pt-free materials to replace the Pt counter electrode for DSSCs.<sup>171</sup> For this reason, recent attention has been focused

on various materials as potential alternatives to Pt, including carbon,<sup>230,231,256-258</sup> transition metal sulfides,<sup>259-263</sup> nitrides,<sup>264-268</sup> and carbides.<sup>269,270</sup>

Graphene was expected to be a promising material for DSSC counter electrodes due to its excellent conductivity that can decrease charge transfer resistance ( $R_{ct}$ ). Kaniyoor and Ramaprabhu<sup>271</sup> showed that the  $R_{ct}$  of thermally exfoliated graphene (TEG) films is  $11.7 \Omega/\text{cm}^2$ , which is very close to that of Pt electrodes ( $6.5 \Omega/\text{cm}^2$ ). So far, several groups have explored graphene-based counter electrodes, the reported efficiencies of DSSCs fabricated with graphene counter electrodes vary from 0.7 to 6.8%. Graphene films for DSSC counter electrodes have been formed by various techniques, including thermal exfoliation from graphite oxide,<sup>271</sup> the oxidative exfoliation of graphite followed by hydrazine reduction,<sup>272</sup> the chemical reduction of graphene oxide colloids under microwave irradiation<sup>273</sup> and electrophoretic deposition (EPD) followed by an annealing treatment.<sup>274,275</sup> So far, the best DSSC efficiency (6.8%) has been obtained with a graphene counter electrode. Besides, graphene-based composites including graphene/polymer, graphene/metal, and graphene/carbon nanotube, were fabricated to be counter electrodes for DSSCs.

Current research focus on flat graphene sheets, however, there is little information about 3D graphene as counter electrode in DSSCs. It was found that the defects and functional groups of the graphene sheets play a critical role in the electrocatalytic sites in DSSC counter electrodes. Raman spectra show that honeycomb-structured graphene have defect structures. Therefore, it is reasonable to hypothesize that honeycomb-structured graphene could be an efficient counter electrode material for DSSCs.



## 6.2 Experimental

### 6.2.1 Fabrication of DSSCs

3D graphene with honeycomb like structure was synthesized by the reaction of  $\text{Li}_2\text{O}$  and  $\text{CO}$ , followed by treatment of hydrochloric acid. The details were described in Chapter 5. Chemical-exfoliation graphene sheets were prepared as follows: Graphite oxide was obtained from graphite powder with modified Hummers method.<sup>74</sup> The obtained graphite oxide was dissolved in di-ionized (DI) water and exfoliated to graphene oxide by ultra-sonic treatment. Then, the graphene oxide was chemically reduced to graphene sheets by  $\text{NaBH}_4$ . The obtained graphene sheets were washed by DI water and dried.

Fluorine-doped tin oxide (FTO) glass plates were cleaned and immersed in 40 mM  $\text{TiCl}_4$  at 70 °C for 30 min.  $\text{TiO}_2$  paste (P25  $\text{TiO}_2$  in EtOH) was deposited on FTO glass to prepare a  $\text{TiO}_2$ -based photoelectrode. The photoelectrodes were heated at 325, 375, 450, and 500 °C for 5, 5, 15, and 15 min, respectively. Then the  $\text{TiO}_2$  deposition and heat-treatment processes were repeated one more time. After that, the  $\text{TiO}_2$  photoelectrodes were treated again with 40 mM  $\text{TiCl}_4$  at 70 °C for 30 min and sintered at 500 °C for 30 min. The obtained photoelectrodes were immersed in an ethanol solution of 0.3 mM N719 dye (Aldrich) for 24 h to achieve sensitization. The counter electrode was prepared by depositing graphene (HSG or CEG) on FTO glass plates. The electrolyte in the DSSCs consists of 0.025 M LiI, 0.04 M  $\text{I}_2$ , 0.28 M tert-butylpyridine (TBP), 0.05 M guanidinium thiocyanate, and 0.6 M 1-Buty-3-methylimidazolium iodide (BMII) in

acetonitrile/valeronitrile with 85/15 volume ratio. The sandwich-type DSSCs were assembled by combining the photoelectrode and the counter electrode together with the electrolyte. The active area of a fabricated DSSC was  $0.5 \times 1.0 \text{ cm}^2$ .

### 6.2.2 Characterization

**Photocurrent-voltage (I-V) measurement:** The Photocurrent–voltage measurements were performed using a Keithley Model 2400 measurement unit. The light source (AM 1.5 solar illumination,  $100 \text{ mW/cm}^2$ ) was generated by a Newport solar simulator equipped with a 1.5G air mass filter.

**Incident photon-to-current conversion efficiency (IPCE):** IPCE curves were obtained after the simulated sunlight was focused through a monochromator (Newport).



**Fig.6.2. Newport IPCE Kit.**

**Electrochemical impedance spectra (EIS):** EIS spectra of DSSCs were obtained in the dark at  $-0.7 \text{ V}$  applied bias by a CHI660 electrochemical workstation. The frequency was varied from  $0.1 \text{ Hz}$  to  $100 \text{ kHz}$  for the EIS measurements.

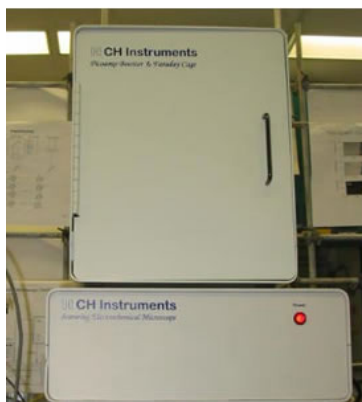


**Fig.6.3. CHI660 Electrochemical Workstation.**

**Cycle voltammetry (CV):** CV was carried out on an EG&G Princeton applied research electrochemical workstation (Model 273A). The measurement employed a three-electrode system (containing an acetonitrile solution of 0.1 M LiClO<sub>4</sub>, 10 mM LiI, and 1 mM I<sub>2</sub> at a scan rate of 20 mV/s): a Pt wire as the counter electrode, an Ag/AgCl electrode as the reference electrode, and the graphene-based electrode as the working electrode.

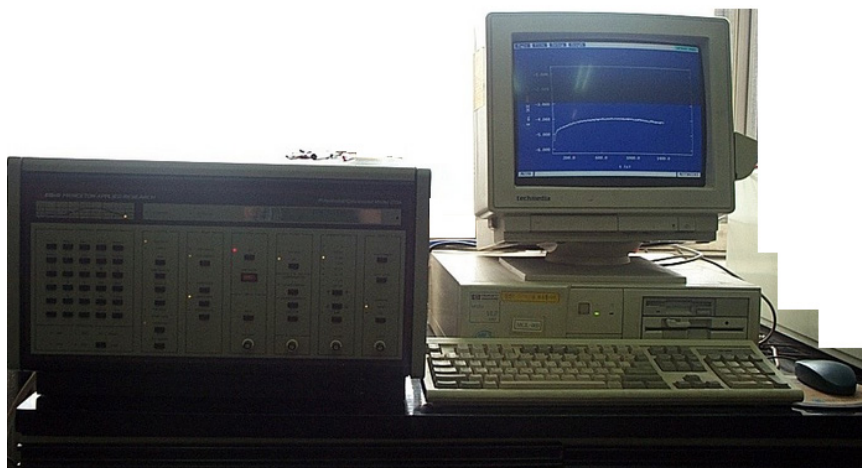


**Fig.6.4. EG&G Princeton Applied Research (Model 273A) Electrochemical Workstation.**

## 6.3 Results and Discussion

### 6.3.1 Photovoltaic performance of DSSCs with Honeycomb Structure graphene as CEs

We employed HSG without any conductive polymer as a CE for DSSCs. The photoelectrode of the DSSCs is N719 dye sensitized TiO<sub>2</sub> film on fluorine-doped tin oxide (FTO) glass plate, and the electrolyte is I<sub>3</sub><sup>-</sup>/I<sup>-</sup> based liquid. The current-voltage characteristics of the DSSCs were shown in Fig.6.5 with detail parameters summarized in Table 6.1. The DSSC with HSG-12h CE exhibited the best performance with the short-circuit current density (*I*<sub>sc</sub>) of 27.2 mA/cm<sup>2</sup>, open-circuit voltage (*V*<sub>oc</sub>) of 0.773 V, fill factor (FF) of 0.371, and power conversion efficiency ( $\eta$ ) of 7.8% under illumination of AM1.5 simulated sunlight with power density of 100 mW cm<sup>-2</sup>. This efficiency is 10 times higher than that (0.64%) of the DSSC with a CEG-based CE. Furthermore, it is even comparable to that (8%) of Pt-based DSSCs.

$$FF = \frac{P_{MAX}}{I_{SC} \times V_{OC}} \quad (1)$$

$$\eta = \frac{P_{MAX}}{E \times A} \quad (2)$$

Wheres *P*<sub>MAX</sub>: maximum power point; *V*<sub>oc</sub>: open circuit voltages; *I*<sub>sc</sub>: short circuit current; *E*: input light irradiance (W/m<sup>2</sup>); *A*: surface area of solar cell (m<sup>2</sup>).

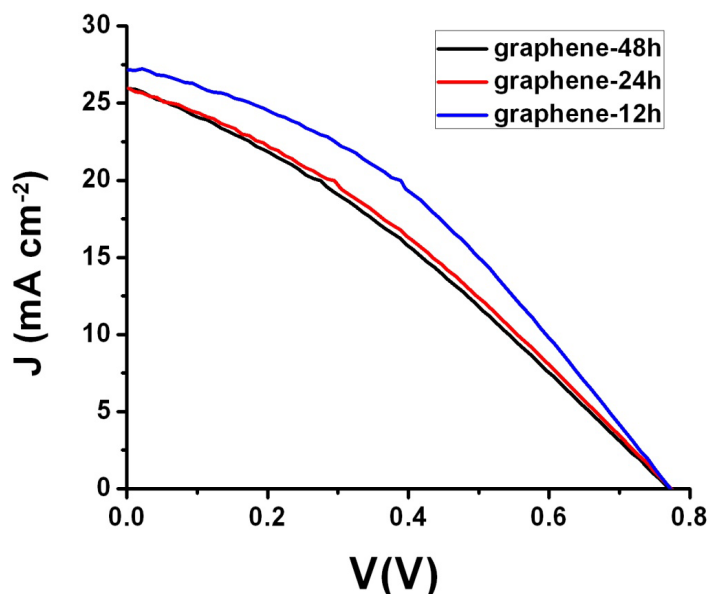


Fig.6.5. I-V curves of DSSCs with honeycomb-structured graphene as a counter electrode.

Table 6.1. The photovoltaic performance of DSSCs with honeycomb-structured graphene counter electrodes

Samples	$J_{sc}$ (mA/cm <sup>2</sup> )	$V_{oc}$ (V)	FF	$\eta$
HSG-12h	27.2	0.773	0.371	7.80%
HSG-24h	26	0.774	0.325	6.53%
HSG-48h	26	0.773	0.314	6.30%
CEG	6.48	0.785	0.127	0.64%

However, the efficiency of the HSG-based DSSC is affected by HSG synthesis time. When the synthesis time increased from 12 to 48 hours, the efficiency of the DSSC

with a HSG CE decreases from 7.8 to 6.3%. The decrease of efficiency with increasing HSG synthesis time is further supported by incident photon to charge carrier efficiency (IPCE) spectra (Fig.6.6). It is well-known that two critical factors (electrical conductivity and catalytic activity) determine CE performance for DSSCs, namely, the larger the conductivity and the catalytic activity, the higher the energy conversion efficiency is. However, when the HSG synthesis time increased from 12 to 48h, the HSG conductivity increased (which is reflected by the decrease in its sheet resistance from 3.4 to 0.45 k $\Omega$ /sq), whereas the efficiency of the HSG-based DSSC decreased. This indicates that the decrease in efficiency with increasing HSG synthesis time is not due to the variation of HSG conductivity. It has been recognized that defects of graphene sheets are active sites for the catalytic reduction of I<sub>3</sub><sup>-</sup> to I<sup>-</sup> at CE.<sup>262</sup> Furthermore, it was suggested that the defects due to nitrogen-doping could play a catalytic role.<sup>276</sup> Similarly, the existence of oxygen in HSG sheets could generate the defects as catalytic sites (Fig.5.12). The XPS results showed that the increase in HSG synthesis time reduced oxygen-containing groups, indicating the decrease of structural defects and thus the decrease of catalytic activity. Therefore, the decrease of catalytic activity with increasing HSG synthesis time would be responsible for the decrease in HSG-based DSSC efficiency.

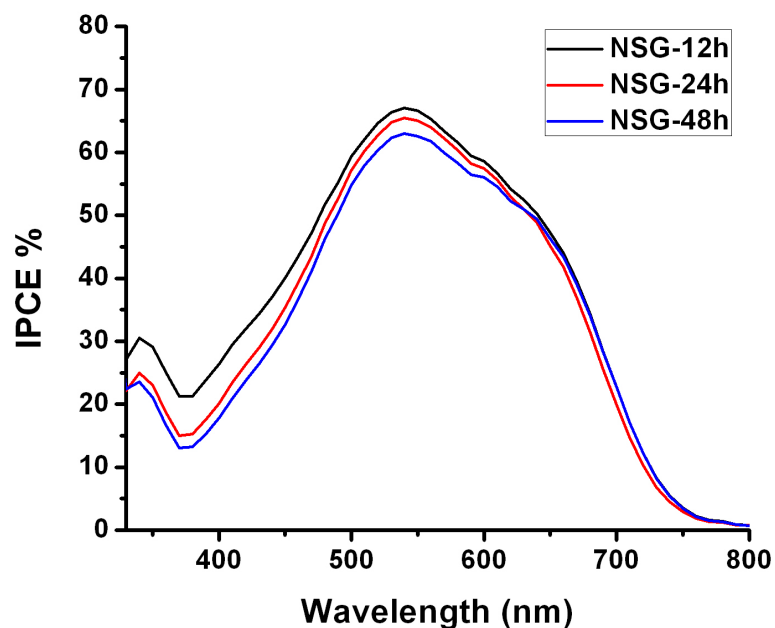


Fig.6.6. IPCE of DSSCs with honeycomb structured graphene counter electrodes.

### 6.3.2 Electrochemical characteristics of DSSCs with honeycomb structured graphene as CEs

This relationship between catalytic activity and synthesis time of HSG was further evaluated by electrochemical impedance spectroscopy (EIS). As shown in Fig.6.7, one can see Nyquist plots of DSSCs fabricated with various CEs, in which two semicircles are observed in the higher (left) and lower (right) frequency regions. The experimental EIS curves were fitted by equivalent circuit model with Z-view software (Fig.6.7) and summarized in Table 6.1. The first semicircle corresponds to charge-transfer resistance ( $R_{ct}$ ) at CE/electrolyte interface, which changes inversely with catalytic ability of CEs for the reduction of  $I_3^-$  to  $I^-$ , while the semicircle in lower frequency region is attributed to Nernst diffusion process ( $Z_N$ ).<sup>277</sup> As the three HSG counter electrodes have nearly the

same value of  $R_s$ , the effect of  $R_s$  on photovoltaic performance can be neglected. The value of  $R_{ct}$  increases in the order of HSG-12h ( $20 \Omega$ ) < HSG-24h ( $35 \Omega$ ) < HSG-48h ( $45 \Omega$ ), which is inverse to the order of electrocatalytic activity. Although HSG-12h possesses the highest intrinsic sheet resistance, it exhibits the lowest transfer resistance ( $R_{ct}$ ) at interface due to its higher catalytic activity. Furthermore, the DSSC with a CEG counter electrode has a very large transfer resistance ( $2500 \Omega$ ), indicating its very low catalytic activity and thus explains why its power conversion efficiency is negligible.

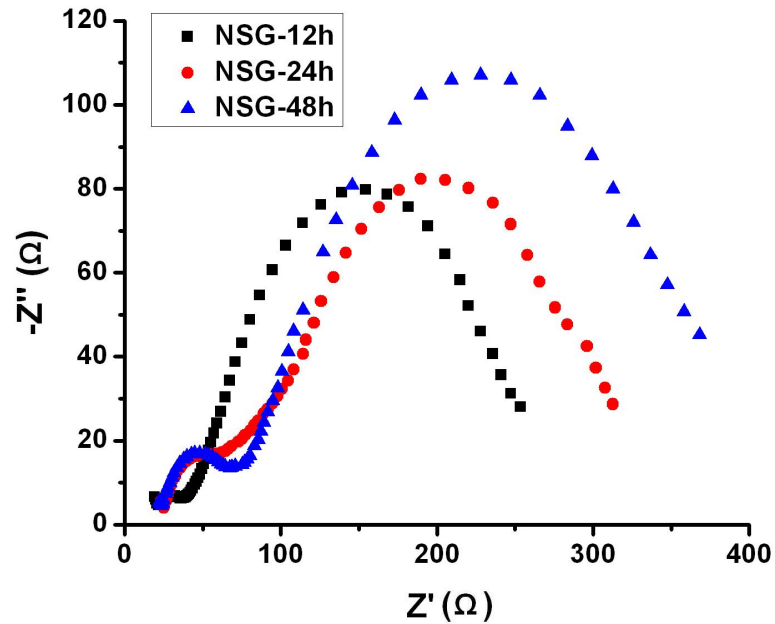


Fig.6.7. EIS of DSSCs with honeycomb structured graphene counter electrodes.



**Table 6.2. The electrochemical characteristics of DSSCs with honeycomb structured graphene counter electrodes**

Samples	$R_s$ ( $\Omega$ )	$R_{ct}$ ( $\Omega$ )	$Z_N$ ( $\Omega$ )
HSG-12h	24	20	220
HSG-24h	25	35	265
HSG-48h	24	45	310
CEG	27	2500	10000

Cyclic voltammetry (CV) curves were obtained for three HSG CEs, which show two pairs of oxidation and reduction peaks (Fig. 6.8). Since the counter electrode of a DSSC mainly catalyzes the reduction of  $I_3^-$  to  $I^-$ , which can be evaluated by the peak current density and the peak-to-peak separation ( $E_{pp}$ ) of  $A_{ox}$  and  $A_{red}$  peaks, namely, the higher the peak current density and the lower the  $E_{pp}$  value, the better the catalytic activity is.<sup>278</sup> The HSG-12 h CE showed the highest current density (1.644 mA/cm<sup>2</sup>) and the lowest  $E_{pp}$  (0.246 V) among the three electrodes, indicating its best electrocatalytic activity. This further supports the results of J-V, IPCE, and EIS measurements.

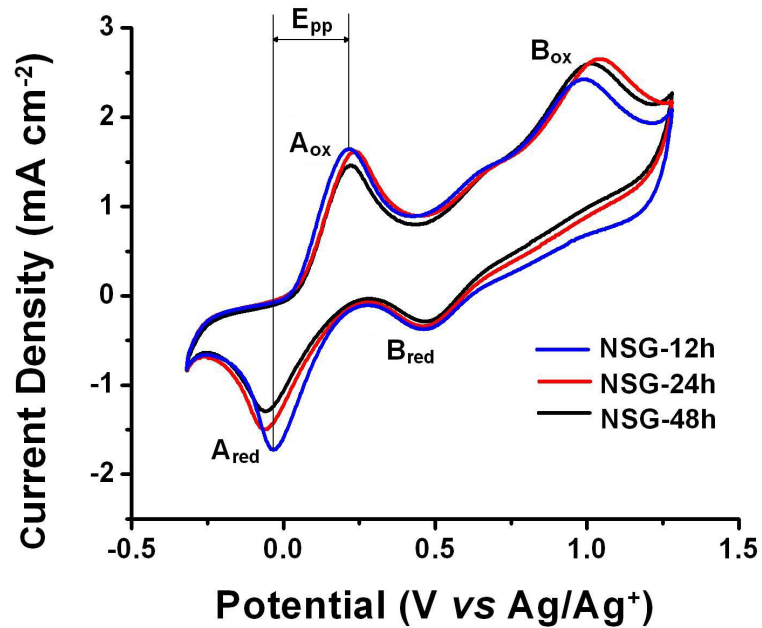


Fig.6.8. CV curves of DSSCs with honeycomb structured graphene counter electrodes

## 6.4 Conclusion

Dye-sensitized solar cells with the honeycomb structured graphene as counter electrode were successfully fabricated and measured. The DSSCs exhibited energy conversion efficiency as high as 7.8%, which is even comparable to that of DSSCs with an expensive Pt counter electrode. As increasing graphene synthesis time, the energy conversion efficiencies of DSSCs decrease due to the decrease of structural defects and thus the decrease of catalytic activity. This result is further supported by IPCE spectra. Electrochemical characteristics of DSSCs with HSG as counter electrode confirm that the catalytic activity of HSG decrease with increasing HSG synthesis time. In addition, the honeycomb structured graphene can be expected to have promising applications for energy storage devices, such as batteries and supercapacitors.

## Chapter 7 Summary

In this dissertation, graphene synthesis methods were investigated and developed. Chemical oxidation and reduction approach was used to produce graphite oxide, and graphene oxide solution. Novel graphene synthesis method was developed by the reaction between  $\text{Li}_2\text{O}$  and  $\text{CO}$ , and the resulted honey-nest-structured graphene was employed as counter electrode in DSSCs.

The effect of oxygen content on structure of graphite oxide was studied in the process of chemical oxidation and reduction method. Oxygen content of graphite oxide was tuned by changing the oxidation time via a modified Hummers approach. There are three types of functional groups in graphite oxides (epoxy, carboxyl, and hydroxyl groups), which are independent of the oxidation time. However, the content of oxygen-containing functional groups increased with increasing the oxidation time and reached a saturated level ( $\text{O/C} = 0.47$ ) in 1.5 h. Furthermore, the interplanar spaces and BET surface areas of graphite oxides linearly increased with increasing oxygen content. However, the ratio of the D band to the G band in Raman spectroscopy, which is associated with the disorder of the carbon backbone, remained unchanged with increasing oxygen content.

The stability of graphene oxide (GO) solution was evaluated. One can see that aqueous GO solution can easily be destabilized by a strong electrolyte (such as acid, base, or salt), leading to GO precipitation. Electrostatic repulsion plays the most important role in keeping the stability of the aqueous GO solutions. It was found that  $\text{HCl}$ - and  $\text{LiCl}$ -induced precipitations could not change the functional groups of GO sheets, which are

carboxyl, epoxy, and hydroxyl groups. In contrast, during the LiOH-induced GO precipitation, the carboxyl group of GO sheets disappeared with a remarkable increase in hydroxyl group and aromatic C=C bonds. This indicates that the LiOH-induced GO precipitation resulted in the partial reduction of GO sheets. Furthermore, the HCl-induced GO precipitation is a feasible approach to deposit GO sheets on a substrate as a Pt-free counter electrode for a dye-sensitized solar cell (DSSC), which exhibited 1.65% of power conversion efficiency.

Novel approach to synthesis three dimensional (3D) graphene was developed. A simple reaction between  $\text{Li}_2\text{O}$  and CO was designed to synthesize three dimensional Honeycomb-like structured graphene. The simultaneous formation of  $\text{Li}_2\text{CO}_3$  with graphene not only can isolate graphene sheets from each other to prevent graphite formation during the process, but also play a role in determining the locally curved shape of graphene sheets. 3D graphene with honeycomb structure were obtained after removing  $\text{Li}_2\text{CO}_3$ . This would be the first approach to synthesize 3D graphene sheets with a controllable shape. For the honeycomb-structured graphene, there is 94.6-97.5% carbon and 2.5-5.4% oxygen. Furthermore, these oxygen groups are heterogeneously distributed. 3D honeycomb structured graphene has excellent electrical conductivity.

Dye-sensitized solar cells with the honeycomb-structured graphene as counter electrode were successfully fabricated and measured. The DSSCs exhibited energy conversion efficiency as high as 7.8%, which is even comparable to that of DSSCs with an expensive Pt counter electrode. It indicates that 3D honeycomb-structured graphene (HSG) possesses excellent electrical conductivity and high catalytic activity, which is

confirmed by IPCE spectra, CV curves and EIS spectra. As increasing graphene synthesis time, the energy conversion efficiencies of DSSCs decrease due to the decrease of structural defects and thus the decrease of catalytic activity.

## References

- 1 C. Goh, M. D. McGehee, *The Bridge* 2005, 34, 33–39.
- 2 N. S. Lewis, *Bull MRS*, 2007, 32, 808–820.
- 3 T. W. Hamann, R. A. Jensen, A. B. F. Martinson, H. V. Ryswyk, J. T. Hupp, *Energy Environ. Sci.* 2008, 1, 66–78.
- 4 R. L. Hirsch, *Energy Policy* 2008, 36, 881–889.
- 5 G. F. Brown, J. Wu, *Laser Photonics Rev.* 2009, 3, 394–405.
- 6 L. L. Kazmerski, M. S. Ayyagari, F. R. White, G. A. Sanborn, *J. Vac. Sci. Technol.* 1976, 13, 139–144.
- 7 J. Brown, C. W. Bates, Jr., *J. Appl. Phys.* 1990, 68, 2517–2519.
- 8 K. J. Hong, T. S. Jeong, C. J. Youn, *J. Appl. Phys.* 2006, 100, 123518.
- 9 W. K. Metzger, M. Gloeckler, *J. Appl. Phys.* 2005, 98, 063701.
- 10 U. Malm and M. Edoff, *Prog. Photovoltaics* 2008, 16, 113–121.
- 11 D.M. Chapin, C.S. Fuller, G.L. Pearson, *J. Appl. Phys.* 1954, 25, 676.
- 12 A. Goetzberger, C. Hebling, H. W. Schock, *Materials Science and Engineering R* 2003, 40, 1–46
- 13 J. Dietl, D. Helmreich, E. Sirtl, *Crystals: Growth, Properties and Applications*, vol. 5, Springer, Berlin, 1981, p. 57.
- 14 R.C. Chittick, J.H. Alexander, H.F. Sterling, *J. Electrochem. Soc.* 1969, 116, 77.
- 15 D. Carlson, C. Wronski, *Appl. Phys. Lett.* 1976, 28, 671.
- 16 S. Guha, S. Yang, S. Glattfelder, Proceedings of the 2nd World Conference on Photovoltaic Solar Energy Conversion, Vienna, 1998, p. 3609.

- 17 J. Meier, P. Torres, R. Platz, S. Dubail, U. Kroll, J. Anna, N. Selvan, Pellaton, Vaucher, C. Hof, D. Fischer, H. Keppner, A. Shah, J. Koehler, *Mater. Res. Soc. Symp. Proc.* 1996, 420, 3.
- 18 D.L. Staebler, C.R. Wronski, *Appl. Phys. Lett.* 1977, 31, 292.
- 19 M.A. Contreras, B. Egaas, K. Ramanathan, J. Hiltner, A. Swartzlander, F. Hason, R. Noufi, *Prog. Photovolt.: Res.Appl.* 1999, 7, 311.
- 20 D.A. Cusano, *Solid State Electron.* 1963, 6, 217.
- 21 B. O'Regan and M. Grätzel, *Nature*, 1991, 353, 737–740.
- 22 M. Grätzel, *Inorg. Chem.*, 2005, 44, 6841–6851
- 23 (a) A. Mishra, M. K. R. Fischer and P. Bauerle, *Angew. Chem. Int. Ed.*, 2009, 48, 2474–2499; (b) Y. M. Wang, *Sol. Energy Mater. Sol. Cells*, 2009, 93, 1167–1175.
- 24 S. Yanagida, Y. H. Yu and K. Manseki, *Acc. Chem. Res.*, 2009, 42, 1827–1838.
- 25 B. O'Regan and J. R. Durrant, *Acc. Chem. Res.*, 2009, 42, 1799–1808.
- 26 G. C. Vougioukalakis, A. I. Philippopoulos, T. Stergiopoulos, *Coord. Chem. Rev.*, 2011, 255, 2602–2621.
- 27 M. Grätzel, *J. Photochem. Photobiol., C*, 2003, 4, 145–153.
- 28 Y. Chiba, A. Islam, Y. Watanabe, R. Komiya, N. Koide and L. Han, *Jpn. J. Appl. Phys.*, 2006, 45, L638–640.
- 29 Y. H. Luo, D.M.Li and Q. B. Meng, *Adv. Mater.*, 2009, 21, 4647–4651.
- 30 K. S. Novoselov, A. K. Geim, S. V. Morozov, D. Jiang, Y. Zhang, S. V. Dubonos, I. V. Gregorieva, A. A. Firsov, *Science* 2004, 306, 666–669.
- 31 P. R. Wallace, *Phys. Rev.* 1947, 71, 622–634.
- 32 J. C. Slonczewski, P. R. Weiss, *Phys. Rev.* 1958, 109, 272–279.

- 33 G. S. Painter, D. E. Ellis, *Phys. Rev. B* 1970, 1, 4747–4752.
- 34 D. P. DiVincenzo, E. J. Mele, *Phys. Rev. B* 1984, 29, 1685–1694.
- 35 G. W. Semenoff, *Phys. Rev. Lett.* 1984, 53, 2449–2452.
- 36 F. D. M. Haldane, *Phys. Rev. Lett.* 1988, 61, 2015–2018.
- 37 A. H. Castro Neto, F. Guinea, N. M. R. Peres, K. S. Novoselov, A. K. Geim, *Rev. Mod. Phys.* 2009, 81, 109–162.
- 38 L. Landau, *Phys. Z. Sowjetunion* 1937, 11, 545–549.
- 39 N. D. Mermin, H. Wagner, *Phys. Rev. Lett.* 1966, 17, 1133–1136.
- 40 N. D. Mermin, *Phys. Rev.* 1968, 176, 250–254.
- 41 K. S. Novoselov, D. Jiang, F. Schedin, T. J. Booth, V. V. Khotkevich, S. V. Morozov, A. K. Geim, *Proc. Natl. Acad. Sci. USA* 2005, 102, 10451–10453.
- 42 K. S. Novoselov, A. K. Geim, S. V. Morozov, D. Jiang, M. I. Katsnelson, I. V. Grigorieva, S. V. Dubonos, A. A. Firsov, *Nature* 2005, 438, 197–200.
- 43 (a) Y. Zhang, Y. W. Tan, H. L. Stormer, P. Kim, *Nature* 2005, 438, 201–204; (b) C. Berger, Z. Song, X. Li, X. Wu, N. Brown, C. Naud, D. Mayou, T. Li, J. Hass, A. N. Marchenkov, E. H. Conrad, P. N. First, W. A. deHeer, *Science* 2006, 312, 1191–1196.
- 44 (a) J. C. Meyer, A. K. Geim, M. I. Katsnelson, K. S. Novoselov, T. J. Booth, S. Roth, *Nature* 2007, 446, 60–63; (b) Y. Hernandez, V. Nicolosi, M. Lotya, F. M. Blighe, Z. Y. Sun, S. De, I. T. McGovern, B. Holland, M. Byrne, Y. K. Gun’ko, J. J. Boland, P. Niraj, G. Duesberg, S. Krishnamurthy, R. Goodhue, J. Hutchison, V. Scardaci, A. C. Ferrari, J. N. Coleman, *Nat. Nanotechnol.* 2008, 3, 563–568.



- 45 (a) A. K. Geim, A. H. MacDonald, *Phys. Today* 2007, 60, 35–41; (b) M. I. Katsnelson, *Mater. Today* 2007, 10, 20–27; (c) A. H. Castro Neto, F. Guinea, N. M. Peres, *Phys. World* 2006, 19, 33–37.
- 46 F. Schedin, A. K. Geim, S. V. Morozov, E. W. Hill, P. Blake, M. I. Katsnelson, K. S. Novoselov, *Nat. Mater.* 2007, 6, 652–655.
- 47 D. A. Dikin, S. Stankovich, E. J. Zimney, R. D. Piner, G. H. B. Dommett, G. Evmenenko, S. T. Nguyen, R. S. Ruoff, *Nature* 2007, 448, 457–460.
- 48 D. C. Elias, R. R. Nair, T. M. G. Mohiuddin, S. V. Morozov, P. Blake, M. P. Halsall, A. C. Ferrari, D. W. Boukhvalov, M. I. Katsnelson, A. K. Geim, K. S. Novoselov, *Science* 2009, 323, 610–613.
- 49 A. K. Geim, *Science* 2009, 324, 1530–1534.
- 50 K. S. Novoselov, Z. Jiang, Y. Zhang, S. V. Morozov, H. L. Stormer, U. Zeitler, J. C. Maan, G. S. Boebinger, P. Kim, A. K. Geim, *Science* 2007, 315, 1379.
- 51 U. Stöberl, U. Wurstbauer, W. Wegscheider, D. Weiss, *Appl. Phys. Lett.* 2008, 93, 051906.
- 52 A. Kongkanand, R. Martine-Dominguez, P. V. Kamat, *Nano Lett.* 2007, 7, 676–680.
- 53 P. Brown, K. Takeuchi, P. V. Kamat, *J. Phys. Chem. C* 2008, 112, 4776–4782.
- 54 G. Williams, B. Seger, P. V. Kamat, *ACS Nano* 2008, 2, 1487–1491.
- 55 N. Yang, J. Zhai, D. Wang, Y. Chen, L. Jiang, *ACS Nano* 2010, 4, 887–894.
- 56 A. J. van Bommel, J. E. Crombeen, A. van Tooren, *Surf. Sci.* 1975, 48, 463–467.
- 57 J. M. D. Coey, M. Venkatesan, C. B. Fitzgerald, A. P. Douvalis, I. S. Sanders, *Nature* 2002, 420, 156–159.

- 58 C. Berger, Z. M. Song, T. B. Li, X. B. Li, A. Y. Ogbazghi, R. Feng, Z. T. Dai, A. N. Marchenkov, E. H. Conrad, P. N. First, W. A. de Heer, *J. Phys. Chem. B* 2004, 108, 19912–19916.
- 59 E. Rollings, G.-H. Gweon, S. Y. Zhou, B. S. Mun, J. L. McChesney, B. S. Hussain, A. V. Fedorov, P. N. First, W. A. de Heer, A. Lanzara, *J. Phys. Chem. Solids* 2006, 67, 2172–2177.
- 60 J. Hass, R. Feng, J. E. Millán-Otoya, X. Li, M. Sprinkle, P. N. First, W. A. de Heer, E. H. Conrad, *Phys. Rev. B* 2007, 75, 214109, 1–8.
- 61 C. N. Rao, A. K. Sood, R. Voggu, K. S. Subrahmanyam, *J. Phys. Chem. Lett.* 2010, 1, 572–580.
- 62 A. N. Obraztsov, E. A. Obraztsova, A. V. Tyurnina, A. A. Zolotukhin, *Carbon* 2007, 45, 2017–2021.
- 63 H. Ueta, M. Saida, C. Nakai, Y. Yamada, M. Sasaki, S. Yamamoto, *Surf. Sci.* 2004, 560, 183–190.
- 64 J. Coraux, A. T. Ndiaye, C. Busse, T. Michely, *Nano Lett.* 2008, 8, 565–570.
- 65 A. L. Vázquez de Parga, F. Calleja, B. Borca, M. C. G. Passeggi, Jr., J. J. Hinarejos, F. Guinea, R. Miranda, *Phys. Rev. Lett.* 2008, 100, 056807–056810.
- 66 A. G. Starodubov, M. A. Medvetskii, A. M. Shikin, V. K. Adamchuk, *Phys. Solid State* 2004, 46, 1340–1348.
- 67 K. S. Kim, Y. Zhao, H. Jang, S. Y. Lee, J. M. Kim, K. S. Kim, J. H. Ahn, P. Kim, J. Y. Choi, B. H. Hong, *Nature* 2009, 457, 706–711.
- 68 A. Reina, X. Jia, J. Ho, D. Nezich, H. Son, V. Bulovic, M. S. Dresselhaus, J. Kong, *Nano Lett.* 2009, 9, 30–35.

- 69 X. Li, W. Cai, J. An, S. Kim, J. Nah, D. Yang, R. Piner, A. Valamakkan, I. Jung, E. Tutuc, S. K. Baerjee, L. Colombo, R. S. Ruoff, *Science* 2009, 324, 1312–1314.
- 70 Y. Wang, X. H. Chen, Y. L. Zhong, F. R. Zhu, K. P. Loh, *Appl. Phys. Lett.* 2009, 95, 063302–063303.
- 71 V. C. Tung, M. J. Allen, Y. Yang, R. B. Kaner, *Nat. Nanotechnol.* 2009, 4, 25–28.
- 72 D. R. Dreyer, S. Park, C. W. Bielawski, R. S. Ruoff, *Chem. Soc. Rev.* 2010, 39, 228–240.
- 73 B. C. Brodie, *Philos. Trans. R. Soc. London* 1859, 149, 249–259.
- 74 W. S. Hummers, R. E. Offeman, *J. Am. Chem. Soc.* 1958, 80, 1339.
- 75 C. N. R. Rao, A. K. Sood, K. S. Subrahmanyam, A. Govindaraj, *Angew. Chem. Int. Ed.* 2009, 48, 7752–7777.
- 76 (a) S. Stankovich, D. A. Dikin, G. B. Dommett, K. M. Kohlhaas, E. J. Zimney, E. A. Stach, R. D. Piner, S. T. Nguyen, R. S. Ruoff, *Nature* 2006, 442, 282–286; (b) S. Stankovich, D. A. Dikin, R. D. Piner, K. A. Kohlhaas, A. Kleinhammes, Y. Jia, Y. Wu, S. T. Nguyen, R. S. Ruoff, *Carbon* 2007, 45, 1558–1565; (c) D. Li, M. B. Muller, S. Gilje, R. B. Kaner, G. Wallace, *Nat. Nanotechnol.* 2008, 3, 101–105.
- 77 G. Eda, G. Fanchini, M. Chhowalla, *Nat. Nanotechnol.* 2008, 3, 270–274.
- 78 H. A. Becerril, J. Mao, Z. Liu, R. M. Stoltenberg, Z. Bao, Y. Chen, *ACS Nano* 2008, 2, 463–470.
- 79 H. C. Schniepp, J. L. Li, M. J. McAllister, H. Sai, M. Herrera-Alonso, D. H. Adamson, R. K. Prud'homme, R. Car, D. A. Saville, I. A. Aksay, *J. Phys. Chem. B* 2006, 110, 8535–8539.

- 80 C. Gómez-Navarro, R. T. Weitz, A. M. Bittner, M. Scolari, A. Mews, M. Burghard, K. Kern, *Nano Lett.* 2007, 7, 3499–3503.
- 81 X. Wang, L. J. Zhi, K. Mullen, *Nano Lett.* 2008, 8, 323–327.
- 82 R. S. Sundaram, C. Gomez-Navarro, K. Balasubramanian, M. Burghard, K. Kern, *Adv. Mater.* 2008, 20, 3050–3053.
- 83 M. Zhou, Y. Wang, Y. Zhai, J. Zhai, W. Ren, F. Wang, S. Dong, *Chem. Eur. J.* 2009, 15, 6116–6120.
- 84 L. J. Cote, R. Cruz-Silva, J. Huang, *J. Am. Chem. Soc.* 2009, 131, 11027–11032.
- 85 X. Du, I. Skachko, A. Barker, E. Y. Andrei, *Nat. Nanotechnol.* 2008, 3, 491–495.
- 86 M. Dragoman, D. Dragoman, *Prog. Quantum Electron.* 2009, 33, 165–214.
- 87 Y.-W. Tan, Y. Zhang, H. L. Stormer, P. Kim, *Eur. Phys. J. Special Topics* 2007, 148, 15–18.
- 88 A. C. Ferrari, J. C. Meyer, V. Scardaci, C. Casiraghi, M. Lazzeri, F. Mauri, S. Piscanec, D. Jiang, K. S. Novoselov, S. Roth, A. K. Geim, *Phys. Rev. Lett.* 2006, 97, 187401–187404.
- 89 J. Yan, Y. Zhang, P. Kim, A. Pinczuk, *Phys. Rev. Lett.* 2007, 98, 166802–166804.
- 90 Z. Jiang, E. A. Henriksen, L.C. Tung, Y. J. Wang, M. E. Schwartz, M. Y. Han, P. Kim, H. L. Stormer, *Phys. Rev. Lett.* 2007, 98, 197403–197404.
- 91 C. Casiraghi, A. Hartschuh, E. Lidorikis, H. Qian, H. Harutyunyan, T. Gokus, K. S. Novoselov, A. C. Ferrari, *Nano Lett.* 2007, 7, 2711–2717.
- 92 D. E. Sheehy, J. Schmalian, *Phys. Rev. B* 2009, 80, 193411–193414.
- 93 L. Hao, L. Sheng, *Solid State Commun.* 2009, 149, 1962–1966.
- 94 E. G. Mishchenko, *Phys. Rev. Lett.* 2009, 103, 246802–246804.

- 95 F. N. Xia, T Mueller, YM Lin, A Valdes-Garcia, P Avouris, *Nat. Nanotechnol.* 2009, 4, 839–843.
- 96 F. Wang, Y. Zhang, C. Tian, C. Girit, A. Zettl, M. Crommie, Y. R. Shen, *Science* 2008, 320, 206–209.
- 97 T. Stauber, N. M. R. Peres, A. K. Geim, *Phys. Rev. B* 2008, 78, 085432–085438.
- 98 A. B. Kuzmenko, L. Benfatto, E. Cappelluti, I. Crassee, D. van der Marel, P. Blake, K. S. Novoselov, A. K. Geim, *Phys. Rev. Lett.* 2009, 103, 116804–116812.
- 99 R. R. Nair, P. Blake, A. N. Grigorenko, K. S. Novoselov, T. J. Booth, T. Stauber, N. M. R. Peres, A. K. Geim, *Science* 2008, 320, 1308
- 100A. W. W. Ludwig, M. P. A. Fisher, R. Shankar, G. Grinstein, *Phys. Rev. B* 1994, 50, 7526–7552.
- 101M. H. Liang, B. Luo, L. J. Zhi, *Inter. J. Energy Res.* 2009, 33, 1161–1170.
- 102 X. Wang, L. Zhi, N. Tsao, Z. Tomović, J. Li, K. Müllen, *Angew. Chem.* 2008, 120, 3032–3034; *Angew. Chem. Int. Ed.* 2008, 47, 2990–2992.
- 103L. Hu, D. S. Hecht, G. Gruner, *Nano Lett.* 2004, 4, 2513–2517.
- 104 Z. C. Wu, Z. H. Chen, X. Du, J. M. Logan, J. Sippel, M. Nikolou, K. Kamaras, J. R. Reynolds, D. B. Tanner, A. F. Hebard, A. G. Rinzler, *Science* 2004, 305, 1273–1276.
- 105 M. Rowell, M. A. Topinka, M. McGehee, H. Prall, G. Dennler, N. Sariciftci, L. Hu, G. Gruner, *Appl. Phys. Lett.* 2006, 86, 233506.
- 106 S. Barazzouk, S. Hotchandani, K. Vinodgopal, P. V. Kamat, *J. Phys. Chem. B* 2004, 108, 17015–17018.

- 107 J. B. Wu, H. A. Becerril, Z. N. Bao, Y. S. Chen, P. Peumans, *Appl. Phys. Lett.* 2008, 92, 263302.
- 108 Y. Y. Liang, J. Frisch, L. J. Zhi, H. Norouzi-Arasi, X. L. Feng, J. P. Rabe, N. Koch, K. Müllen, *Nanotechnology* 2009, 20, 434007.
- 109 I. Jung, D. A. Dikin, R. D. Piner, R. S. Ruoff, *Nano Lett.* 2008, 8, 4283–4387.
- 110 S. D. Wu, L. J. Jing, Q. X. Li, Q. W. Shi, J. Chen, H. B. Su, X. P. Wang, J. L. Yang, *Phys. Rev. B* 2008, 77, 195411.
- 111 L. Zhao, L. Zhao, Y. X. Xu, L. J. Zhi, G. Q. Shi, *Electrochim. Acta* 2009, 55, 491–497.
- 112 R. D. Rauh, *Electrochim. Acta* 1999, 44, 3165–3176.
- 113 V. C. Tung, L. M. Chen, M. J. Allen, J. K. Wassei, K. Nelson, R. B. Kaner, Y. Yang, *Nano Lett.* 2009, 9, 1949–1955.
- 114 B. B. Parekh, G. Fanchini, G. Eda, M. Chhowalla, *Appl. Phys. Lett.* 2007, 90, 121913, 1–3.
- 115 G. Eda, Y.-Y. Lin, S. Miller, C.-W. Chen, W-F. Su, M. Chhowalla, *Appl. Phys. Lett.* 2008, 93, 233502, 1–3.
- 116 F. Padinger, R. Rittberger, N. S. Sariciftci, *Adv. Funct. Mater.* 2003, 13, 85–88.
- 117 C. W. Tang, *Appl. Phys. Lett.* 1986, 48, 183–185.
- 118 G. Yu, J. Gao, J. C. Hummelen, F. Wudl, A. J. Heeger, *Science* 1995, 270, 1789–1791.
- 119 J. M. Halls, C. A. Walsh, N. C. Greenham, E. A. Marseglia, R. H. Friend, S. C. Moratti, A. B. Holmes, *Nature* 1995, 376, 498–500.

- 120 A. C. Mayer, S. R. Scully, B. E. Hardin, M. W. Rower, M. D. McGehee, *Mater. Today* 2007, 10, 28–33.
- 121 N. Li, S. R. Forrest, *Appl. Phys. Lett.* 2009, 95, 123309.
- 122 D. Veldman, T. Offermans, J. Sweelssen, M. M. Koetse, S. C. J. Meskers, R. A. Janssen, *Thin Solid Films* 2006, 511/512, 333–337.
- 123 M. M. Alam, S. A. Jenekhe, *Chem. Mater.* 2004, 16, 4647–4656.
- 124 T. Kietzke, H. H. Horhold, D. Neher, *Chem. Mater.* 2005, 17, 6532–6537.
- 125 M. M. Koetse, J. Sweelssen, K. T. Hoekerd, H. M. Schoo, S. C. Veenstra, J. M. Kroon, X. Yang, J. Loos, *Appl. Phys. Lett.* 2006, 88, 083504, 1–3.
- 126 J. J. Dittmer, K. Petritsch, E. A. Marseglia, R. H. Friend, H. Rost, A. B. Holmes, *Synth. Met.* 1999, 102, 879–880.
- 127 J. J. Dittmer, R. Lazzaroni, P. Leclere, P. Moretti, M. Granstrom, K. Petritsch, E. A. Marseglia, R. H. Friend, J. L. Bredas, H. Rost, A. B. Holmes, *Sol. Energy Mater. Sol. Cells* 2000, 61, 53–61.
- 128 J. J. Dittmer, E. A. Marseglia, R. H. Friend, *Adv. Mater.* 2000, 12, 1270–1274.
- 129 F. Yang, M. Shtein, S. R. Forrest, *Nat. Mater.* 2005, 4, 37–41.
- 130 P. Peumans, S. Uchida, S. R. Forrest, *Nature* 2003, 425, 158–162.
- 131 L. Schmidt-Mende, A. Fechtenkötter, K. Mullen, E. Moons, R. H. Friend, J. D. MacKenzie, *Science* 2001, 293, 1119–1122.
- 132 J. Peet, J. Y. Kim, N. E. Coates, W. L. Ma, D. Moses, A. J. Heeger, G. C. Bazan, *Nat. Mater.* 2007, 6, 497–500.
- 133 A. J. Moul, K. Meerholz, *Adv. Mater.* 2008, 20, 240–245.

- 134 G. Li, V. Shrotriya, J. S. Huang, Y. Yao, T. Moriarty, K. Emery, Y. Yang, *Nat. Mater.* 2005, 4, 864–868.
- 135 W. L. Ma, C. Y. Yang, X. Gong, K. Lee, A. J. Heeger, *Adv. Funct. Mater.* 2005, 15, 1617–1622.
- 136 K. Kim, J. Liu, M. A. G. Namboothiry, D. L. Carroll, *Appl. Phys. Lett.* 2007, 90, 163511.
- 137 J. Y. Kim, K. Lee, N. E. Coates, D. Moses, T. Q. Nguyen, M. Dante, A. J. Heeger, *Science* 2007, 317, 222–225.
- 138 B. J. Landi, R. P. Raffaele, S. L. Castro, S. G. Bailey, *Prog. Photovoltaics* 2005, 13, 165–172.
- 139 E. Kymakis, E. Koudoumas, I. Franghiadakis, G. A. J. Amaratunga, *J. Phys. D* 2006, 39, 1058–1062.
- 140 E. Kymakis, I. Alexandrou, G. A. J. Amaratunga, *J. Appl. Phys.* 2003, 93, 1764–1768.
- 141 J. X. Geng, T. Y. Zeng, *J. Am. Chem. Soc.* 2006, 128, 16827–16833.
- 142 E. Kymakis, G. A. J. Amaratunga, *Appl. Phys. Lett.* 2002, 80, 112–116.
- 143 Q. Liu, Z. F. Liu, X. Y. Zhang, L. Y. Yang, N. Zhang, G. L. Pan, S. G. Yin, Y. Chen, J. Wei, *Adv. Funct. Mater.* 2009, 19, 894–904.
- 144 Z. F. Liu, Q. Liu, Y. Huang, Y. F. Ma, S. G. Yin, X. Y. Zhang, W. Sun, Y. S. Chen, *Adv. Mater.* 2008, 20, 3924–3930.
- 145 G. Williams, P. V. Kamat, *Langmuir* 2009, 25, 13869–13873.
- 146 O. Akhavan, E. Ghaderi, *J. Phys. Chem. C* 2009, 113, 20214–20220.
- 147 O. Akhavan, *J. Colloid Interface Sci.* 2009, 336, 117–124.



- 148 T. Sato, M. Taya, *Biochem. Eng. J.* 2006, 30, 199–204.
- 149 Y.-L. Kuo, H.-W. Chen, Y. Ku, *Thin Solid Films* 2007, 515, 3461–3468.
- 150 V. Vamathevan, R. Amal, D. Beydoun, G. Low, S. McEvoy, *J. Photochem. Photobiol. A* 2002, 148, 233–245.
- 151 T. Murakata, Y. Higashi, N. Yasui, T. Higuchi, S. Sato, *J. Chem. Eng. Jpn.* 2002, 35, 1270–1276.
- 152 A. Vollmer, X. L. Feng, X. Wang, L. J. Zhi, K. M\_llen, N. Koch, J. P. Rabe, *Applied Physics A* 2009, 94, 1–4.
- 153 K. Kalyanasundaram, M. Grätzel, *Coord. Chem. Rev.* 1998, 177, 347–414.
- 154 M. Grätzel, *J. Photochem. Photobiol. A* 2004, 164, 3–14.
- 155 P. Varshney, M. Deepa, N. Sharma, S. Agnihotry, *Solid State Ionics* 2002, 877, 152–153.
- 156 S. Y. Chae, M. K. Park, S. K. Lee, T. Y. Kim, S. K. Kim, W. I. Lee, *Chem. Mater.* 2003, 15, 3326–3331.
- 157 S. R. Kim, M. K. Parvez, M. Chhowalla, *Chem. Phys. Lett.* 2009, 483, 124–127.
- 158 S. Sun, L. Gao, Y. Liu, *Appl. Phys. Lett.* 2010, 96, 083113.
- 159 (a) B. O'Regan, M. Grätzel, *Nature* 1991, 353, 737–740; (b) N. Papageorgiou, *Coord. Chem. Rev.* 2004, 248, 1421–1423.
- 160 Y. Xu, H. Bai, G. Lu, C. Li, G. Shi, *J. Am. Chem. Soc.* 2008, 130, 5856–5857.
- 161 X. Crispin, F. L. E. Jakobsson, A. Crispin, P. C. M. Grim, P. Andersson, A. Volodin, C. van Haesendonck, M. Van der Auweraer, W. R. Salaneck, M. Berggren, *Chem. Mater.* 2006, 18, 4354–4360.

- 162 B. L. Groenendaal, F. Jonas, D. Freitag, H. Pielartzik, J. Reynolds, *Adv. Mater.* 2000, 12, 481–494.
- 163 W. J. Hong, Y. X. Xu, G. W. Lu, C. Li, G. Q. Shi, *Electrochem. Commun.* 2008, 10, 1555–1558.
- 164 (a) S. Park, R. S. Ruoff, *Nat. Nanotechnol.* 2009, 4, 217–224. (b) S. Park, D. A. Dikin, S. T. Nguyen, R. S. Ruoff, *J. Phys. Chem. C* 2009, 113, 15801–15804.
- 165 M. Feng, R. Sun, H. Zhan, Y. Chen, *Nanotechnology* 2010, 21, 075601.
- 166 G. Eda, M. Chhowalla, *Adv. Mater.* 2010, 22, 2392–2415.
- 167 J. Kim, L. J. Cote, F. Kim, W. Yuan, R. Shull Kenneth, J. X. Huang, Graphene Oxide Sheets at Interfaces. *J. Am. Chem. Soc.* 2010, 132, 8180–8186.
- 168 S. Pang, H. N. Tsao, X. Feng, K. Müllen, *Adv. Mater.* 2009, 21, 3488–3493.
- 169 F. Grieser, M. Ashokkumar, in: *Colloids and Colloid Assemblies*, F. Caruso (Ed.) First ed., Wiley-VCH:Weinheim, 2004.
- 170 (a) K.L. Chen, M. Elimelech, *Langmuir* 2006, 22, 10994; (b) K.L. Chen, S.E. Mylon, M. Elimelech, *Environ. Sci. Technol.* 2006, 40, 1516.
- 171 N. Papageorgiou, W. F. Maiera and M. Grätzel, *J. Electrochem. Soc.* 1997, 144, 876.
- 172 S. S. Kim, Y. C. Nah, Y. Y. Noh, J. Jo and D. Y. Kim, *Electrochim. Acta*, 2006, 51, 3814–3819.
- 173 X. Fang, T. Ma, G. Guan, M. Akiyama, T. Kida and E. Abe, *J. Electroanal. Chem.*, 2004, 570, 257–263.
- 174 (a) E. Olsen, G. Hagen and S. E. Lindquist, *Sol. Energy Mater. Sol. Cells*, 2000, 63, 267–273; (b) F. Jaouen, E. Proietti, M. Lefevre, R. Chenitz, J. P. Dodelet, G.

- Wu, H. T. Chung, C. M. Johnston and P. Zelenay, *Energy Environ. Sci.*, 2011, 4, 114–130.
- 175 K. S. Kim, Y. Zhao, H. Jang, S. Y. Lee, J. M. Kim, K. S. Kim, J. H. Ahn, P. Kim, J. Y. Choi, B. H. Hong, *Nature* 2009, 457, 706–710.
- 176 D. R. Dreyer, S. Park, C. W. Bielawski, R. S. Ruoff, *Chem. Soc. Rev.* 2010, 39, 228–240.
- 177 L. Ber. Deut. Staudenmaier, *Chem. Ges.* 1898, 31, 1481–1499.
- 178 H. He, T. Riedl, A. Lerf, J. Klinowski, *J. Phys. Chem.* 1996, 100, 19954–19958.
- 179 A. Lerf, H. He, M. Forster, J. Klinowski, *J. Phys. Chem.* 1998, 102, 4477–4482.
- 180 L. B. Casabianca, M. A. Shaibat, W. W. Cai, S. Park, R. Piner, R. S. Ruoff, Y. Ishii, *J. Am. Chem. Soc.* 2010, 132, 5672–5676.
- 181 L. J. Cote, F. Kim, J. X. Huang, *J. Am. Chem. Soc.* 2009, 131, 1043–1049.
- 182 S. Brunauer, P. H. Emmett, E. Teller, *J. Am. Chem. Soc.* 1938, 60, 309–319.
- 183 J. I. Paredes, S. Villar-Rodil, A. Martínez-Alonso, J. M. D. Tascon, *Langmuir* 2008, 24, 10560–10564.
- 184 Y. X. Xu, H. Bai, G. W. Lu, C. Li, G. Q. Shi, *J. Am. Chem. Soc.* 2008, 130, 5856–5857.
- 185 Q. Yang, X. J. Pan, F. Huang, K. Li, *J. Phys. Chem. C* 2010, 114, 3811–3816.
- 186 Y. Si, E. T. Samulski, *Nano Lett.* 2008, 8, 1679–1682
- 187 Y. W. Zhu, M. D. Stoller, W. W. Cai, A. Velamakanni, R. D. Piner, D. Chen, Ruoff, R. S. *ACS Nano* 2010, 4, 1227–1233.
- 188 F. A. d. I. Cruz, J. M. Cowley, *Nature* 1962, 196, 468–469; F. A. d. I. Cruz, J. M. Cowley, *Acta Crystallogr.* 1963, 16, 531–534.

- 189 H. K. Jeong, Y. P. Lee, R. J. Lahaye, M. H. Park, K. H. An, I. J. Kim, C. W. Yang, C. Y. Park, R. S. Ruoff, Y. H. Lee, *J. Am. Chem. Soc.* 2008, 130, 1362.
- 190 T. Szabó, O. Berkesi, P. Forgó, K. Josepovits, Y. Sanakis, D. Petridis, I. Dékány, *Chem. Mater.* 2006, 18, 2740–2749.
- 191 D. W. Boukhvalov, M. I. Katsnelson, *J. Am. Chem. Soc.* 2008, 130, 10697–10701.
- 192 A. Peigney, C. Laurent, E. Flahaut, R. R. Bacsa, A. Rousset, *Carbon* 2001, 39, 507–514.
- 193 K. N. Kudin, B. Ozbas, H. C. Schniepp, R. K. Prudhomme, I. A. Aksay, R. Car, *Nano Lett.* 2008, 8, 36–41.
- 194 M. Baraket, S. G. Walton, E. H. Lock, J. T. Robinson, F. K. Perkins, *Appl. Phys. Lett.* 2010, 96, 231501.
- 195 D. X. Yang, A. Velamakanni, G. Bozoklu, S. Park, M. Stoller, R. D. Piner, S. Stankovich, I. Jung, D. A. Field, C. A. Jr. Ventrice, R. S. Ruoff, *Carbon* 2009, 47, 145–152.
- 196 A. Das, B. Chakraborty, A. K. Sood, *Bull. Mater. Sci.* 2008, 31, 579–584.
- 197 A.K. Geim, K.S. Novoselov, *Nat. Mater.* 2007, 6, 183.
- 198 S.K. Park, Y. Shao, H. Wan, P.C. Rieke, V.V. Viswanathan, S.A. Towne, L.V. Saraf, J. Liu, Y. Lin, Y. Wang, *Electrochem. Commun.* 2011, 13, 258.
- 199 (a) S. Stankovich, R.D. Piner, X. Chen, N. Wu, S.T. Nguyen, R.S. Ruoff, *J. Mater.Chem.* 2006, 16, 155; (b) S. Stankovich, R.D. Piner, S.T. Nguyen, R.S. Ruoff, *Carbon* 2006, 44, 3342.

- 200 (a) M.J. Allen, V.C. Tung, R.B. Kaner, *Chem. Rev.* 2010, 110, 132; (b) C.N.R. Rao, K. Biswas, K.S. Subrahmanyam, A.J. Govindaraj, *Mater. Chem.* 2009, 19, 2457; Y.W. Zhu, S. Murali, W.W. Cai, X.S. Li, J.W. Suk, J.R. Potts, R.S. Ruoff, *Adv. Mater.* 2010, 22, 3906.
- 201 S. Gilje, S. Han, M.S. Wang, K.L. Wang, R.B. Kaner, *Nano Lett.* 2007, 7, 3394.
- 202 S. Wang, P.K. Ang, Z.Q. Wang, A.L.L. Tang, J.T.L. Thong, K.P. Loh, *Nano Lett.* 2010, 10, 92.
- 203 J.T. Robinson, F.K. Perkins, E.S. Snow, Z.Q. Wei, P.E. Sheehan, *Nano Lett.* 2008, 8, 3137.
- 204 J.D. Fowler, M.J. Allen, V.C. Tung, Y. Yang, R.B. Kaner, B.H. Weiller, *ACS Nano* 2009, 3, 301.
- 205 D. Joung, A. Chunder, L. Zhai, S.I. Khondaker, *Nanotechnology* 2010, 21, 165202.
- 206 S. Watcharotone, D. A. Dikin, S. Stankovich, R. Piner, I. Jung, G. H. B. Dommett, G. Evmenenko, S. E. Wu, S. F. Chen, C. P. Liu, S. T. Nguyen, R. S. Ruoff, *Nano Lett.* 2007, 7, 1888.
- 207 D. Li, R.B. Kaner, *Science* 2008, 320, 1170.
- 208 D.H. Wang, D.W. Choi, J. Li, Z.G. Yang, Z.M. Nie, R. Kou, D.H. Hu, C.M. Wang, L.V. Saraf, J.G. Zhang, I.A. Aksay, J. Liu, *ACS Nano* 2009, 3, 907.
- 209 H. Kim, A.A. Abdala, C.W. Macosko, *Macromolecular* 2010, 43, 6515.
- 210 D. Li, M.B. Müller, S. Gilje, R.B. Kaner, G.G. Wallace, *Nat. Nanotechnol.* 2008, 3, 101.

- 211 (a) R.J. Hunter, *Foundations of Colloid Science*, second ed., Oxford University Press, Oxford; New York, 2001; (b) J. Israelachvili, *Intermolecular and Surface Forces*, Academic Press, New York, 1991; (c) S.A. Hasan, J.L. Rigueur, R.R. Harl, A.J. Krejci, I. Gonzalo-Juan, B.R. Rogers, J.H. Dickerson, *ACS Nano* 2010, 4, 7367; (d) M. Lotya, Y. Hernandez, P.J. King, R.J. Smith, V. Nicolosi, L.S. Karlsson, F.M. Blighe, S. De, Z. Wang, I.T. McGovern, G.S. Duesberg, J.N. Coleman, *J. Am. Chem. Soc.* 2009, 131, 3611.
- 212 F. Yang, Y.Q. Liu, L. Gao, J. Sun, *J. Phys. Chem. C* 2010, 114, 22085.
- 213 J. I. Paredes, S. Villar-Rodil, A. Martínez-Alonso, J. M. D. Tascón, *Langmuir* 2008, 24, 10560.
- 214 J. N. Israelachvili, *Intermolecular and Surface Forces*, Academic Press, San Diego, 1992. p. 450.
- 215 X. Fan, W. Peng, Y. Li, X. Li, S. Wang, G. Zhang, F. Zhang, *Adv. Mater.* 2008, 20, 4490.
- 216 J. P. Rourke, P. A. Pandey, J. J. Moore, M. Bates, I. A. Kinloch, R. J. Young, N. R. Wilson, *Angew. Chem. Int. Ed.* 2011, 50, 3173.
- 217 D.J. Muller, A. Engel, *Biophys. J.* 1997, 73, 1633.
- 218 E.J. Wanless, W.A. Ducker, *J. Phys. Chem.* 1996, 100, 3207.
- 219 M. Colic, M.L. Fisher, *Chem. Phys. Lett.* 1998, 291, 24.
- 220 (a) V. Bergeron, *Langmuir* 1996, 12, 5751; (b) S. McLaughlin, *Annu. Rev. Biophys. Biophys. Chem.* 1989, 18, 113.
- 221 G.X. Wang, B. Wang, J. Park, J. Yang, X.P. Shen, J. Yao, *Carbon* 2009, 47, 68.

- 222 J.F. Shen, Y.Z. Hu, M. Shi, X. Lu, C. Qin, C. Li, M.X. Ye, *Chem. Mater.* 2009, 21, 3514.
- 223 G. Wang, X. Shen, B. Wang, J. Yao, J. Park, *Carbon* 2009, 47, 2049.
- 224 Z. Ni, Y. Wang, T. Yu, Z. Shen, *Nano Res.* 2008, 1, 273.
- 225 S. Stankovich, D.A. Dikin, R.D. Piner, K.A. Kohlhaas, A. Kleinhammes, Y. Jia, Y. Wu, S.T. Nguyen, R.S. Ruoff, *Carbon* 2007, 45, 1558.
- 226 P.G. Ren, D.X. Yan, X. Ji, T. Chen, Z.-M. Li, *Nanotechnol* 2011, 22, 055705.
- 227 J. Shen, M. Shi, N. Li, B. Yan, H. Ma, Y. Hu, M. Ye, *Nano Res.* 2010, 3, 339.
- 228 O.C. Compton, B. Jain, D.A. Dikin, A. Abouimrane, K. Amine, S.T. Nguyen, *ACS Nano* 2011, 5, 4380.
- 229 M.J. Fernández-Merino, L. Guardia, J.I. Paredes, S. Villar-Rodil, P. Solís-Fernández, A. Martínez-Alonso, J.M.D. Tascón, *J. Phys. Chem. C* 2010, 114, 6426.
- 230 A. Kay, M. Grätzel, *Sol. Energy Mater. Sol. Cells* 1996, 44, 99–117.
- 231 T. Hino, Y. Ogawa and N. Kuramoto, *Carbon* 2006, 44, 880–887.
- 232 C. Lee, X. Wei, J. W. Kysar, J. Home, *Science* 2008, 321, 385–388.
- 233 P. Sutter, *Nat. Mater.* 2009, 8, 171–172.
- 234 L. Ci, L. Song, D. Jariwala, A. Laura Elías, W. Gao, M. Terrones, P. M. Ajayan, *Adv. Mater.* 2009, 21, 4487–4491.
- 235 B. Wu, D. Geng, Y. Guo, L. Huang, Y. Xue, J. Zheng, J. Chen, G. Yu, Y. Liu, L. Jiang, W. Hu, *Adv. Mater.* 2011, 23, 3522–3525.
- 236 Z. Yan, J. Lin, Z. Peng, Z. Sun, Y. Zhu, L. Li, C. Xiang, E. L. Samuel, C. Kittrell, J. M. Tour, *ACS Nano* 2012, 6, 9110–9117.

- 237 Z. Chen, W. Ren, L. Gao, B. Liu, S. Pei, H.-M. Cheng, *Nat. Mater.* 2011, 10, 424–428.
- 238 Y. Zhu, S. Murali, M. D. Stoller, K. J. Ganesh, W. Cai, P. Ferreira, A. Pirkle, R. M. Wallace, K. A. Cychosz, M. Thommes, D. Su, E. A. Stach, R. S. Ruoff, *Science* 2011, 332, 1537–1541.
- 239 Z.S. Wu, Y. Sun, Y. Z. Tan, S. Yang, X. Feng, K. Müllen, *J. Am. Chem. Soc.* 2012, 134, 19532–19535.
- 240 Z.S. Wu, S. Yang, Y. Sun, K. Parvez, X. Feng, K. Müllen, *J. Am. Chem. Soc.* 2012, 134, 9082–9085.
- 241 Z.S. Wu, A. Winter, L. Chen, Y. Sun, A. Turchanin, X.L. Feng, K. Müllen, *Adv. Mater.* 2012, 24, 5130–5135.
- 242 W.J. Yu, S.H. Chae, D.P., S.Y. Lee, G.H. Han, Y.H. Lee, *ACS Nano* 2010, 4, 5480–5486.
- 243 C. Hu, Y. Zhao, H. Cheng, Y. Wang, Z. Dong, C. Jiang, X. Zhai, L. Jiang, L. Qu, *Nano Lett.* 2012, 12, 5879–5884.
- 244 B.G. Choi, M.H. Yang, W.H. Hong, J.W. Choi, Y.S. Huh, *ACS Nano* 2012, 6, 4020–4028.
- 245 X. Huang, K. Qian, J. Yang, J. Zhang, L. Li, C. Yu, D. Zhao, *Adv. Mater.* 2012, 24, 4419–4423.
- 246 M.C.J. Bradford, M.A. Vannice, *Catal. Rev.* 1999, 41, 1–42
- 247 J.C. Meyer, A.K. Geim, M.I. Katsnelson, K.S. Novoselov, T. Booth, S. Roth, *Nature* 2007, 446, 60–63.



- 248 S. Stankovich, D.A. Dikin, G.H.B. Dommett, K.M. Kohlhaas, E.J. Zimney, E.A. Stach, R. D. Piner, S. T. Nguyen, R. S. Ruoff, *Nature* 2006, 442, 282
- 249 P. K. Chu, L. Li, *Mater. Chem. Phys.* 2006, 96, 253–277.
- 250 R. Wirth, *Phys. Chem. Minerals* 1997, 24, 561–568.
- 251 W. Zhang, J. Cui, C. Tao, Y. Wu, Z. Li, L. Ma, Y. Wen, G.Li, *Angew. Chem. Int. Ed.* 2009, 121, 5978–5982.
- 252 J.M. Englert, C. Dotzer, G. Yang, M. Schmid, C. Papp, J. M. Gottfried, H.-P. Steinrück, E. Spiecker, F. Hauke, A. Hirsch, *Nature Chem.*, 2011, 3, 279–286.
- 253 Y.-B. Tang, C.-S. Lee, J. Xu, Z.-T. Liu, Z.-H. Chen, Z. B. He, Y.-L. Cao, G. D. Yuan, H. S. Song, L.M. Chen, L. Luo, H.-M. Cheng, W.-J. Zhang, I. Bello, S.-T. Lee, *ACS Nano* 2010, 4, 3482–3488.
- 254 W. Chen, L. Yan, *Nanoscale* 2010, 2, 559–563.
- 255 Z. Wei, D. Wang, S. Kim, S.-Y. Kim, Y. Hu, M.K. Yakes, A.R. Laracuente, Z. Dai, S. Marder, C. Berger, W.P. King, W. A. de Heer, P.E. Sheehan, E. Riedo, *Science* 2010, 328, 1373–1376.
- 256 (a) K. Imoto, K. Takahashi, T. Yamaguchi, T. Komura, J. Nakamura and K. Murata, *Sol. Energy Mater. Sol. Cells*, 2003, 79, 459–469; (b) H. W. Zhu, J. Q. Wei, K. L. Wang and D. H. Wu, *Sol. Energy Mater. Sol. Cells*, 2009, 93, 1461–1470.
- 257 J.K. Chen, K.X. Li, Y.H. Luo, X.Z. Guo, D.M. Li, M.H. Deng, S.Q. Huang and Q.B. Meng, *Carbon*, 2009, 47, 2704–2708.

- 258 T.N. Murakami, S. Ito, Q. Wang, M.K. Nazeeruddin, T. Bessho, I. Cesar, P. Liska, R. Humphry-Baker, P. Comte, P. Pechy and M. Grätzel, *J. Electrochem. Soc.* 2006, 153, A2255.
- 259 W.J. Lee, E. Ramasamy, D.Y. Lee and J.S. Song, *ACS Appl. Mater. Interfaces*, 2009, 1, 1145–1149.
- 260 J. Han, H. Kim, S.H. Kim, D.Y. Kim, S.M. Jo and S.Y. Jang, *ACS Nano*, 2010, 4, 3503–3509.
- 261 M.K. Wang, A.M. Anghel, B. Marsan, N.C. Ha, N. Postrakulchote, S.M. Zakeeruddin and M. Grätzel, *J. Am. Chem. Soc.* 2009, 131, 15976–15977.
- 262 H.C. Sun, D. Qin, S.Q. Huang, X.Z. Guo, D. M. Li, Y. H. Luo and Q. B. Meng, *Energy Environ. Sci.* 2011, 4, 2630–2637.
- 263 X. Xin, M. He, W. Han, J. Jung and Z. Lin, *Angew. Chem., Int. Ed.*, 2011, 50, 11739–11742.
- 264 Q.W. Jiang, G.R. Li and X. P.Gao, *Chem. Commun.*, 2009, 6720–6722.
- 265 G.R. Li, F. Wang, Q.W. Jiang, X.P. Gao and P.W. Shen, *Angew. Chem., Int. Ed.*, 2010, 49, 3653–3656.
- 266 Q.W. Jiang, G.R. Li, S. Liu and X.P. Gao, *J. Phys. Chem. C*, 2010, 114, 13397–13401.
- 267 M.X. Wu, Q.Y. Zhang, C.Y. Ma, X. Lin, C.Y. Miao, Y.J. He, Y.R. Gao, A. Hagfeldt and T.L. Ma, *J. Mater. Chem.* 2011, 21, 10761–10766.
- 268 G.R. Li, J. Song, G. Pan and X.P. Gao, *Energy Environ. Sci.*, 2011, 4, 1680–1683.
- 269 J. S. Jang, D.J. Ham, E. Ramasamy, J. Lee and J. Lee, *Chem. Commun.*, 2010, 46, 8600–8602.

- 270 M. Wu, X.A. Lin, A. Hagfeldt and T.L. Ma, *Angew. Chem., Int. Ed.*, 2011, 50, 3520–3524.
- 271 A. Kaniyoor and S. Ramaprabhu, *J. Appl. Phys.*, 2011, 109, 124308.
- 272 D.W. Zhang, X.D. Li, H.B. Li, S. Chen, Z. Sun, X.J. Yin and S.M. Huang, *Carbon*, 2011, 49, 5382–5388.
- 273 C.T. Hsieh, B.H. Yang and J.Y. Lin, *Carbon*, 2011, 49, 3092–3097.
- 274 H. Choi, S. Hwang, H. Bae, S. Kim, H. Kim and M. Jeon, *Electron. Lett.*, 2011, 47, 4.
- 275 H. Choi, H. Kim, S. Hwang, Y. Han and M. Jeon, *J. Mater. Chem.*, 2011, 21, 7548–7551.
- 276 Y. Xue, J. Liu, H. Chen, R. Wang, D. Li, J. Qu and L. Dai, *Angew. Chem. Int. Ed.* **2012**, 51, 1–5.
- 277 F. Gong, H. Wang, X. Wu, G. Zhou, Z.S. Wang, *J. Am. Chem. Soc.* 2012, 134, 10953–10958.
- 278 R. Bajpai, S. Roy, P. Kumar, P. Bajpai, N. Kulshrestha, J. Rafiee, N. Koratkar, D. S. Misra, *ACS Appl. Mater. Interfaces* 2011, 3, 3884–3889.

## Appendix A Copyright Permission of Fig 1.2 and Table 1.1

Fig. 1.2 used in Chapter 1 of this dissertation was originally published in “Transparent Carbon Films as Electrodes in Organic Solar Cells” *Angew. Chem. Inter. Ed.*, Wiley, 2008, 47, 2990–2992. Permission to reuse material from the published work was obtained with kind permission from John Wiley and Sons. A copy of the granting permission for reproduction is shown below.

This is a License Agreement between Hui Wang ("You") and John Wiley and Sons ("John Wiley and Sons") provided by Copyright Clearance Center ("CCC"). The license consists of your order details, the terms and conditions provided by John Wiley and Sons, and the payment terms and conditions.

**All payments must be made in full to CCC. For payment instructions, please see information listed at the bottom of this form.**

License Number	3234880142115
License date	Sep 23, 2013
Licensed content publisher	John Wiley and Sons
Licensed content publication	Angewandte Chemie International Edition
Licensed content title	Transparent Carbon Films as Electrodes in Organic Solar Cells
Licensed copyright line	Copyright © 2008 WILEY-VCH Verlag GmbH & Co. KGaA, Weinheim
Licensed content author	Xuan Wang, Linjie Zhi, Nok Tsao, Željko Tomović, Jiaoli Li, Klaus Müllen
Licensed content date	Mar 10, 2008
Start page	2990
End page	2992
Type of use	Dissertation/Thesis
Requestor type	University/Academic
Format	Print and electronic

Portion	Figure/table
Number of figures/tables	2
Original Wiley figure/table number(s)	Figure 3 and Table 1
Will you be translating?	No
Total	0.00 USD

## Appendix B Copyright Permission of Fig 1.3

Fig. 1.3 used in Chapter 1 of this dissertation was originally published in “Large area, continuous, few-layered graphene as anodes in organic photovoltaic devices” Applied Physics Letters, AIP Publishing LLC, 2009, 95, 063302. Permission to reuse material from the published work was obtained with kind permission from AIP Publishing LLC. A copy of the granting permission for reproduction is shown below.

### AIP PUBLISHING LLC LICENSE

**All payments must be made in full to CCC. For payment instructions, please see information listed at the bottom of this form.**

License Number	3235001195787
Order Date	Sep 23, 2013
Publisher	AIP Publishing LLC
Publication	Applied Physics Letters
Article Title	Large area, continuous, few-layered graphene as anodes in organic photovoltaic devices
Author	Yu Wang, Xiaohong Chen, Yulin Zhong, Furong Zhu, et al.
Online Publication Date	Aug 13, 2009
Volume number	95
Issue number	6
Type of Use	Thesis/Dissertation
Requestor type	University or Educational Institution
Format	Print and electronic
Portion	Figure/Table
Number of figures/tables	1
Title of your dissertation	Synthesis of Graphene and Its Application in DSSCs
Expected completion date	Sep 2013
Estimated size (number of pages)	140
Total	0.00 USD

## Appendix C Copyright Permission of Fig 1.4

Fig. 1.4 used in Chapter 1 of this dissertation was originally published in “Transparent, highly conductive graphene electrodes from acetylene-assisted thermolysis of graphite oxide sheets and nanographene molecules” Nanotechnology, IOP Publishing, 2009, 20, 434007. Permission to reuse material from the published work was obtained with kind permission from IOP Publishing. A copy of the granting permission for reproduction is shown below.

**Photocopy or share content electronically**

...if you need to distribute print and online copyrighted content to students or faculty at your institution through:

- Print coursepacks
- Classroom handouts
- Electronic reserves
- Course management systems
- Institution Intranets
- CD-ROM/DVD
- Other electronic academic uses

**You're covered if...**  
You are a faculty member or staff of an academic institution that has purchased an Annual Copyright License from Copyright Clearance Center. This permission type is covered by your license.

Close



## Appendix D Copyright Permission of Fig 1.5

Fig. 1.5 used in Chapter 1 of this dissertation was originally published in “Low-Temperature Solution Processing of Graphene–Carbon Nanotube Hybrid Materials for High-Performance Transparent Conductors” Nano Letters, American Chemical Society, 2009, 9, 1949. Permission to reuse material from the published work was obtained with kind permission from American Chemical Society. A copy of the granting permission for reproduction is shown below.

---

Home Account Info Help

**ACS Publications** Title: Low-Temperature Solution Processing of Graphene–Carbon Nanotube Hybrid Materials for High-Performance Transparent Conductors  
Author: Vincent C. Tung, Li-Min Chen, Matthew J. Allen, Jonathan K. Wassei, Kurt Nelson, Richard B. Kaner, and Yang Yang  
Publication: Nano Letters  
Publisher: American Chemical Society  
Date: May 1, 2009  
Copyright © 2009, American Chemical Society

Logged in as:  
Hui Wang  
[LOGOUT](#)

### PERMISSION/LICENSE IS GRANTED FOR YOUR ORDER AT NO CHARGE

This type of permission/license, instead of the standard Terms & Conditions, is sent to you because no fee is being charged for your order. Please note the following:

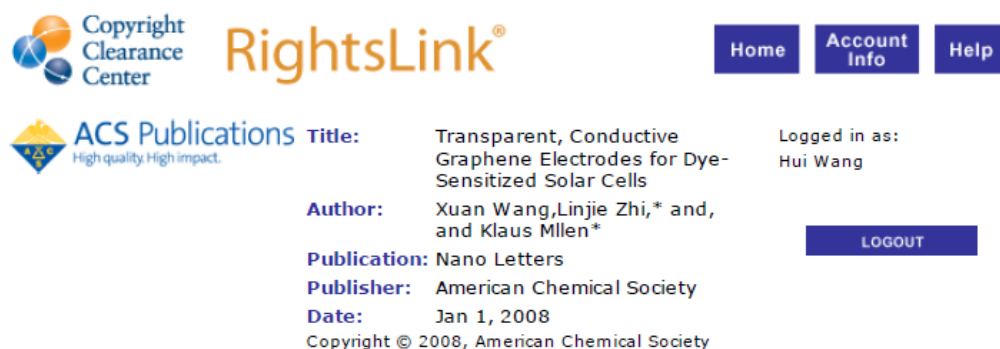
- Permission is granted for your request in both print and electronic formats, and translations.
- If figures and/or tables were requested, they may be adapted or used in part.
- Please print this page for your records and send a copy of it to your publisher/graduate school
- Appropriate credit for the requested material should be given as follows: "Reprinted (adapted) with permission from (COMPLETE REFERENCE CITATION). Copyright (YEAR) American Chemical Society." Insert appropriate information in place of the capitalized words.
- One-time permission is granted only for the use specified in your request. No additional uses are granted (such as derivative works or other editions). For any other uses, please submit a new request.

If credit is given to another source for the material you requested, permission must be obtained from that source.



## Appendix E Copyright Permission of Fig 1.6

Fig. 1.6 used in Chapter 1 of this dissertation was originally published in “Transparent, Conductive Graphene Electrodes for Dye-Sensitized Solar Cells” Nano Letters, American Chemical Society, 2008, 8, 323. Permission to reuse material from the published work was obtained with kind permission from American Chemical Society. A copy of the granting permission for reproduction is shown below.



The screenshot shows the Copyright Clearance Center RightsLink interface. At the top left is the Copyright Clearance Center logo. To its right is the RightsLink logo. Further right are three navigation buttons: Home, Account Info, and Help. Below the Copyright Clearance Center logo is the ACS Publications logo with the tagline "High quality. High impact." To the right of the ACS logo, the following information is displayed:

**Title:** Transparent, Conductive Graphene Electrodes for Dye-Sensitized Solar Cells  
**Author:** Xuan Wang, Linjie Zhi,\* and, and Klaus Mllen\*  
**Publication:** Nano Letters  
**Publisher:** American Chemical Society  
**Date:** Jan 1, 2008  
Copyright © 2008, American Chemical Society

Logged in as:  
Hui Wang

LOGOUT

### PERMISSION/LICENSE IS GRANTED FOR YOUR ORDER AT NO CHARGE

This type of permission/license, instead of the standard Terms & Conditions, is sent to you because no fee is being charged for your order. Please note the following:

- Permission is granted for your request in both print and electronic formats, and translations.
- If figures and/or tables were requested, they may be adapted or used in part.
- Please print this page for your records and send a copy of it to your publisher/graduate school.
- Appropriate credit for the requested material should be given as follows: "Reprinted (adapted) with permission from (COMPLETE REFERENCE CITATION). Copyright (YEAR) American Chemical Society." Insert appropriate information in place of the capitalized words.
- One-time permission is granted only for the use specified in your request. No additional uses are granted (such as derivative works or other editions). For any other uses, please submit a new request.

If credit is given to another source for the material you requested, permission must be obtained from that source.

## Appendix F Copyright Permission of Fig 1.7

Fig. 1.7 used in Chapter 1 of this dissertation was originally published in “UV-reduction of graphene oxide and its application as an interfacial layer to reduce the back-transport reactions in dye-sensitized solar cells” in Chemical Physics Letters, Elsevier, 2009, 483, 124. Permission to reuse material from the published work was obtained with kind permission from Elsevier. A copy of the granting permission for reproduction is shown below.

This is a License Agreement between Hui Wang ("You") and Elsevier ("Elsevier") provided by Copyright Clearance Center ("CCC"). The license consists of your order details, the terms and conditions provided by Elsevier, and the payment terms and conditions.

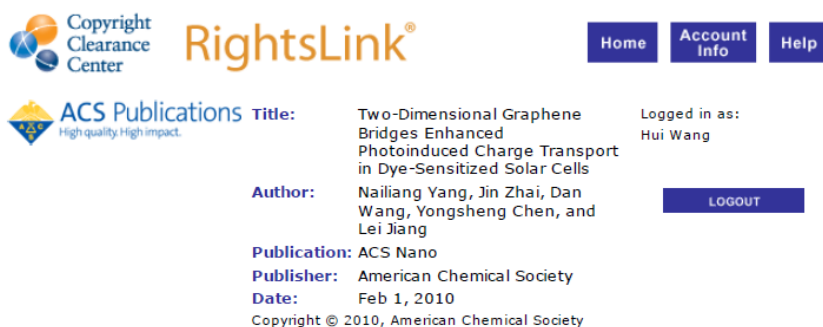
**All payments must be made in full to CCC. For payment instructions, please see information listed at the bottom of this form.**

Supplier	Elsevier Limited The Boulevard, Langford Lane Kidlington, Oxford, OX5 1GB, UK
Registered Company Number	1982084
Customer name	Hui Wang
Customer address	MM Building Michigan Tech University Houghton, MI 49931
License number	3234890052294
License date	Sep 23, 2013
Licensed content publisher	Elsevier
Licensed content publication	Chemical Physics Letters
Licensed content title	UV-reduction of graphene oxide and its application as an interfacial layer to reduce the back-transport reactions in dye-sensitized solar cells

Licensed content author	Sung Ryong Kim,Md. Khaled Parvez,Manish Chhowalla
Licensed content date	24 November 2009
Licensed content volume number	483
Licensed content issue number	1-3
Number of pages	4
Start Page	124
End Page	127
Type of Use	reuse in a thesis/dissertation
Intended publisher of new work	other
Portion	figures/tables/illustrations
Number of figures/tables/illustrations	1
Format	both print and electronic
Are you the author of this Elsevier article?	No
Will you be translating?	No
Order reference number	
Title of your thesis/dissertation	Synthesis of Graphene and Its Application in DSSCs
Expected completion date	Sep 2013
Estimated size (number of pages)	140
Elsevier VAT number	GB 494 6272 12
Permissions price	0.00 USD
VAT/Local Sales Tax	0.0 USD / 0.0 GBP
Total	0.00 USD

## Appendix G Copyright Permission of Fig 1.8

Fig. 1.8 used in Chapter 1 of this dissertation was originally published in “Two-Dimensional Graphene Bridges Enhanced Photoinduced Charge Transport in Dye-Sensitized Solar Cells”. ACS Nano, American Chemical Society, 2010, 4, 887. Permission to reuse material from the published work was obtained with kind permission from American Chemical Society. A copy of the granting permission for reproduction is shown below.



The screenshot shows the RightsLink interface. At the top left is the Copyright Clearance Center logo. To its right is the RightsLink logo. Further right are three navigation buttons: Home, Account Info, and Help. Below the logos is the ACS Publications logo with the tagline "High quality. High impact." The main content area displays the following information:

<b>Title:</b>	Two-Dimensional Graphene Bridges Enhanced Photoinduced Charge Transport in Dye-Sensitized Solar Cells	Logged in as: Hui Wang
<b>Author:</b>	Nailiang Yang, Jin Zhai, Dan Wang, Yongsheng Chen, and Lei Jiang	<a href="#">LOGOUT</a>
<b>Publication:</b>	ACS Nano	
<b>Publisher:</b>	American Chemical Society	
<b>Date:</b>	Feb 1, 2010	

Copyright © 2010, American Chemical Society

### PERMISSION/LICENSE IS GRANTED FOR YOUR ORDER AT NO CHARGE

This type of permission/license, instead of the standard Terms & Conditions, is sent to you because no fee is being charged for your order. Please note the following:

- Permission is granted for your request in both print and electronic formats, and translations.
- If figures and/or tables were requested, they may be adapted or used in part.
- Please print this page for your records and send a copy of it to your publisher/graduate school.
- Appropriate credit for the requested material should be given as follows: "Reprinted (adapted) with permission from (COMPLETE REFERENCE CITATION). Copyright (YEAR) American Chemical Society." Insert appropriate information in place of the capitalized words.
- One-time permission is granted only for the use specified in your request. No additional uses are granted (such as derivative works or other editions). For any other uses, please submit a new request.

If credit is given to another source for the material you requested, permission must be obtained from that source.

## Appendix H Copyright Permission of Chapter 1

Chapter 1 of this dissertation was originally published in “Thinnest Two-Dimensional Nanomaterial-Graphene for Solar Energy”, ChemSusChem, John Wiley and Sons, 2010, 3, 782–796. Permission to reuse material from the published work was obtained with kind permission from John Wiley and Sons. A copy of the granting permission for reproduction is shown below.

This is a License Agreement between Hui Wang ("You") and John Wiley and Sons ("John Wiley and Sons") provided by Copyright Clearance Center ("CCC"). The license consists of your order details, the terms and conditions provided by John Wiley and Sons, and the payment terms and conditions.

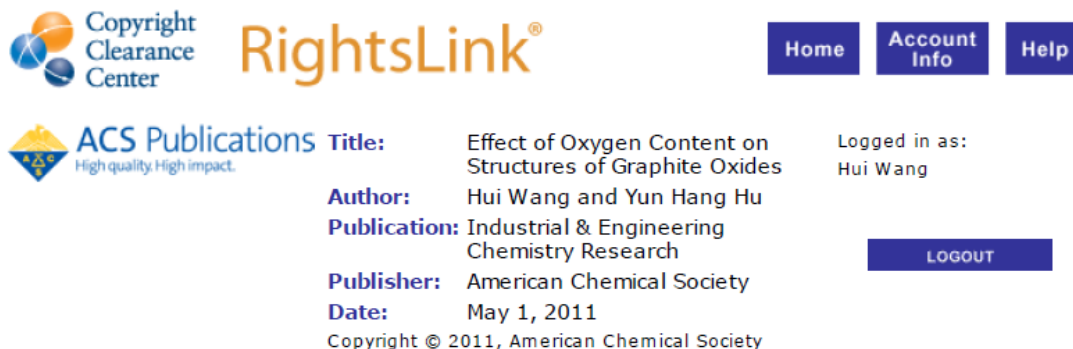
**All payments must be made in full to CCC. For payment instructions, please see information listed at the bottom of this form.**

License Number	3234890851070
License date	Sep 23, 2013
Licensed content publisher	John Wiley and Sons
Licensed content publication	ChemSusChem
Licensed content title	Thinnest Two-Dimensional Nanomaterial—Graphene for Solar Energy
Licensed copyright line	Copyright © 2010 WILEY-VCH Verlag GmbH & Co. KGaA, Weinheim
Licensed content author	Yun Hang Hu,Hui Wang,Bo Hu
Licensed content date	Jun 11, 2010
Start page	782
End page	796
Type of use	Dissertation/Thesis
Requestor type	Author of this Wiley article
Format	Print and electronic

Portion	Full article
Will you be translating?	No
Total	0.00 USD

## Appendix I Copyright Permission of Chapter 3

Chapter 3 of this dissertation was originally published in “Effect of Oxygen Content on Structures of Graphite Oxides”, *Industrial & Engineering Chemistry Research*, American Chemical Society, 2011, 50, 6132–6137. Permission to reuse material from the published work was obtained with kind permission from American Chemical Society. A copy of the granting permission for reproduction is shown below.



The screenshot shows the Copyright Clearance Center RightsLink interface. At the top left is the Copyright Clearance Center logo. To its right is the RightsLink logo. On the top right are three navigation buttons: Home, Account Info, and Help. Below the Copyright Clearance Center logo is the ACS Publications logo with the tagline "High quality. High impact." To the right of the ACS Publications logo is the following information:

**Title:** Effect of Oxygen Content on Structures of Graphite Oxides  
**Author:** Hui Wang and Yun Hang Hu  
**Publication:** Industrial & Engineering Chemistry Research  
**Publisher:** American Chemical Society  
**Date:** May 1, 2011  
Copyright © 2011, American Chemical Society

To the right of this information, it says "Logged in as: Hui Wang" and there is a blue button labeled "LOGOUT".

### PERMISSION/LICENSE IS GRANTED FOR YOUR ORDER AT NO CHARGE

This type of permission/license, instead of the standard Terms & Conditions, is sent to you because no fee is being charged for your order. Please note the following:

- Permission is granted for your request in both print and electronic formats, and translations.
- If figures and/or tables were requested, they may be adapted or used in part.
- Please print this page for your records and send a copy of it to your publisher/graduate school.
- Appropriate credit for the requested material should be given as follows: "Reprinted (adapted) with permission from (COMPLETE REFERENCE CITATION). Copyright (YEAR) American Chemical Society." Insert appropriate information in place of the capitalized words.
- One-time permission is granted only for the use specified in your request. No additional uses are granted (such as derivative works or other editions). For any other uses, please submit a new request.

## Appendix J Copyright Permission of Chapter 4

Chapter 4 of this dissertation was originally published in “Electrolyte-induced precipitation of graphene oxide in its aqueous solution”, Journal of Colloid and Interface Science, Elsevier, 2013, 391, 21–27. Permission to reuse material from the published work was obtained with kind permission from Elsevier. A copy of the granting permission for reproduction is shown below.

This is a License Agreement between Hui Wang ("You") and Elsevier ("Elsevier") provided by Copyright Clearance Center ("CCC"). The license consists of your order details, the terms and conditions provided by Elsevier, and the payment terms and conditions.

**All payments must be made in full to CCC. For payment instructions, please see information listed at the bottom of this form.**

Supplier	Elsevier Limited The Boulevard,Langford Lane Kidlington,Oxford,OX5 1GB,UK
Registered Company Number	1982084
Customer name	Hui Wang
Customer address	MMBuilding Michigan Tech University Houghton, MI 49931
License number	3234890947848
License date	Sep 23, 2013
Licensed content publisher	Elsevier
Licensed content publication	Journal of Colloid and Interface Science
Licensed content title	Electrolyte-induced precipitation of graphene oxide in its aqueous solution
Licensed content author	Hui Wang,Yun Hang Hu
Licensed content date	1 February 2013
Licensed content	391



volume number	
Licensed content issue number	
Number of pages	7
Start Page	21
End Page	27
Type of Use	reuse in a thesis/dissertation
Intended publisher of new work	other
Portion	full article
Format	both print and electronic
Are you the author of this Elsevier article?	Yes
Will you be translating?	No
Order reference number	
Title of your thesis/dissertation	Synthesis of Graphene and Its Application in DSSCs
Expected completion date	Sep 2013
Estimated size (number of pages)	140
Elsevier VAT number	GB 494 6272 12
Permissions price	0.00 USD
VAT/Local Sales Tax	0.0 USD / 0.0 GBP
Total	0.00 USD

## Appendix K Copyright Permission of Chapter 5 and Chapter 6

Chapter 5 and Chapter 6 of this dissertation were originally published in 3D Honeycomb-Like Structured Graphene and Its High Efficiency as a Counter-Electrode Catalyst for Dye-Sensitized Solar Cells” Angewandte Chemie International Edition, John Wiley and Sons, 2013, 52, 9210–9214. Permission to reuse material from the published work was obtained with kind permission from John Wiley and Sons. A copy of the granting permission for reproduction is shown below.

This is a License Agreement between Hui Wang ("You") and John Wiley and Sons ("John Wiley and Sons") provided by Copyright Clearance Center ("CCC"). The license consists of your order details, the terms and conditions provided by John Wiley and Sons, and the payment terms and conditions.

**All payments must be made in full to CCC. For payment instructions, please see information listed at the bottom of this form.**

License Number	3234891236132
License date	Sep 23, 2013
Licensed content publisher	John Wiley and Sons
Licensed content publication	Angewandte Chemie International Edition
Licensed content title	3D Honeycomb-Like Structured Graphene and Its High Efficiency as a Counter-Electrode Catalyst for Dye-Sensitized Solar Cells
Licensed copyright line	Copyright © 2013 WILEY-VCH Verlag GmbH & Co. KGaA, Weinheim
Licensed content author	Hui Wang, Kai Sun, Franklin Tao, Dario J. Stacchiola, Yun Hang Hu
Licensed content date	Jul 29, 2013
Start page	9210
End page	9214
Type of use	Dissertation/Thesis

Requestor type	Author of this Wiley article
Format	Print and electronic
Portion	Full article
Will you be translating?	No
Total	0.00 USD

## Appendix L Copyright Permission of Chapter 6

Chapter 6 of this dissertation were partially originally published in “Graphene as a counter electrode material for dye-sensitized solar cells”, Energy & Environmental Science, RSC, 2012, 5, 8182–8188. Permission to reuse material from the published work was obtained with kind permission from RSC. A copy of the granting permission for reproduction is shown below.

If you are not the author of this article and you wish to reproduce material from it in a third party non-RSC publication you must [formally request permission](#) using RightsLink. Go to our [Instructions for using RightsLink page](#) for details.

**Authors contributing to RSC publications (journal articles, books or book chapters) do not need to formally request permission to reproduce material contained in this article provided that the correct acknowledgement is given with the reproduced material.**

Reproduced material should be attributed as follows:

For reproduction of material from NJC:

Reproduced from Ref. XX with permission from the Centre National de la Recherche Scientifique (CNRS) and The Royal Society of Chemistry.

For reproduction of material from PCCP:

Reproduced from Ref. XX with permission from the PCCP Owner Societies.

For reproduction of material from PPS:

Reproduced from Ref. XX with permission from the European Society for Photobiology, the European Photochemistry Association, and The Royal Society of Chemistry.

For reproduction of material from all other RSC journals and books:

Reproduced from Ref. XX with permission from The Royal Society of Chemistry.

If the material has been adapted instead of reproduced from the original RSC publication "Reproduced from" can be substituted with "Adapted from".

In all cases the Ref. XX is the XXth reference in the list of references.

If you are the author of this article you do not need to formally request permission to reproduce figures, diagrams etc. contained in this article in third party publications or in a thesis or dissertation provided that the correct acknowledgement is given with the reproduced material.

Reproduced material should be attributed as follows:

For reproduction of material from NJC:

[Original citation] - Reproduced by permission of The Royal Society of Chemistry (RSC) on behalf of the Centre National de la Recherche Scientifique (CNRS) and the RSC

For reproduction of material from PCCP:

[Original citation] - Reproduced by permission of the PCCP Owner Societies

For reproduction of material from PPS:

[Original citation] - Reproduced by permission of The Royal Society of Chemistry (RSC) on behalf of the European Society for Photobiology, the European Photochemistry Association, and RSC

For reproduction of material from all other RSC journals:

[Original citation] - Reproduced by permission of The Royal Society of Chemistry